Engineering

RR

# Journal of Research

of the

National Bureau of Standards

DECEMBER 1954

VOLUME 53 NUMBER 6

U. S. DEPARTMENT OF COMMERCE
Sinclair Weeks, Secretary
NATIONAL BUREAU OF STANDARDS
A. V. Astin, Director

DECEMBER • 1954
VOLUME • 53
NUMBER • 6

# JOURNAL OF RESEARCH

of the

NATIONAL BUREAU OF STANDARDS

## PERIODICALS OF THE NATIONAL BUREAU OF STANDARDS

The National Bureau of Standards is engaged in fundamental and applied research in physics, chemistry, mathematics, and engineering. Projects are conducted in fifteen fields: electricity and electronics, optics and metrology, heat and power, atomic and radiation physics, chemistry, mechanics, organic and fibrous materials, metallurgy, mineral products, building technology, applied mathematics, data processing systems, cryogenic engineering, radio propagation, and radio standards. The Bureau has custody of the national standards of measurement and conducts research leading to the improvement of scientific and engineering standards and of techniques and methods of measurement. Testing methods and instruments are developed; physical constants and properties of materials are determined; and technical processes are investigated.

## JOURNAL OF RESEARCH

The Journal presents research papers by authorities in the specialized fields of physics, mathematics, chemistry, and engineering. Complete details of the work are presented, including laboratory data, experimental procedures, and theoretical and mathematical analyses. Annual subscription: domestic, $4.00; foreign, $5.25.

## TECHNICAL NEWS BULLETIN

Summaries of current research at the National Bureau of Standards are published each month in the Technical News Bulletin. The articles are brief, with emphasis on the results of research, chosen on the basis of their scientific or technologic importance. Lists of all Bureau publications during the preceding month are given, including Research Papers, Handbooks, Applied Mathematics Series, Building Materials and Structures Reports, Miscellaneous Publications, and Circulars. Each issue contains 12 or more two-column pages; illustrated. Annual subscription: domestic, $1.00; foreign, $1.35.

## BASIC RADIO PROPAGATION PREDICTIONS

The Predictions provide the information necessary for calculating the best frequencies for communication between any two points in the world at any time during the given month. The data are important to all users of long-range radio communications and navigation, including broadcasting, airline, steamship, and wireless services, as well as to investigators of radio propagation and ionosphere. Each issue, covering a period of one month, is released three months in advance and contains 16 large pages, including pertinent charts, drawings, and tables. Annual subscription: domestic, $1.00; foreign, $1.25.

Order all publications from the Superintendent of Documents
U. S. Government Printing Office, Washington 25, D. C.

The printing of this publication has been approved by the Director of the Bureau of the Budget, May 12, 1953.

Journal of Research of the National Bureau of Standards Vol. 53, No. 6, December 1954 Research Paper 2551

# Creep of High-Purity Nickel

William D. Jenkins, Thomas G. Digges, and Carl R. Johnson

A study was made of the creep behavior in tension at 300°, 700°, 900°, and 1,200° F of initially annealed high-purity nickel. Discontinuous flow was observed in each of the three stages of creep, and it was affected by temperature, strain rate, and prior-strain history. The phenomenon of strain aging was especially prominent at 300° F as manifested by the attainment of an appreciable creep life in specimens stressed in excess of the tensile strength at this temperature. The experimental results are analyzed in terms of the past and present theories of deformation of metals. Strain hardening, recovery, and the initiation, propagation, and types of fractures obtained during creep are further evaluated by means of true-stress–true-strain and hardness data obtained at room temperature and by metallographic examination of the fractured specimens.

## 1. Introduction

Numerous equations have been proposed by analysts of creep data as descriptive of the extension-time relationship in the creep of metallic materials. The equations are modified and new ones are proposed as experimental results are accumulated. To date, however, no theoretical treatment of the complete extension-time relation is universally accepted, and there is still need for additional precise data from experiments carried out under accurately controlled conditions. The interrelation of strain hardening, recovery, and recrystallization are not fully understood, and the important role of the thermal-mechanical history on creep behavior has not been generally recognized. Any adequate physical theory of the mechanism of plastic flow in creep must account for the influence of all these factors.

The present tests on high-purity nickel were made as one phase of a project to study the mechanism of creep in high-purity polycrystalline metals and to evaluate the creep behavior of these metals in comparison with binary alloys of such metals. The comprehensive program includes a study of the creep characteristics of high-purity copper, high-purity nickel, and alloys of these two metals. As previously pointed out [1],[1] the relatively low temperatures at which creep may occur in each of these metals, the unlimited solid solubility of the two metals in each other, the availability of commercial metal of high purity, and the wide industrial applications of both the metals and alloys made the binary system an attractive one for use in the present investigation.

The present paper is concerned with the results of creep tests made on high-purity nickel at 300°, 700°, 900°, and 1,200° F, the influence of rate of loading to selected creep stresses on creep behavior, and the effect of prior-strain history on the tensile properties at room temperature of the nickel. Contour and hardness surveys were also made on specimens fractured in creep and on specimens fractured in tension at room temperature, and the microstructures were correlated with creep and tensile behavior.

[1] Figures in brackets indicate the literature references at the end of this paper.

## 2. Previous Investigations

The results of creep and other tests made at the National Bureau of Standards on high-purity copper, both initially as annealed and as cold-worked to various amounts, and on annealed high-purity nickel are presented in several publications [1, 2, 3, 4]. The results of tension tests made at temperatures ranging from −320° to +1,500° F on the same lot of high-purity nickel [3] as that used in the present creep tests showed irregularities in some of the tensile properties at temperatures of about 80° to 300° F and 500° to 700° F; strain aging occurred in the range 80° to 300° F; recovery and recrystallization predominated in specimens fractured at 1,200° or 1,500° F.

Several comprehensive summaries and appraisals of the existing theories of creep have been recently published [5, 6]. Hazlett and Parker [7] included the results of some constant-stress creep tests on high-purity nickel in their discussion of the nature of the creep curve. No attempt will be made, therefore, to completely review the abundant literature on the deformation of metals, but reference will be made to selected publications that are closely related to the results given in subsequent sections of this paper.

## 3. Material, Apparatus, and Procedures

The nickel was prepared by induction melting, and all bars were processed from one 14- by 14- by 60-in. ingot. This ingot was milled, then forged to 8- by 8-in. blooms, and hot-rolled to 2½-in. square billets. The billets were then hot-rolled to ⅞-in.-diameter bars and annealed 16 hr at 1,100° F, followed by 8 hr at 1,000° F. The average grain diameter was 0.045 mm in the above condition as supplied by the manufacturer. All the specimens used in the creep tests except two were prepared from the same bar, designated as A in tables 1, 2, and 3; the two specimens prepared from bar E were used for check purposes. Chemical, spectrochemical, and vacuum-fusion analyses were made on specimens prepared from bar A, and the results (percentage by weight) were as follows: 99.85 Ni, 0.009 Cu, 0.04 Fe, 0.03 Mn, 0.11 Si, 0.007 C, 0.002 S, <0.01 Co, 0.001 $O_2$, 0.001 $N_2$, and 0.0002 $H_2$.

TABLE 1. *Summary of conditions used and results of creep tests on high-purity nickel, initially as annealed*

Rate of loading, 5,330 lb/in.², added at 1-hr intervals.

| Test | | | | | | Beginning of third stage | | | End of test | | | | | Remarks |
|---|---|---|---|---|---|---|---|---|---|---|---|---|---|---|
| Number | Temperature | Nominal creep stress [a] | Plastic extension 1 hr. after application of load | Plastic extension, intercept at zero time | Average creep rate, second stage | Time | Plastic extension | True stress [b] | Time | Plastic extension | Reduction of area | $\log_e (A_0/A_f)$ [c] | True stress | |
| | °F | lb/in.² | % | % | %/1,000 hr | hr | % | lb/in.² | hr | % | % | | lb/in.² | |
| A–5 | 800 | 37,330 | 11.7 | 11.9 | 0 | | | | 1,485 | 11.9 | 10 | | 37,800 | Test stopped in second stage. |
| A–9 | 800 | 42,660 | 21.3 | 21.7 | 0.0007 | | | | 3,798 | 21.8 | 18 | | 52,000 | Do. |
| A–4 | 800 | 45,000 | 29.2 | 32.0 | .0011 | | | | 8,070 | 32.03 | 24 | | 59,400 | Do. |
| A–12 | 800 | 45,500 | 31.0 | 34.5 | .01 | | | | 6,403 | 34.56 | 26 | | 61,200 | Do. |
| A–16 | 800 | 46,000 | 37.5 | 35.4 | 2.100 | 2.66 | 41.1 | 64,980 | 3.6 | 69.5 | 87.6 | 2.08 | 370,800 | Tested to complete fracture. |
| A–17 | 700 | 16,000 | 1.78 | 3.65 | 0.30 | | | | 3,919 | 4.84 | 4.6 | | 23,700 | Test stopped in second stage. |
| A–11 | 700 | 21,330 | 4.7 | 16.9 | 1.6 | 9,800 | 32.5 | 28,400 | 21,047 | 101 | 93.0 | 2.67 | 306,600 | Tested to complete fracture. |
| A–10 | 700 | 26,670 | 9.4 | 15.0 | 33.3 | 690 | 38 | 36,800 | 1,015 | 99.5 | 92.3 | 2.56 | 346,400 | Do. |
| A–15 | 700 | 29,335 | 12.5 | 16.6 | 120 | 127 | 32 | 38,700 | 207 | 91 | 93.4 | 2.72 | 444,700 | Do. |
| A–7 | 700 | 32,000 | 21.5 | 22.3 | 1,020 | 14.5 | 37 | 43,800 | 22.1 | 73 | 92.9 | 2.65 | 454,100 | Do. |
| A–13 | 900 | 10,670 | 1.02 | 7.10 | 1.52 | | | | 4,004 | 13.26 | 11.8 | | 12,100 | Test stopped in second stage. |
| A–8 | 900 | 13,335 | 2.3 | 9.7 | 7.35 | | | | 2,138 | 25.3 | 20 | | 16,700 | Do. |
| A–6 | 900 | 16,000 | 2.8 | 13.0 | 20.1 | 960 | 33.5 | 21,400 | 1,870 | 60.6 | 42 | | 28,000 | Test stopped in third stage. |
| A–14 | 900 | 18,670 | 8.9 | 14.0 | 238 | 92 | 36 | 25,400 | 153 | 107.5 | 95.8 | 3.14 | 443,400 | Tested to complete fracture. |
| A–18 | 900 | 20,000 | 12.3 | 17.5 | 620 | 34 | 39 | 27,800 | 57.1 | 102.5 | 95.9 | 3.19 | 484,500 | Do. |
| A22 | 1,200 | 4,010 | 0.07 | 0.94 | 10.5 | 370 | 4.5 | 4,200 | 6,800 | 66 | 47.1 | 0.64 | 7,600 | Tested to complete fracture. |
| A–21 | 1,200 | 6,670 | 1.6 | 4.4 | 62.5 | 82 | 9.5 | 7,300 | 224 | 87 | 98.1 | 3.96 | 349,400 | Do. |
| A–20 | 1,200 | 9,330 | 5.1 | 6.5 | 500 | 20 | 17 | 10,900 | 32.3 | 91 | 97.4 | 3.66 | 361,000 | Do. |

[a] The nominal stress is defined as the stress obtained by dividing the current load by the original cross-sectional area of the specimen.
[b] The true stress is defined as the stress obtained by dividing the current load by the current minimum cross-sectional area of the specimen.
[c] $A_0/A_f$ is a ratio; the value $A_0$ being the initial cross-sectional area of the specimen, and the value $A_f$ being the minimum cross-sectional area of the specimen after fracture.

TABLE 2. *Effect of rate of loading on creep of high-purity nickel, initially as annealed*

| Test | Creep behavior at 800° F and at indicated stresses | | | | | | | | | | | | | | | | | | | | |
|---|---|---|---|---|---|---|---|---|---|---|---|---|---|---|---|---|---|---|---|---|---|
| | 37,330 lb/in.² | | | 42,660 lb/in.² | | | 45,000 lb/in.² | | | 45,500 lb/in.² | | | 46,000 lb/in.² | | | 46,500 lb/in.² | | | | |
| | Extension prior to application of this stress | Time at this stress | Extension at end of test at this stress | Mean creep rate [a] at this stress | Mean creep rate at this stress | Time at this stress | Extension at end of test at this stress | Mean creep rate at this stress | Time at this stress | Extension at end of test at this stress | Mean creep rate at this stress | Time at this stress | Extension at end of test at this stress | Mean creep rate at this stress | Time at this stress | Extension at end of test at this stress | Mean creep rate at this stress | Time at this stress | Extension at end of test at this stress | | |
| | % | hr | % | %/1,000 hr | %/1,000 hr | hr | % | %/1,000 hr | hr | % | %/1,000 hr | hr | % | %/1,000 hr | hr | % | %/1,000 hr | hr | % | | |
| A–5 | 7.496 | 1482.8 | 11.875 | 2.95 | 4925 | 1 | 16.80 | 3.76 | 2249.3 | 25.257 | 0.33 | 3170.8 | 26.315 | 0.02 | 3982.3 | 26.395 | 0.44 | 2804.8 | 27.679 | | |
| A–9 | 8.02 | 1 | 12.352 | 4332 | 2.49 | 3798 | 21.787 | 1.31 | 2833 | 25.502 | .044 | 2937.8 | 25.502 | .38 | 3191.5 | 26.812 | .37 | 3841.5 | 28.219 | | |
| A–4 | 8.53 | 1 | 13.00 | 4740 | 8547 | 1 | 21.547 | 1.30 | 8070 | 32.029 | .0044 | 2496.5 | 32.04 | .023 | 1560.8 | 32.076 | 2.61 | 1032.8 | 34.777 | | |
| A–12 | 8.53 | 1 | 13.45 | 4920 | 8051 | 1 | 21.501 | | | | 2.04 | 6403.5 | 34.56 | .019 | 2640.5 | 34.610 | 0.75 | 4552.5 | 38.046 | | |

| Test | 47,000 lb/in.² | | | 47,500 lb/in.² | | | 48,000 lb/in.² | | | Fracture | | | | | Remarks |
|---|---|---|---|---|---|---|---|---|---|---|---|---|---|---|---|
| | Mean creep rate at this stress | Time at this stress | Extension at end of test at this stress | Mean creep rate at this stress | Time at this stress | Extension at end of test at this stress | Mean creep rate at this stress | Time at this stress | Extension at end of test at this stress | Total time of test | Plastic extension | Reduction of area | $\log_e (A_0/A_f)$ | True stress | |
| | %/1,000 hr | hr | % | %/1,000 hr | hr | % | %/1,000 hr | hr | % | hr | % | % | | lb/in.² | |
| A–5 | 0.78 | 2185.5 | 29.374 | 1.14 | 2808.8 | 32.578 | 58.5 | 383.5 | 55.0 | 19,200 | 55.0 | 84 | 1.820 | 256,200 | Fractured under stress of 48,000 lb/in.² |
| A–9 | .41 | 2880.5 | 29.362 | 2.61 | 1367.3 | 32.961 | 270 | 85.5 | 56.0 | 20,000 | 56.0 | 85 | 1.913 | 325,200 | Do. |
| A–4 | 46.9 | 526.3 | 59.5 | | | | | | | 13,700 | 59.5 | 87 | 2.037 | 360,300 | Fractured under stress of 47,000 lb/in.² |
| A–12 | 24.4 | 911.0 | 60.3 | | | | | | | 14,500 | 60.3 | 85 | 1.894 | 312,100 | Do. |

[a] The mean creep rate (%/1,000 hr) is defined as that creep rate obtained by dividing the total plastic extension (percent) at the designated stress by the time hr/1,000 at the designated stress.

TABLE 2. *Effect of rate of loading on creep of high-purity nickel, initially as annealed*—Continued

| Test | Creep behavior at different temperatures | | | | | | | | | | | | | | Remarks |
|---|---|---|---|---|---|---|---|---|---|---|---|---|---|---|---|
| | Temperature | Prior-strain history | Nominal creep stress | Plastic extension, 1 hr after application of load | Plastic extension, interept at zero time | Average creep rate, second stage | Beginning of third stage | | | End of test | | | | | |
| | | | | | | | Time | Plastic extension | True stress | Total time at indicated stress | Total plastic extension | Reduction of area | $\log_e (A_0/A_f)$ | True stress | |
| | ° F | | lb/in.² | % | % | %/1,000 hr | hr | % | lb/in.² | hr | % | % | | lb/in.² | |
| A–17 | 700 | Loaded 5,330 (lb/in.²)/hr to 16,000 lb/in.² Stress changed to 21,330 lb/in.² after 3909.8 hr. | 21,330 | 6.761 | 10.5 | 2.2 | | | | 2067.7 | 15.128 | 13.2 | | 24,000 | Test stopped in second stage. |
| A–13 | 900 | Step 1. Loaded 5,330 (lb/in.²)/hr to 10,670 lb/in.² Stress changed to 13,335 lb/in.² after 4,004 hr. | 13,335 | 13.850 | 19.2 | 4.6 | | | | 2183 | 29.44 | 22.7 | | 17,250 | Do. |
| | | Step 2. Stress lowered to zero and held for 63.75 hr before reloading to 13,335 lb/in.². | 13,335 | 29.44 | 29.43 | 3.5 | | | | 904 | 32.8 | 24.7 | | 17,700 | Do. |
| | | Step 3. Stress changed to 16,000 lb/in.², 904 hr after reapplication of stress. | 16,000 | 33.77 | 35.1 | 43.2 | 280 | 48 | 23,700 | 585 | 89 | 89 | 2.21 | 145,700 | Tested to complete fracture. |

TABLE 3. *Effect of prior-strain history on the mechanical properties, at room temperature, of high-purity nickel, initially as annealed at 1,100° F for 16 hr and at 1,000° F for 8 hr*

| Specimen | Additional thermal-strain history | Yield strength (0.2% offset) | Maximum load * | | | | | Beginning of fracture * | | Complete fracture | | | | | | True strain (tensile test only) |
|---|---|---|---|---|---|---|---|---|---|---|---|---|---|---|---|---|
| | | | Tensile strength | True stress | Strain in 2 in. | Reduction in area | True strain | True stress | True strain | True stress | Elongation in 2 in. | | Reduction of area | | |
| | | | | | | | | | | | Tensile test only | Creep and tensile test | Tensile test only | Creep and tensile test | |
| | | lb/in.² | lb/in.² | lb/in.² | % | % | $\log_e (A_0/A)$ | lb/in.² | $\log_e (A_0/A)$ | lb/in.² | % | % | % | % | $\log_e (A_0/A)$ |
| C–9 | Subjected to no additional treatment. | 12,500 | 51,000 | 72,300 | 41 | 29 | 0.340 | 145,300 | 1.65 | 222,800 | 56 | | 87 | | 2.076 |
| E–5 | Tested in creep for 1,036 hr at 900° F to a reduction of area of 12 percent. | 21,700 | 53,400 | 75,500 | 40 | 28.5 | .336 | 151,300 | 1.536 | 248,500 | 53 | 79 | 87 | 88.5 | 2.032 |
| E–4 | Tested in creep for 2,829 hr at 900° F to a reduction of area of 19 percent. | 24,000 | 54,800 | 74,900 | 37 | 27 | .314 | 144,600 | 1.485 | 226,000 | 49 | 91 | 85.5 | 88 | 1.932 |
| A–6 | Tested in creep for 1,870 hr at 900° F to a reduction of area of 42.6 percent. | 39,800 | 63,100 | 82,900 | 31.5 | 24 | .273 | 139,700 | 1.293 | 184,900 | 22 | 114 | 78 | 87 | 1.514 |
| A–19 | Annealed at 1,750° F for 1 hr. | 6,300 | 47,100 | 66,900 | 42 | 29.5 | .351 | 122,400 | 1.492 | 230,500 | 65 | | 88 | | 2.125 |
| 631–A | Cold-drawn 30 percent reduction of area; followed by annealing at 1,750° F for 1 hr. | 6,700 | 50,700 | 71,000 | 40 | 28.5 | .337 | 124,800 | 1.353 | 217,200 | 63 | | 85 | | 1.907 |
| A–8 | Tested in creep for 2,138 hr at 900° F to a reduction of area of 25.4 percent before annealing at 1,750° F for 1 hr. | 7,200 | 46,000 | 67,300 | 46.5 | 31.5 | .381 | 116,600 | 1.469 | 169,400 | 64.5 | 104 | 84 | 88 | 1.843 |
| A–17 | Tested in creep for 5,978 hr at 700° F to a reduction of area of 30.8 percent before annealing at 1,750° F for 1 hr. | 8,500 | 44,700 | 70,400 | 57.5 | 36.5 | .453 | 117,400 | 1.616 | 193,700 | 67 | 118 | 88 | 92 | 2.117 |

* The strain, reduction of area, or true-strain values at maximum load or at beginning of fracture are based on measurements obtained in the tensile tests.

Tensile tests at room temperature were also made on specimens prepared from bar A and on two additional ⅞-in. round bars, designated C and 631–A (table 3). A subsequent annealing treatment was carried out at 1,750° F on certain specimens prepared from bars A and 631–A in order to produce a relatively coarse grain size (approximately 1.5- to 2-mm avg diam).

The preparation of the specimens and the apparatus used for creep testing have been previously described [1]. The creep specimens had a reduced section of 0.505-in. diameter and a gage length of 2 in. Each specimen was heated in air to the desired temperature in an electrically heated furnace regulated by a photoelectric-type control. Each specimen was held at the temperature for 48 hr before applying the loads. Increments of load were added at 1-hr intervals until the desired creep stress was reached. The load increment corresponded to a stress of 5,333 lb/in.$^2$ unless the creep stress was not a multiple of 5,333. In that case, the final increment was smaller. This loading procedure (selected as standard) was modified in those tests designed to show the influence of rate of loading on creep behavior. All of the creep tests were made under constant loads and the creep-stress values (also designated as nominal stresses) were obtained by dividing the loads by the original cross-sectional area of the specimens.

The tensile tests at room temperature were made at a strain rate of approximately 1-percent reduction of area per minute. Usual recommended procedures were used for preparing specimens and making the Rockwell hardness measurements and in the preparation of specimens, by mechanical methods, for metallographic examination [3].

## 4. Results and Discussion

### 4.1. Effect of Stress and Temperature on Creep Behavior

The results of the creep tests made on specimens loaded at the standard rate are summarized in table 1 and shown in figures 1 to 15.

#### a. Resistance to Plastic Deformation

The resistance of the nickel to plastic deformation decreased as the test temperatures were increased (fig. 1,A). Some idea of the reproducibility of the strain measurements 1 hr after the application of stress increments of 5,330 lb/in.$^2$ can be obtained from the lengths of the horizontal bars representing the range of extension values for the number of test specimens designated above these bars. The resistance to flow at each temperature was similar for all the nickel specimens tested at that selected temperature. Furthermore, no marked differences were obtained in the extension measurements made on the extensometer strips located 180° apart on the specimen (positions x and y, respectively, fig. 1,B). This fact indicates that nearly axial loading was attained and accurate measurements of extension were made even in the primary stage of creep.

#### b. Extension-Time Curves

The families of curves in figures 2, 3, and 4 depict the creep behavior of the nickel in relation to different stress levels at temperatures of 700°, 900°, and 1,200° F, respectively. The extension-time curves for specimens tested at 300° F are given in figure 17 and will be discussed later. An attempt was made to select the applied loads so that at least one specimen in each series would be subject to the same load at each of the four temperatures used. However, this was impractical because of the wide differences in resistance to flow over the temperature range 300° to 1,200° F. For example, a specimen stressed at 9,330 lb/in.$^2$ at 1,200° F (fig. 4) fractured in 32.3 hr at an extension of 91 percent, whereas a specimen stressed at 16,000 lb/in.$^2$ at 700° F (fig. 2) lengthened only 5 percent in 3,900 hr. The appearance of the extension-time curves, as plotted, indicates that creep occurred in a continuous manner in all specimens except the one stressed at 4,010 lb/in.$^2$ at 1,200° F (fig. 4). The irregularity in the latter curve is believed to be due to a combination of strain hardening and recrystallization with recrystallization predominating; high-purity nickel recrystallizes at approximately 1,100° F [8]. However, when the data were plotted on a more expanded scale (not shown), irregularities in the extension-time curves were observed in each of the three stages of creep in all of the specimens tested to complete fracture. The presence of irregularities is clearly illustrated in the logarithm of creep rate-extension curves of figures 5 and 6. The serrations in these curves are in excess of those that can be attributed to variations in test conditions. The magnitude of the serrations at low stresses appears to be greater than at the high-stress levels at equal temperatures, due, in part, to the use of the semilog relationship. The serrated curves, in general, may be considered as due to a repetitive series of reactions occurring consecutively, each with a different energy of activation as affected by the instantaneous condition of the nickel. These irregularities in the three stages of creep are considered, at least in part, to be due to such factors as grain orientations, grain rotation, formation of subgrains within the parent grains, strain hardening, recovery, and formation of cracks.

The shape of the curves for specimens tested at 300° F at stresses of 45,000 and 45,500 lb/in.$^2$ (fig. 5) may be interpreted as indicating flow by the predominance of the exhaustion mechanism of dislocations [10] and also the existence of a stress region between 45,500 and 46,000 lb/in.$^2$ where the flow is predominately by the generation of dislocations. The considerable jaggedness shown in the curves for the specimens tested at 700° F were possibly accentuated by the nearness to the magnetic transformation (Curie point) of nickel (680° F) [8].

Discontinuities obtained in some of the tensile properties of this high-purity nickel at both 300° and 700° F were also discussed in a previous publication [3]. According to Köster [9], the elastic modulus in tension of nickel decreases as the test temperature is increased from 80° to about 350° F

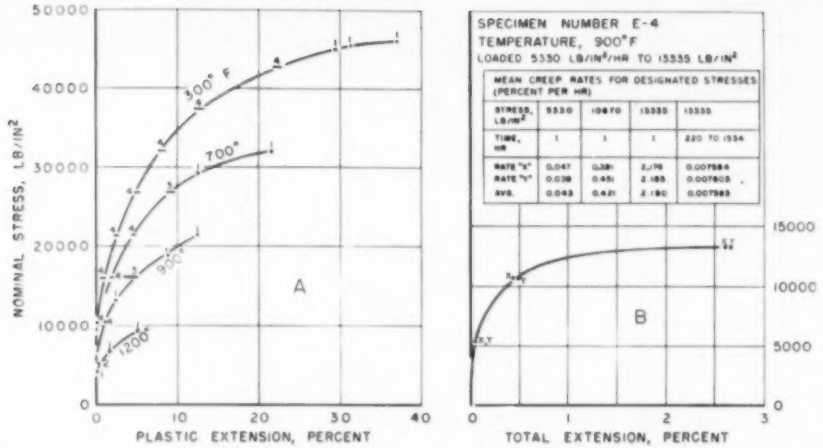


FIGURE 1. *Effect of temperature on the stress-extension relation during loading of the annealed nickel.*

The values for extension are those obtained after the application of the loads for a period of 1 hr.

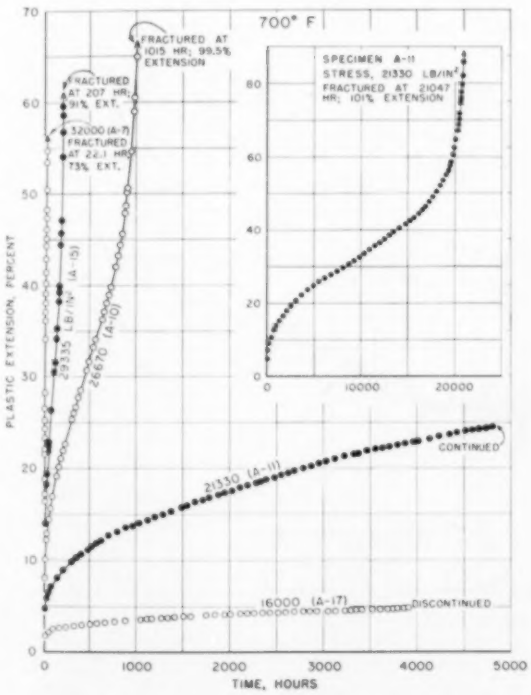


FIGURE 2. *Extension-time curves for the nickel at 700° F.*

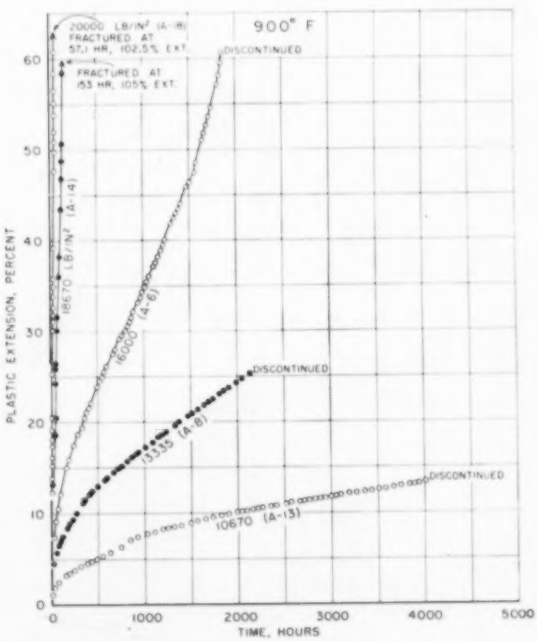


FIGURE 3. *Extension-time curves for the nickel at 900° F.*

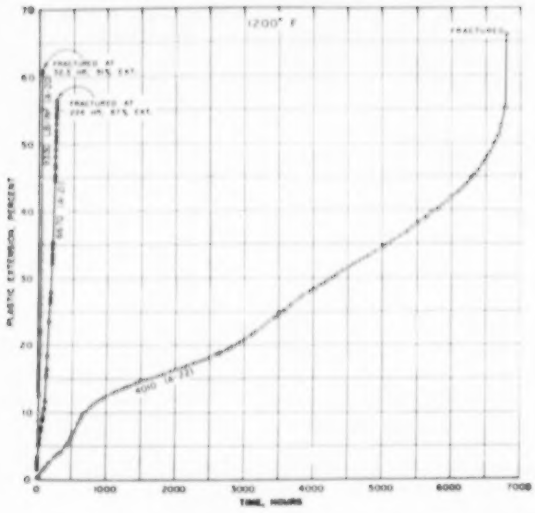


FIGURE 4. *Extension-time curves for the nickel at 1,200° F.*

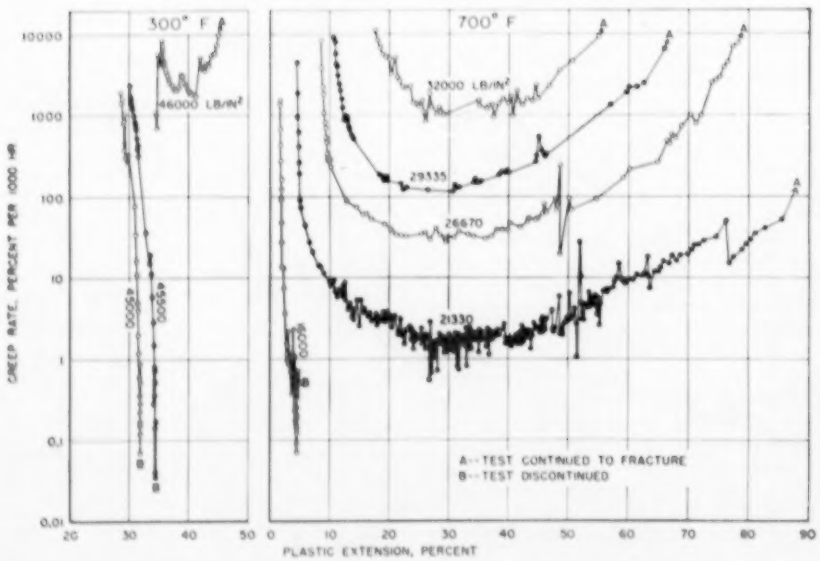


FIGURE 5. *Relation of creep rate to plastic extension at 300° and 700° F.*

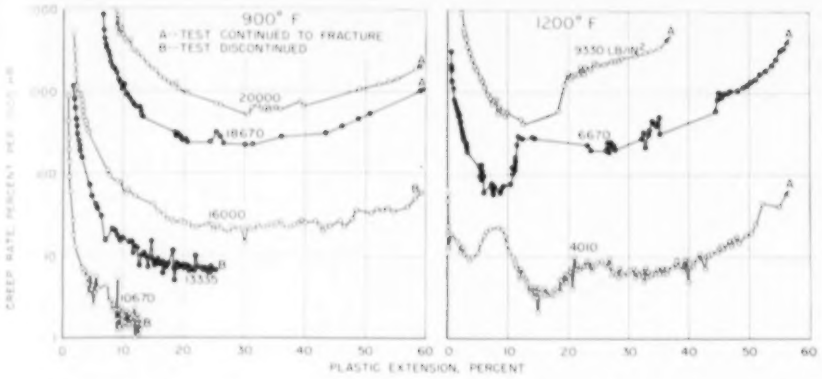


FIGURE 6. *Relation of creep rate to plastic extension at 900° and 1,200° F.*

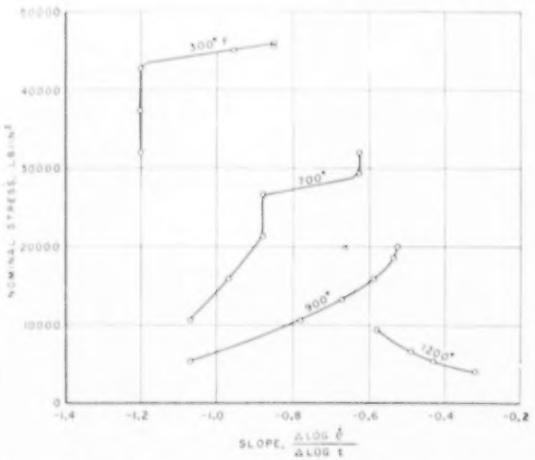


FIGURE 7. *Influence of stress on the log creep rate (ė)—log time (t) slopes during the first stage of creep at different temperatures.*

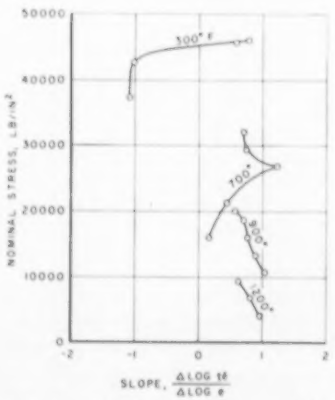


FIGURE 8. *Influence of stress on the log product of time (t) and creep rate (ė)—log extension (e) slopes during the first stage of creep at different temperatures.*

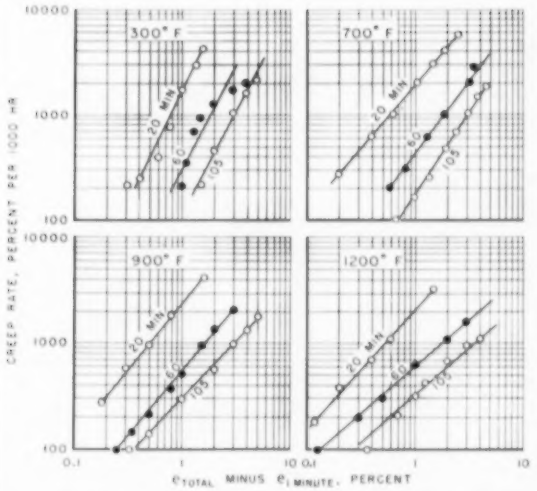


FIGURE 9. *Relation of creep rate to plastic extension at different temperatures and times.*

$e_{total}$=extension at designated time; $e_{1\ min}$=extension at the end of 1 min.

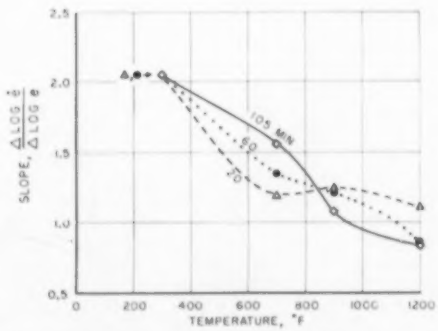


FIGURE 10. *Variation in slope of log creep rate (ė)—log extension (e) curves of nickel with temperature at different times.*

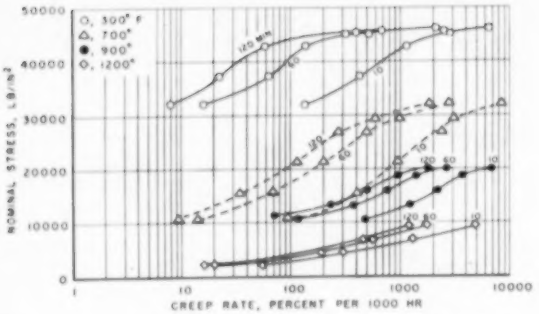


FIGURE 11. *Relation of nominal stress to first stage creep rate at different temperatures and times.*

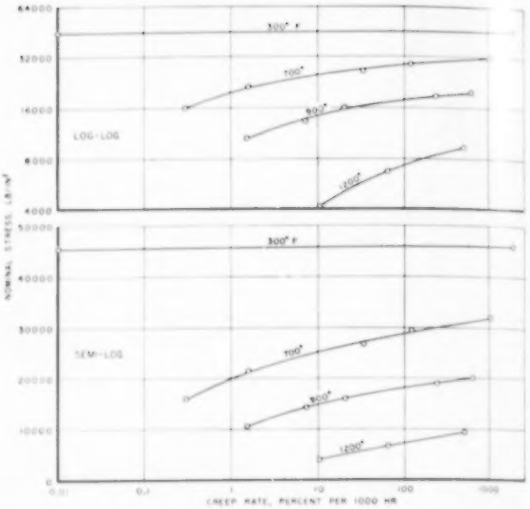


FIGURE 12. *Influence of stress on the average creep rate during the second stage of creep at different temperatures.*

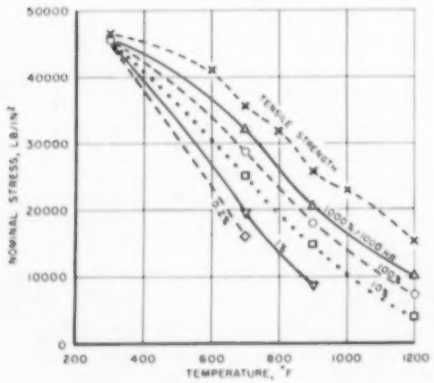


FIGURE 13. *Variation in stress required to produce different creep rates in the second stage at different temperatures.*

The influence of temperature on the tensile strength of the nickel is also shown.

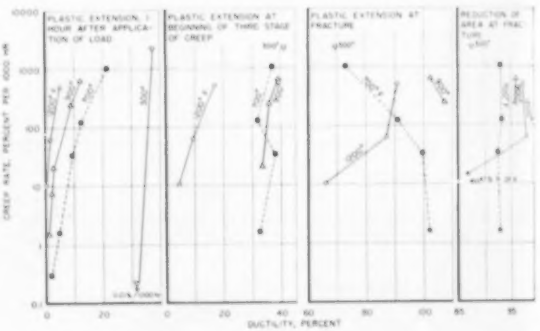


FIGURE 14. *Relation of creep rate in the second stage to ductility at various stages of the creep tests.*

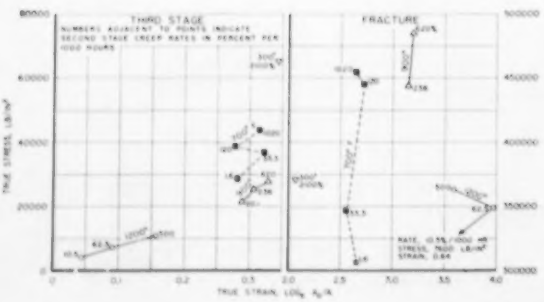


FIGURE 15. *True stress-true strain relations at different temperatures and second stage creep rates.*

$A_0$ and $A$ are initial and current cross-sectional areas, respectively, of the creep specimens.

and it then increases with further increase in temperature to the Curie point (680° F). The values at 80° and 680° F were nearly the same. The modulus then decreases continuously as the temperature is increased from 680° to 1,400° F.

The discontinuities appear to increase in magnitude with decrease in stress both at 700° and at 900° F (fig. 6). The latter temperature seems to be more favorable for a continuing balance between strain hardening and recovery. The curves for specimens tested at 1,200° F are representative of the effect of stress, in the recrystallization region, on the initiation of strain hardening of the original grains, followed by continuous recovery, then recrystallization, followed by grain growth and creep in the larger grains. These processes are sensitive to stress and temperature, as shown by the magnitude and the distribution of the discontinuities.

### c. First Stage of Creep

The relationship between the logarithm of creep rate and the logarithm of time is nearly linear in the initial portion of the first stage of creep of the nickel specimens (curves are not shown). The cycling effects observed, however, are considered as indicating that the deformation process should be both stress and temperature dependent. In contrast, the analysis made by Andrade [11] indicated that the mechanism of deformation in the initial stage of creep is independent of stress, temperature, and chemical composition.

The effect of stress and temperature on the slope of the logarithmic creep-rate–time curves is shown in figure 7.[2] At 300° F, the slopes are independent of stresses within the range of 32,000 to 43,000 lb/in.$^2$, but the slope increases as the stress is further increased to 45,000 lb/in.$^2$ At 700° F, the slope is independent of stress over some stress ranges, but it is strongly stress dependent over other ranges. At 900° F, the slope shows a continuous increase with increase in creep stress; it appears to approach a limiting value at relatively high stress levels. Contrary to the trend at 900° F, the slope of the curves for the specimens tested at 1,200° F shows a continuous decrease with increase in stress.

The present data were evaluated to ascertain the conformity of the creep of nickel to the exhaustion theory proposed by Mott and Nabarro [10] and modified by Davis and Thompson [12]. The exhaustion theory is considered as generally applicable to the primary creep of metals at relatively low temperatures and stresses. The modified theory predicts a linear relation between the logarithm of the product of the creep rate and time and the logarithm of the strain; in this plot, the values for the slope of the curves should be within the range of $-\frac{1}{2}$ and $+1$. Most of the experimental results (fig. 8) agree closely with the results predicted by the modified theory.

The relation of creep rate to strain for periods of 20, 60, and 105 min after the application of the creep stresses at different temperatures is illustrated by the results summarized in figure 9. The maximum deviation from linearity (log-log plot) is shown in the experimental results obtained 60 min after the application of the stresses at 300° F; this temperature is within the range where strain aging can occur in the nickel. Some deviations from linearity are also shown in the values for a period of 105 min at 1,200° F; recrystallization can occur at this temperature. The slopes of the family of curves shown for specimens at 300° F were nearly constant (see also fig. 10), whereas the slopes varied somewhat with the other test temperatures used. The slopes of the three curves again coincide at a temperature of approximately 850° F.

The influence of stress on the creep rate for selected periods of 10, 60, and 120 min after the application of stress at the different test temperatures is shown in the results of figure 11. The contour of the family of sigmoidal curves (semilog plot) is affected by both time and temperature; the curves representing the values, as plotted on a log-log basis (not shown) are also sigmoidal. The curves (fig. 11) also indicate that, at each temperature used, there is a threshold stress below which no measurable creep would occur.

### d. Second and Third Stages of Creep

Numerous theories have been proposed to explain the effects of stress on the rate of creep in the second stage. Linear relations have been obtained between stress and creep rate of various metallic materials when the experimental values were plotted on the basis of log-log, semilog, or creep rate—hyperbolic sine function of stress.

The influence of stress on the secondary creep rate of the nickel at different temperatures is shown by the results given in figure 12. The relationship between stress and creep rate, in general, is not linear when the experimental values for the nickel are plotted on either a log-log or a semilog basis; a linear relation is obtained in the semilog plot of the values obtained for the specimens at 1,200° F. The resistance to creep increased with a decrease in test temperature. At 300° F the initially annealed nickel had a high resistance to creep for stresses up to 45,500 lb/in.$^2$, but with a further increase in stress of 500 lb/in.$^2$ the creep rate increased by a factor of about 100,000. It is noteworthy that these stresses used in the creep tests are only about 1,500 and 1,000 lb/in.$^2$, respectively, below the tensile strength of the nickel at 300° F (fig. 13). The high resistance of the nickel to creep at 300° F is attributed to a combination of strain and age hardening and relatively low rate of recovery. At 700°, 900°, 1,200° F (fig. 12), the creep rates increased continuously with an increase in stress in the ranges investigated. This curvilinear relationship indicates that the deformation characteristic (strain hardening and recovery) of the nickel continuously changed as the stress was increased. However, the linear relationship obtained between the stress and log creep rate of the values for specimens tested at 1,200° F is indicative of an approach to viscous flow at this temperature.

The relation between stress and temperature to produce various second-stage creep rates is shown in

[2] The increments, such as $\Delta \log t$ or $\Delta \log \dot{\epsilon}$, in this and other diagrams were taken sufficiently large so as to eliminate the effects of the small oscillations of creep rate.

figure 13. The trend is for the curves to converge at a test temperature of about 300° F. The magnitude of differences between the curves corresponding to the various creep rates emphasizes the importance of a knowledge of the engineering properties of a metallic material and the accompanying microstructures in the design of components for use at elevated temperatures.

The relation between second-stage creep rate and ductility is shown in figure 14. The amount of plastic extension on loading decreased continuously with increase in temperature necessary to produce equivalent second-stage creep rates.

Relatively little information is available in the literature on the third stage of creep. The initiation of this stage has been attributed to such factors as the beginning of microcracking, increase in creep stress due to a decrease in the area of the specimen, atomic rearrangement, etc.

The plastic extension at the beginning of the third stage of creep increased with increase in secondary creep rate at both 900° and 1,200° F (fig. 14). Although the change in ductility with creep rate was more pronounced at the higher temperature, the amount of plastic extension at the beginning of the third stage was appreciably greater at 900° than at 1,200° F. At 700° F, however, the extension-creep rate curve shows reversals in the intermediate range of rates. Only one specimen was tested into the third stage and to complete fracture at 300° F. A maximum value for plastic extension at the beginning of the third stage was attained with this specimen, but its extension at fracture was appreciably less than that of some other specimens fractured at 700°, 900°, or 1,200° F. All the fractured specimens had an extension of 65 percent or more before fracturing; in some cases, the elongation in 2 in. exceeded 100 percent. However, the effect of secondary creep rate on the plastic extension at fracture varied with the test temperatures used. At 700° and 900° F, the extension increased as the creep rates were decreased, whereas at 1,200° F the extension increased with increase in the rates. The reduction of area at fracture was nearly insensitive to the rate of extension used, but the general trend was for the reduction of area to increase with an increase in temperature; however, one specimen tested at a secondary creep rate of about 10 percent per 1,000 hr at 1,200° F had a relatively low value for the reduction of area (47%).

The true strain, $\log_e(A_0/A)$, at the beginning of the third stage of creep increased continuously with the true stress at 900° and 1,200° F (fig. 15), but reversals were again obtained in the curve representing the true-stress–true-strain relation at 700° F. At each of these temperatures, the true stress (see table 1) increased continuously with increase in the creep rate in the second stage. The true-strain values at the beginning of the third stage were appreciably higher in all of the specimens tested at 300°, 700°, and 900° F than in the specimens tested at 1,200° F, even though the creep rate of some of the former specimens was slower than those at 1,200° F. Thus, the phenomenon of recrystallization that

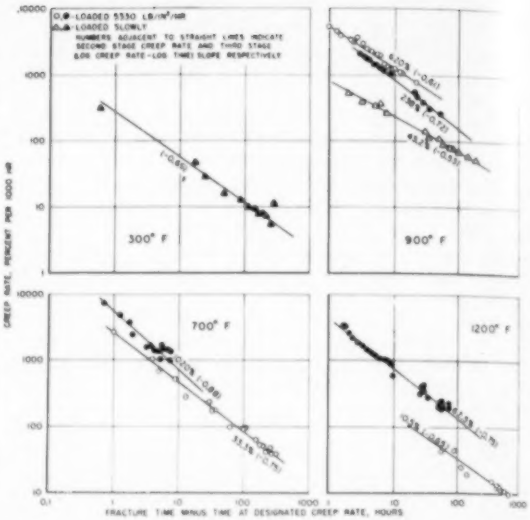


FIGURE 16. *Effects of temperature, second stage creep rate, and rate of loading on the creep rate-time relation in the third stage of creep.*

Data at 300° F was obtained for specimen A–5 under creep stress of 48,000 lb/in. (see table 2 for rate of loading).

occurred at 1,200° F was not accompanied by an increase in ductility as measured by the true strain at the beginning of the third stage.

The true strain at fracture was relatively insensitive to variations in true stress at 700° or 900° F, whereas at 1,200° F the true strain was materially affected by changes in true stress or secondary creep rate. Except for one specimen tested at a slow rate, the true strain at fracture increased with an increase in test temperature.

The effect of temperature and secondary creep rate on the rate-time relation during the third stage of creep is shown in figure 16. The slope of the linear curves differed somewhat as the test conditions were altered. The general trend was for the numerical values of slopes of these curves to be steeper for the specimens tested at 700° or 1,200° F than those at 900° F.

An analysis of measurements of ductility made under creep conditions showed that the flow characteristics of the nickel cannot always be predicted accurately from results based solely on determinations of stress, time, and ductility at fracture.

### 4.2. Effect of Rate of Loading on Creep Behavior

Tests were made at 300°, 700°, and 900° F to determine the influence of rate of loading to different stress levels on the creep characteristic of the nickel initially as annealed. The test conditions and results are summarized in table 2 and figures 17 to 24.

Extension-time curves are given in figure 17 for specimens tested at 300° F that were loaded at the standard rate until the creep stresses of 37,330,

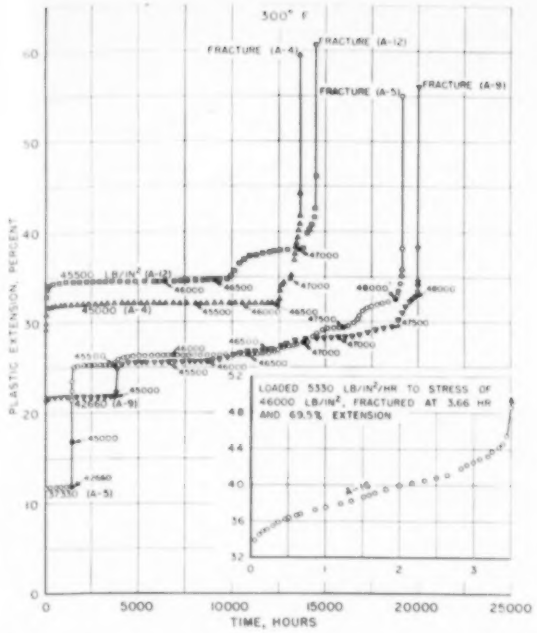


FIGURE 17. *Extension-time curves for specimens loaded at different rates to different stresses at 300° F.*

Solid symbols indicate points where stress was changed.

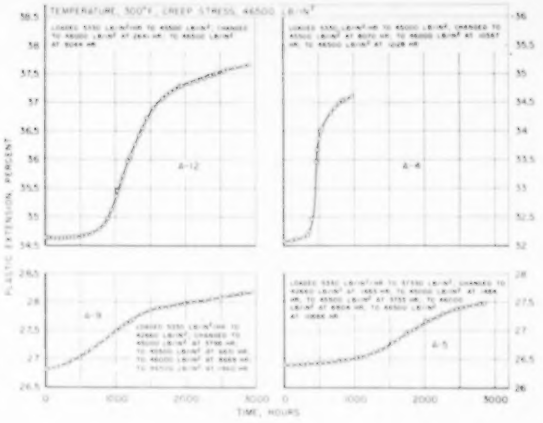


FIGURE 18. *Effect of rate of loading on the extension-time relation at 300° F and stress of 46,500 lb/in.²*

The values for time include only the range after application of stress of 46,500 lb/in.². The values of plastic extensions include all prior extension attained in creep at 300° F.

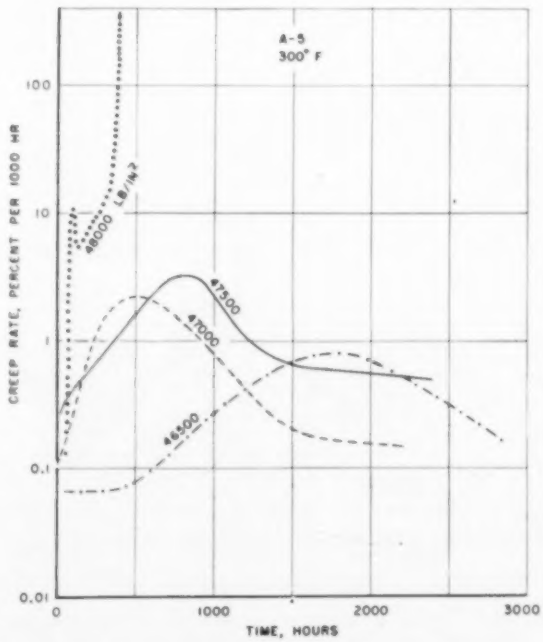


FIGURE 19. *Creep rate-time relation of a specimen tested at 300° F and with increasing stress levels.*

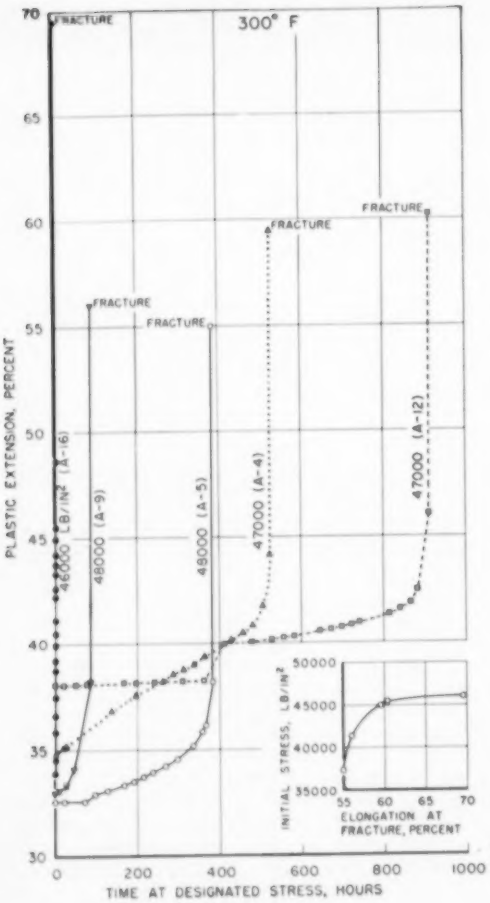


FIGURE 20. *Effect of rate of loading to different stresses on the extension-time curves for specimens fractured at 300° F.*

Refer to tables 1 and 2 and figure 18 for schedule of loading to the designated creep stress.

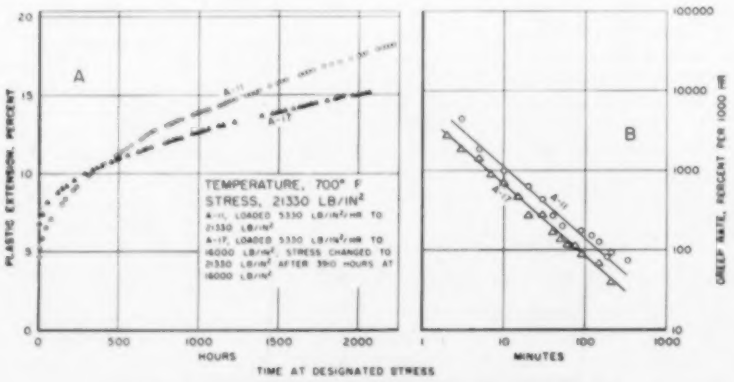


FIGURE 21. *Effect of rate of loading to a stress of 21,330 lb/in.² on the extension-time and creep-rate–time curves for specimens at 700° F.*

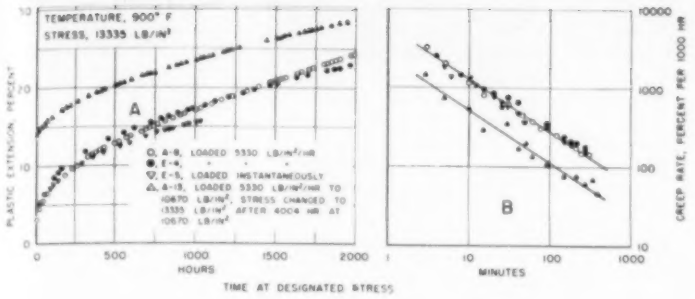


FIGURE 22. *Effect of rate of loading to a stress of 13,335 lb/in.² on the creep characteristics during the first and second stages for specimens at 900° F and on reproducibility of test results.*

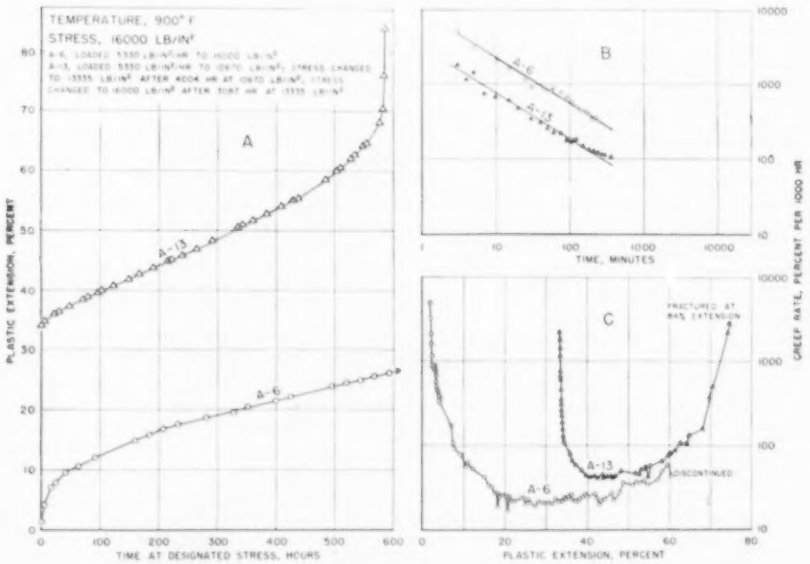


FIGURE 23. *Effect of rate of loading to a stress of 16,000 lb/in.² on the creep of specimens at 900° F.*

Time values do not include 63.75 hr at zero stress (table 2).

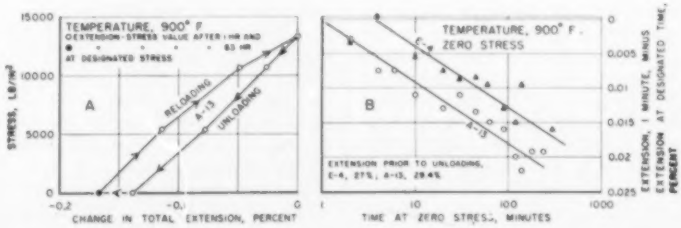


FIGURE 24. *Some relaxation characteristics of the nickel at 900° F.*

42,600, 45,000, 45,500, or 46,000 lb/in.$^2$ (specimens numbered A–5, A–9, A–4, A–12, and A–16, respectively) were attained. Thereafter, the changes in stress were made at the times designated on the curves. If the creep rate, deformation characteristics, and ductility of the high-purity nickel were independent of prior-strain history, then the creep curves would be alike at any one of the selected stress levels. That is, the extension-time curves for all the specimens tested at a selected stress would coincide either as constructed or by the transposition of the initial extension values to those corresponding to the zero time ordinates at this stress. However, an actual comparison of these curves for any selected stress level shows that the creep varied markedly with rate of loading. For example, at a nominal stress of 46,000 lb/in.$^2$, specimen A–16, which was loaded relatively rapidly, fractured in 3.66 hr, whereas specimen A–5, which was loaded slowly, did not fracture in 3,982 hr at this stress. This difference in creep rate is primarily attributed to a combination of strain-aging and strain-hardening characteristics of the nickel. At 300° F, the strain aging and hardening is considerably more prominent in the specimens loaded slowly than in the specimens loaded rapidly to the selected creep stresses. Although the tensile strength of the nickel at 300° F is 46,400 lb/in.$^2$ [3], it is noteworthy that the creep life was appreciable in some of the specimens tested at stresses in excess of this value.

Lubahn [13] made a review of the literature and discussed the strain-aging effects in both nonferrous and ferrous materials. He relates the effects to yield-point phenomenon, strengthening (increase in flow stress or hardness), discontinuous yielding (serrated stress-strain curves, etc.), and abnormally low rate sensitivity. Furthermore, he reported that strain aging is of particular importance in creep where the associated strengthening can cause a significant decrease in creep rate.

The effect of prior-strain history on creep behavior is evident from the results summarized in figure 18. The time lag for the initiation and propagation of deformation at a fast rate followed by a slowing down to some nearly constant rate can be considered a fundamental property of metals. The sigmoidal form of the extension-time curve obtained with the high-purity nickel, however, may be modified with changes in the strain history of the nickel and in the magnitude of the stress increments. As the stress was increased on a selected specimen, differences were also obtained in the creep rate-time relationship (fig. 19). Each of these curves showed a definite peak, and the maximum creep rate obtained in this family of curves increased with an increase in creep stress.

Extension-time curves are shown in figure 20 for all the specimens tested to complete fracture in creep at 300° F. The values for time, as plotted in this figure, include only the range after the application of the stress producing fracture, as designated, whereas the extension values also include a summation of all of the prior plastic extension of the specimen. The specimen (A–16), loaded at the standard rate to 46,000 lb/in.$^2$, fractured after a relatively short time at this stress; this creep stress is slightly below that of the tensile strength of the annealed nickel. However, each specimen (A–9, A–5, A–4, and A–12) that was loaded slowly to a stress in excess of the short-time tensile strength had an appreciable life before fracturing. The plastic extension at fracture of the specimens loaded slowly ranged from about 55 to 60 percent, whereas the extension was 69.5 percent for the specimen loaded rapidly. As shown by the curve in the insert, the elongation at fracture increased continuously with increase in the initial creep stress applied by loading to this stress at 5,330 lb/in.$^2$ at 1-hr intervals.

Extension-time curves are shown in figure 21, A, for two specimens at 700° F that were loaded differently to a stress of 21,330 lb/in.$^2$ The greater strain hardening in the specimen (A–17) loaded slowly resulted in the lowering of the curve and rate in the second stage of creep. In loading each specimen, however, the final increment of stress was sufficient to produce a decrease in creep rate with time in the first stage (fig. 21, B). The parallelism of the two curves indicates that there was no appreciable difference in the mechanism of flow of the two specimens in the first stage of creep.

The influence of rate of loading on the creep behavior of the nickel at 900° F is shown by the results of figures 22 and 23 and table 3. The testing program was extended to include duplicate tests on specimens (A–8 and E–4) prepared from two different bars processed from the same heat.

The creep characteristics in both the first and second stages were nearly alike for the two specimens prepared from different bars of the annealed nickel and tested under the same conditions, as is shown by the near coincidence of the curves representing the experimental values (fig. 22A).

At a stress of 13,335 lb/in.$^2$, the primary creep-rate-time curves are nearly parallel (fig. 22B), but the two curves do not coincide. Likewise, at a stress of 16,000 lb/in.$^2$, the curves are again nearly parallel (fig. 23B), but they do not coincide and their slope differs from that of the former curves (fig. 22B). This indicates that the mechanism of deformation in the first stage at 900° F is stress dependent, but at a given stress level, the mechanism is primarily independent of the prior-strain history of the nickel.

Although the wide variations used in the rate of loading the specimens to the relatively low creep stress of 13,335 lb/in.$^2$ affected the creep rate in the second stage (fig. 22A), this effect was not as prominent as that obtained at the lower test temperatures. A comparison of the extension-time curves for the period ranging from 750 to 1,050 hr indicates that the creep rate of the specimen (E–5) loaded instantaneously was somewhat lower than that of the specimens (A–8 and E–4) loaded at the standard rate. The creep rates of the latter specimens were also higher than that of specimen (A–13) loaded slowly. The second-stage creep rate was increased and time to fracture was decreased by decreasing the standard rate of loading to a creep stress of 16,000 lb/in.$^2$ (fig. 23A). This increase in creep rate and decrease in

time to fracture can be attributed to a difference in amount of plastic deformation of the specimens at the time of applying the creep stress of 16,000 lb/in.$^2$.

A specimen (A–13) was unloaded from a stress of 13,335 lb/in.$^2$ and allowed to relax at zero stress before reloading at the standard rate to the above stress; its temperature was maintained at 900° F. The hysteresis loop (fig. 24,A) obtained was closed, thus indicating no change in the extension value at the attainment of the final creep-stress level. However, the slopes of the curves for the conditions of unloading and reloading (fig. 24,A) and also for initial loading (fig. 1) were not parallel. The effect of time on change in extension at zero stress for this specimen and another specimen (E–4) that had been tested in creep to approximately the same extension is shown in figure 24,B. The parallelism of the curves indicates that the mechanism of relaxation was similar for the two specimens. The second-stage creep rate of specimen A–13 (table 2) at a stress of 13,335 lb/in.$^2$ was slightly lower after the above cycle of unloading and reloading.

The hysteresis loop previously obtained with oxygen-free high-conductivity copper was not closed [1]. Apparently, both the chemical composition and prior-strain history of the materials affect this phenomenon.

Thus, the influence of rate of loading on creep behavior of the initially annealed nickel depended not only upon the strain, temperature, and stress, but also on the magnitude of the aging, strain hardening, and recovery that occurred in the temperature range investigated. The results again serve to emphasize the importance of controlling the rate of loading in creep testing.

### 4.3. Effect of Prestraining in Creep on the Mechanical Properties at Room Temperature

Tension tests were made at room temperature on specimens prestrained different amounts in creep at 900° F and also on specimens prestrained in creep at 700° or 900° F and then annealed at 1,750° F. The results are summarized in figures 25 and 26 and in table 3.

The influence of prestraining in creep at 900° F on the resistance to flow in tension at room temperature is illustrated by a comparison of the relative positions of the curves of figure 25. The resistance to the initiation of flow was decreased somewhat by deforming 12- or 19-percent reduction of area in creep, but the resistance to flow for strains within the range of about 0.02 to 0.3 increased with the amount of prestraining in creep. However, at still higher strains the flow curves intersect for specimens prestrained 12 and 19 percent in creep, respectively.

The yield and tensile strengths increased continuously with the amount of prestraining at 900° F (table 3). This increase in the strength properties was accompanied by a corresponding decrease in strain at maximum load, at the beginning, and at complete fracture. The inconsistencies observed in this pattern for the values of true stress at the beginning or at complete fracture can be attributed to

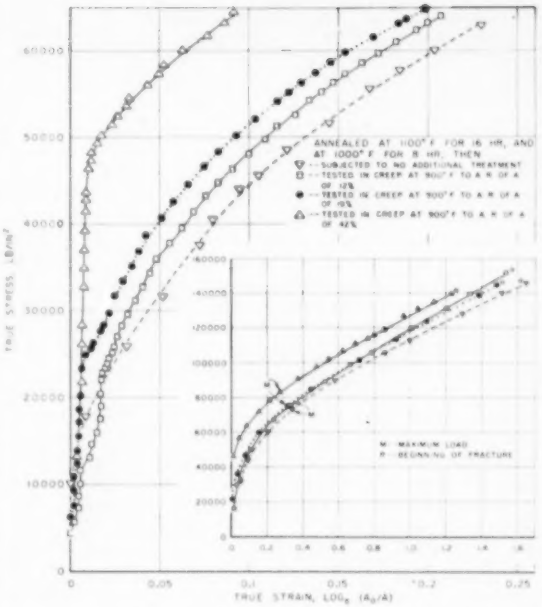
TRUE STRESS, LB/IN²
TRUE STRAIN, LOG$_e$ (A$_o$/A)
ANNEALED AT 1100° F FOR 16 HR, AND AT 1000° F FOR 8 HR, THEN
SUBJECTED TO NO ADDITIONAL TREATMENT
TESTED IN CREEP AT 900° F TO A R OF A OF 12%
TESTED IN CREEP AT 900° F TO A R OF A OF 42%
M - MAXIMUM LOAD
R - BEGINNING OF FRACTURE

FIGURE 25. *Influence of prior deformation in creep at 900° F on the true-stress–true-strain curves for specimens tested in tension at room temperature.*

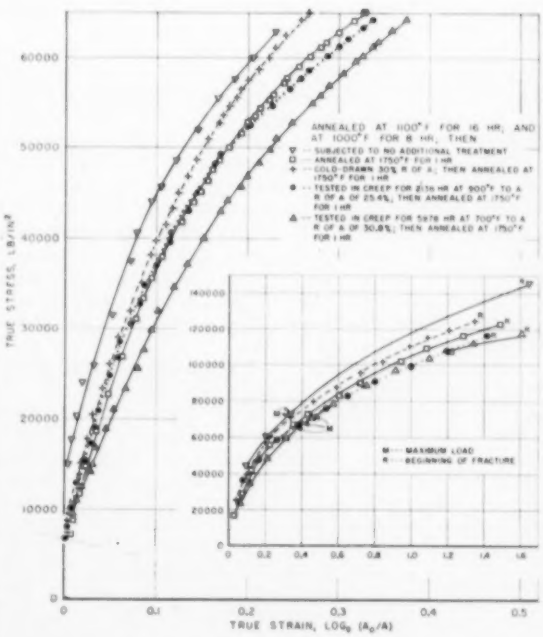
TRUE STRESS, LB/IN²
TRUE STRAIN, LOG$_e$ (A$_o$/A)
ANNEALED AT 1100° F FOR 16 HR, AND AT 1000° F FOR 8 HR, THEN
SUBJECTED TO NO ADDITIONAL TREATMENT
ANNEALED AT 1750° F FOR 1 HR
COLD-DRAWN 30% R OF A; THEN ANNEALED AT 1750° F FOR 1 HR
TESTED IN CREEP FOR 2236 HR AT 900° F TO A R OF A OF 25.4%; THEN ANNEALED AT 1750° F FOR 1 HR
TESTED IN CREEP FOR 5878 HR AT 700° F TO A R OF A OF 30.8%; THEN ANNEALED AT 1750° F FOR 1 HR
M - MAXIMUM LOAD
R - BEGINNING OF FRACTURE

FIGURE 26. *Influence of prior-strain history followed by annealing at 1,750° F on the true-stress–true-strain curves for specimens tested in tension at room temperature.*

variations in the necking characteristics of the different specimens. The values obtained for reduction of area (total of creep and room temperature tensile) were independent of the prior-strain history.

Increasing the annealing temperature from 1,100° to 1,750° F decreased the resistance to flow at room temperature of the nickel (fig. 26); this increase in annealing temperature was accompanied by an increase in grain size. The resistance to flow at room temperature was further reduced by prestraining a specimen to 30.8-percent reduction of area in creep at 700° F before annealing at 1,750° F (see table 3); this decrease was accompanied by an increase in strain at maximum load. However, prestraining to 25.4-percent reduction of area at 900° F followed by annealing at 1,750° F did not materially affect the position of the true-stress–true-strain curve for strains ranging up to about 0.3 (maximum load). Above this range, the curves for the two specimens prestrained in creep were nearly alike. The flow curve for the specimen cold-drawn 30-percent reduction of area before annealing at 1,750° F is located between the curves for the specimens annealed only at 1,750° or 1,100° F. Evidently, the effects of the cold-working, such as preferred orientation and elongation of the grains, were not completely removed by subsequent annealing at the relatively high temperature.

The effects of prestraining the nickel in creep at different temperatures and rates and in tension at room temperature on the necking characteristics and on the Rockwell B hardness at room temperature are shown by the results summarized in figure 27.

It is apparent that the general tendency was for the nickel to neck sharply before fracturing in creep (fig. 27,A) or in tension at room temperature (fig. 27,C). However, one specimen (A–22) with a slow creep rate at 1,200° F fractured with a relatively small amount of local necking (fig. 27,A). The necking characteristics observed for the specimens tested at 300° F were independent of the rates of loading used (insert, fig. 27,A). For the specimens fractured at room temperature, the tendency toward localized necking was a minimum in the specimen (C–9) annealed at 1,100° F and a maximum in the specimen (A–6) prestrained to 42-percent reduction of area in creep at 900° F (fig. 27,C).

The hardness at room temperature of each specimen fractured in creep at 300°, 700°, or 900° F increased with an increase in the amount of deformation in the vicinity of complete fracture (fig. 27,B). These curves are nearly parallel, but their relative positions varied with the test temperatures and creep rates. The trend was for the curves to be displaced to higher values as the creep temperature was decreased and the creep rate was increased. The hardness of the specimen (A–20) fractured at 1,200° F with a relatively high secondary creep rate of 500 percent per 1,000 hr also increased with increase in deformation at fracture, but the curve was displaced to considerably lower values than the corresponding curves for specimens tested at the lower temperatures. However, the trend was for the hardness of the other two specimens (A–21 and A–22), tested at 1,200° F with slower secondary creep rates, to decrease as the deformation in the vicinity of fracture increased. As previously pointed out, 1,200° F is above the recrystallization temperature of nickel. Whether the combination of recrystallization and recovery or strain hardening predominated at 1,200° F depended upon the creep rate or time in the third stage of creep. Evidently, strain hardening predominated in the former specimen, whereas recovery and recrystallization predominated in the latter two specimens. The rate of loading at 300° F had no material effect on the subsequent hardness induced by deforming in tension at room temperature.

As is to be expected, the hardness of all the specimens tested in tension at room temperature increased continuously with increase in deformation (fig. 27,D). However, the relative positions of the hardness–reduction-of-area curves varied with the prior-strain history of the nickel. Prestraining in creep at 900° F, without subsequent annealing, resulted in a general trend of raising the positions of these curves as the amount of prestraining increased. Increasing the annealing temperature from 1,100° to 1,750° F had no significant effect on the hardness–reduction-of-area relationship at room temperature (specimens C–9 and A–19, respectively). This relationship was also unaffected by cold-drawing 30-percent reduction of area followed by annealing at 1,750° F (specimens 631–A and A–19, respectively). However, prestraining a specimen to 30.8-percent reduction of area into the third stage of creep at 700° F before annealing at 1,750° F had the over-all effect of decreasing the resistance to hardening induced by deforming in tension at room temperature (specimens A–17 and 631–A).

### 4.4 Effect of Creep Conditions on Fracture Characteristics and Structures

The effect of temperature on the appearance of the specimens fractured in creep at relatively high rates is illustrated in figure 28. Each of these specimens exhibited a ductile fracture, a rim effect, and both circumferential and longitudinal flow lines on the surface. No evidence of surface cracking was observed in the specimens fractured at 300° or 700° F, whereas numerous cracks were formed in the surface of the specimens fractured at 900° F. Surface cracking was accentuated by further increasing the test temperature to 1,200° F (fig. 29,A) and by decreasing the creep rate at this temperature (fig. 29). The presence of numerous surface cracks, however, was not always accompanied by brittle behavior, as determined by the appearance of flow lines and by a measurement of the reduction of area at fracture. This is evident by a comparison of the appearance of the specimens tested at the fast or intermediate creep rate at 1,200° F (fig. 29,A and B) with that of the specimens tested at high creep rates at 300° or 700° F (fig. 28,A and B). Despite the presence of the surface cracks in the former specimens, it is believed that the cracks linking up to form complete rupture were initiated at or near the axis of the

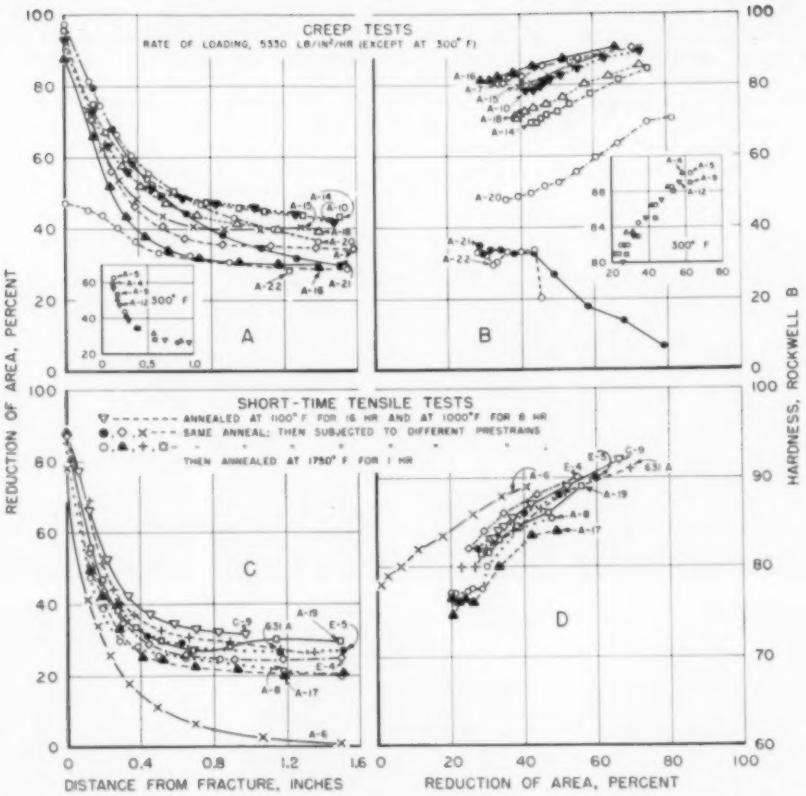
CREEP TESTS
RATE OF LOADING, 5330 LB/IN²/HR (EXCEPT AT 300° F)
A
B
300° F
SHORT-TIME TENSILE TESTS
ANNEALED AT 1100° F FOR 16 HR AND AT 1000°F FOR 8 HR
SAME ANNEAL; THEN SUBJECTED TO DIFFERENT PRESTRAINS
THEN ANNEALED AT 1750° F FOR 1 HR
C
D
REDUCTION OF AREA, PERCENT
HARDNESS, ROCKWELL B
DISTANCE FROM FRACTURE, INCHES
REDUCTION OF AREA, PERCENT

FIGURE 27. *Effects of temperature, prior-strain history, and creep rate on specimen contour and distribution of hardness of specimens fractured in creep or in tension at room temperature.*

| Creep (A and B) | | | Tensile (C and D) | | | |
|---|---|---|---|---|---|---|
| Specimen | Temperature | Second-stage creep rate | Specimen | Creep test | | Additional thermal treatment prior to tensile test |
| | | | | Temperature | Reduction of area | |
| | °F | %/1,000 hr | | °F | % | |
| A-16 | 300 | 2100 | C-9 | None | None | None. |
| A-7 | 700 | 1020 | E-5 | 900 | 12 | Do. |
| A-15 | 700 | 120 | E-4 | 900 | 19 | Do. |
| A-10 | 700 | 33.3 | A-6 | 900 | 42 | Do. |
| A-18 | 900 | 620 | A-19 | None | None | Annealed at 1,750° F. |
| A-14 | 900 | 238 | 631-A | do | do | Annealed at 1,750° F after cold-drawing 30% reduction of area. |
| A-20 | 1,200 | 500 | | | | |
| A-21 | 1,200 | 62.5 | A-8 | 900 | 25.4 | Annealed at 1,750° F. |
| A-22 | 1,200 | 16.5 | A-17 | 700 | 30.8 | Do. |

See table 2 for rate of loading of specimens A-4, A-5, A-9, and A-12.

specimen and then propagated outward to the surface (rim effect). However, extensive surface cracking and a relatively brittle fracture were obtained in the specimen tested at a slow creep rate at 1,200° F (fig. 29,C). The evidence indicates that cracking started at or near the surface of this specimen and then propagated to its axis. Thus, the surface appearance of a failed specimen does not necessarily reveal its behavior in creep.

The grains were nearly equiaxed in the annealed nickel (fig. 30,A). These grains were elongated during creep, but the degrees of distortion and strain markings vary with the test temperature and creep rates. The trend was for the distortion and strain markings in the region of complete fracture to be accentuated by decreasing the secondary creep rate within the range used at 700° or 900° F (fig. 30,C, D, E, and F). Distortion of the grains at fracture was

somewhat less severe in the specimen tested at 300° F at a relatively high rate (fig. 30,B) than in the specimens fractured at either 700° or 900° F. Furthermore, the number of microcracks observed in the vicinity of complete fracture was a minimum in the specimens fractured at 300° F, intermediate at 900° F, and a maximum at 700° F. If cracks of microscopic dimension are a prerequisite for the beginning of the third stage, then it is to be expected that cracks also would be observed in regions other than at complete fracture. However, no microcracks were detected in these nickel specimens fractured in creep except in the region of complete fracture.

No indication of recrystallization was observed in a metallographic study of the specimens fractured at 300°, 700°, or 900° F; the failures were probably transcrystalline.

Strain marking and distortion of the grains at fracture were less prominent in the specimens tested

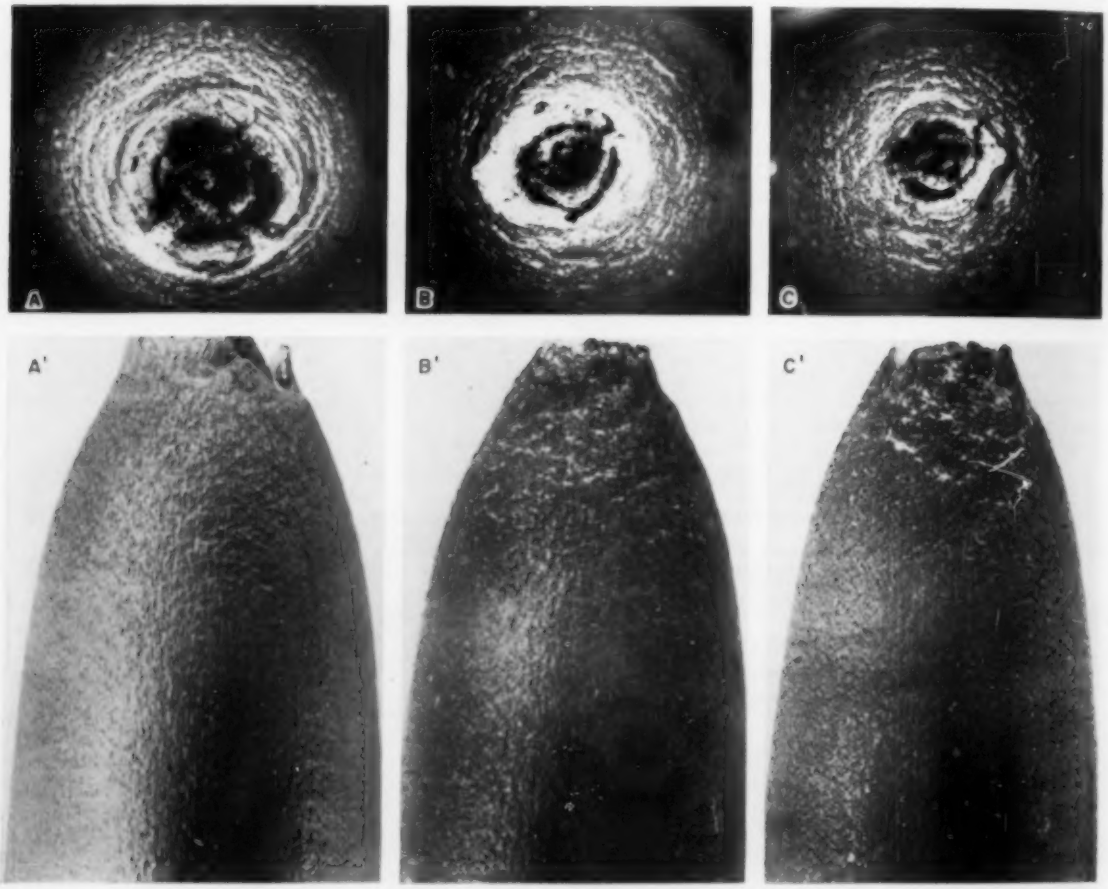


FIGURE 28. *Specimens fractured in creep at different temperatures.*

Unetched, × 6.

| | Test | | Plastic extension in 2 in. | Reduction of area |
|---|---|---|---|---|
| | Temperature | Rate | | |
| | ° F | %/1,000 hr | % | % |
| A, A' | 300 | 2,100 | 69.5 | 87.6 |
| B, B' | 700 | 1,020 | 73 | 92.9 |
| C, C' | 900 | 620 | 102.5 | 95.9 |

at 1,200° F (fig. 31) than in the specimens fractured at the lower temperatures (fig. 30). Moreover, the size of the grains at 1,200° F varied appreciably with creep rate and also from surface to center in one specimen. Decreasing the secondary creep rate from 500 percent to 10.5 percent per 1,000 hr was accompanied by an appreciable increase in grain size and a general deterioration at fracture (fig. 31,A and B). The grain size in the vicinity of fracture of the latter specimen varied markedly from its center to its surface (fig. 31,B and C, respectively). This may be interpreted as supporting the belief that the final fracture was initiated at or near the surface (large grains) and then propagated to the axis (small grains). As 1,200° F is above the recrystallization temperature of nickel, it seems feasible

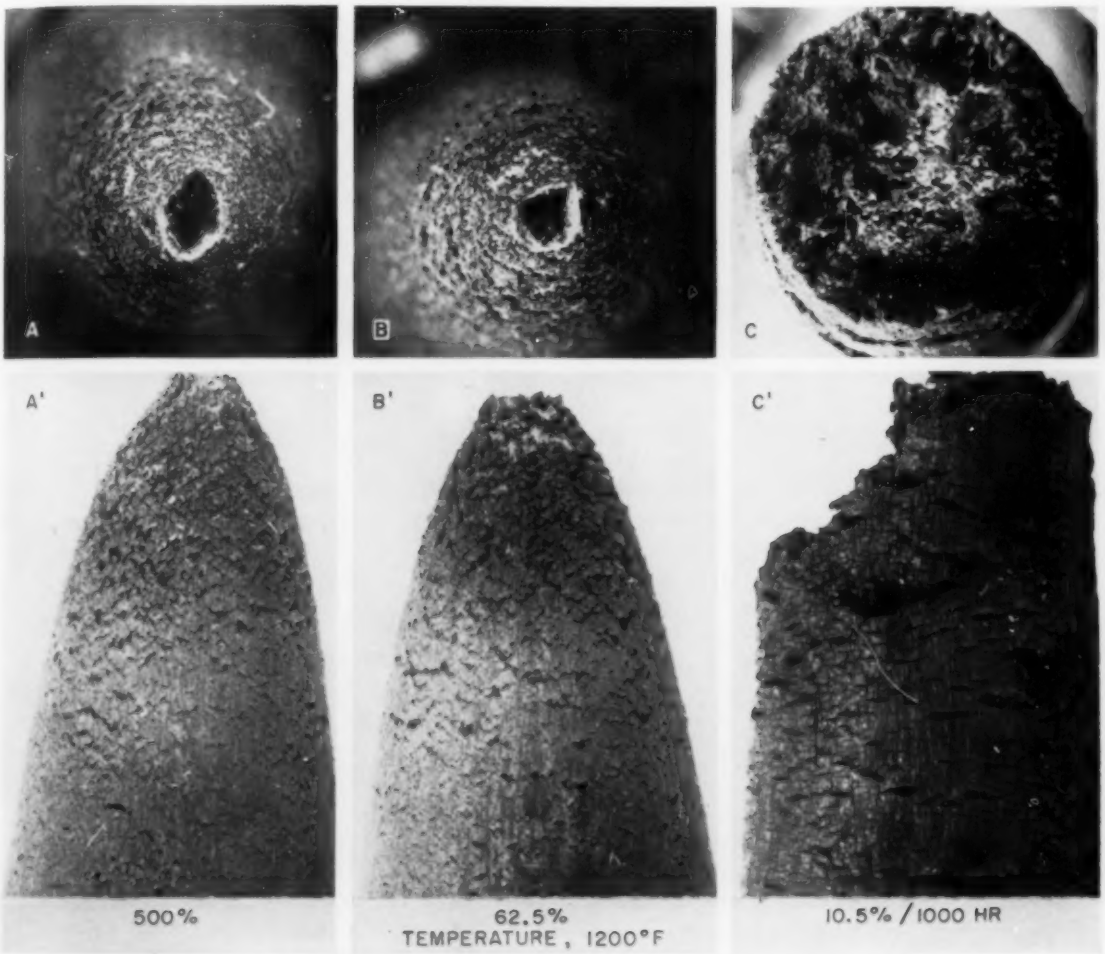


FIGURE 29. *Specimens fractured at 1,200° F at different rates.*

Unetched, × 6.

| | Creep rate | Plastic extension in 2 in. | Reduction of area |
|---|---|---|---|
| | %/1,000 hr | % | % |
| A, A' | 500 | 91 | 97.4 |
| B, B' | 62.5 | 87 | 98.1 |
| C, C' | 10.5 | 66 | 47.1 |

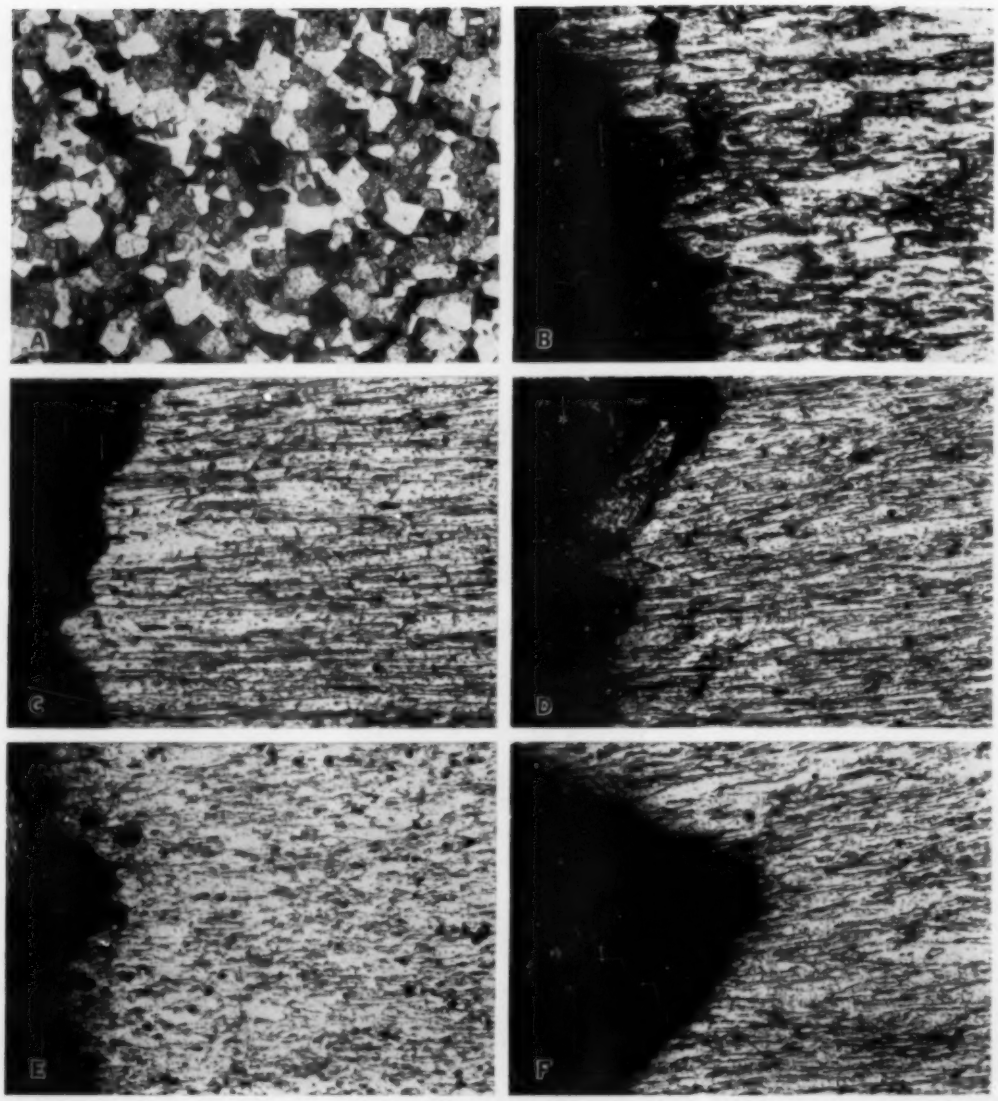


FIGURE 30. *Structure of the nickel as annealed and after fracturing in creep at different temperatures and rates.*

Longitudinal sections etched in 6 parts of $HNO_3$ (concentrated) and 4 parts of glacial ascetic acid.

| | Test | | Plastic extension in 2 in. | Reduction of area | Remarks |
|---|---|---|---|---|---|
| | Temperature | Creep rate | | | |
| | ° *F* | %/1,000 *hr* | % | % | |
| A | | | | | × 75; as annealed. |
| B | 800 | 2,100 | 69.5 | 87.6 | × 100; near axis at fracture. |
| C | 700 | 120 | 91 | 93.4 | Do. |
| D | 700 | 33.3 | 99.5 | 92.3 | Do. |
| E | 900 | 620 | 102.5 | 95.9 | Do. |
| F | 900 | 238 | 107.5 | 95.8 | Do. |

that the freshly fractured and nearly strain-free recrystallized grains at the surface continued to grow while the normal process of strain hardening, recovery, and recrystallization was occurring in the unfractured interior of the specimen. The relatively rapid grain growth after the final recrystallization is even more apparent at the surface 0.1 in. from complete fracture of this specimen (fig. 31,D).

The fractures at 1,200° F appeared predominantly intercrystalline, although some transcrystalline cracking was observed.

Typical microstructures observed in a specimen taken from a test bar that had been strained into the third stage of creep at 900° F and then fractured in tension at room temperature are illustrated in the photomicrographs of figure 32. The microcracks

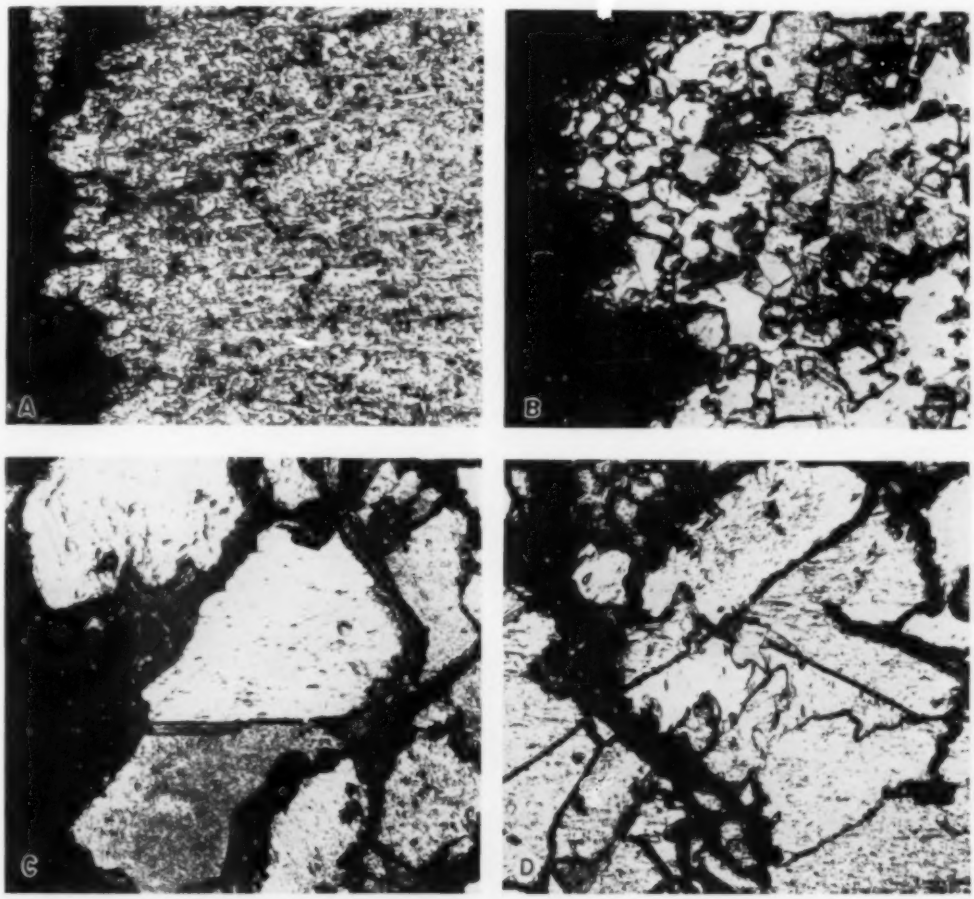


FIGURE 31. *Structure of the nickel after fracturing in creep at different rates at 1,200° F.*

Longitudinal sections etched in 6 parts of $HNO_3$ (concentrated) and 4 parts of glacial acetic acid. × 100.

| | Creep rate | Remarks |
|---|---|---|
| | *%/1,000 hr* | |
| A | 500 | Near axis at fracture. |
| B | 10.5 | Do. |
| C | 10.5 | Same specimen as B; near outer surface at fracture. |
| D | 10.5 | Same specimen as B; near outer surface, 0.1 in. from fracture. |

were located near the axis of the specimen, and they were confined principally within the region of complete fracture; the cracks were of the elliptical type. The extensive flow that occurred at the outer surface and the general disintegration at the axis of the specimen indicate that the cracking leading to complete rupture was initiated at the center and then progressed outward. An oxide film formed on the specimen during the time of exposure in air at 900° F. This film was fractured in the tension test at room temperature (fig. 32,C and D), but apparently it had no significant effect on the mechanism of the final fracture. Extensive strain markings and some distortion of the parent grains are also evident some distance from complete fracture (fig. 32,E and F).

In a specimen that was strained into the third

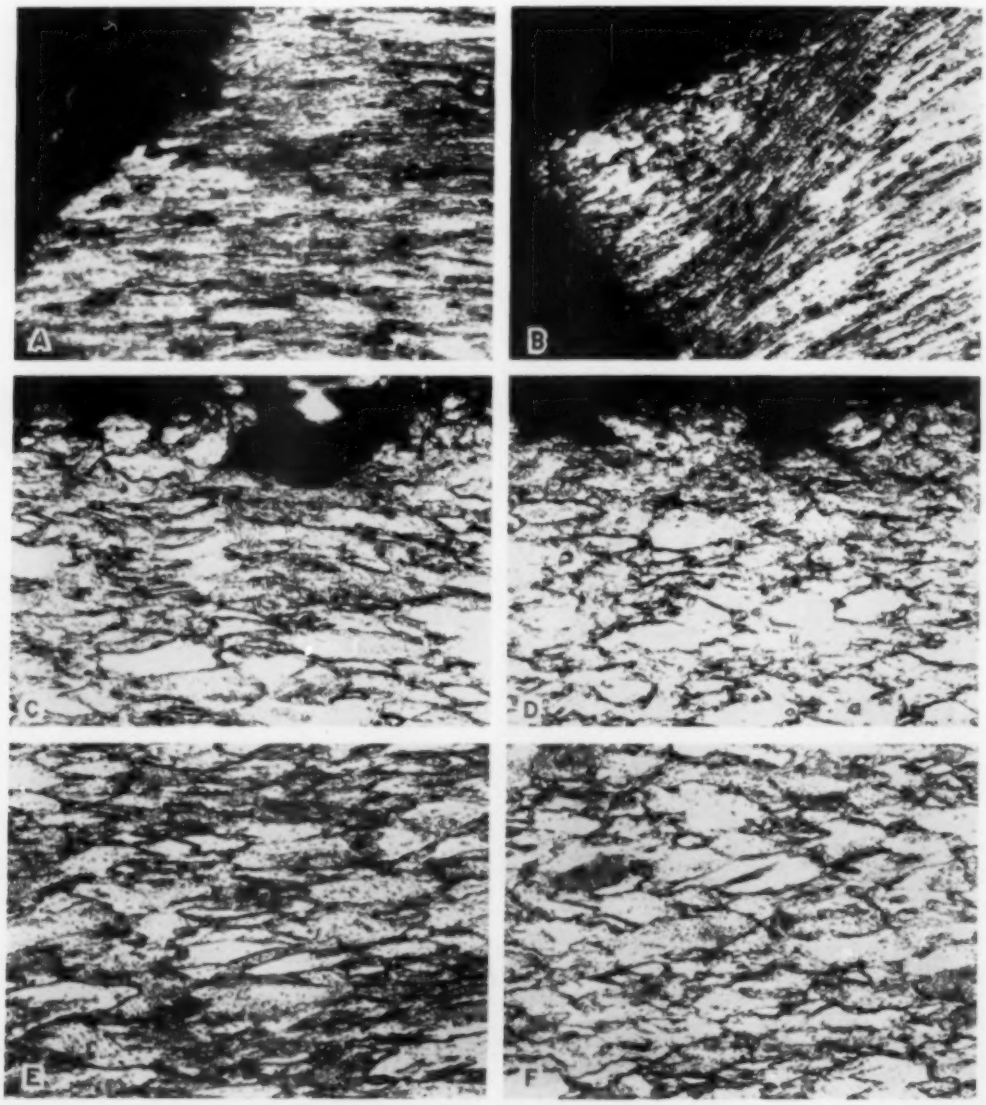


FIGURE 32. *Structure of a specimen strained in creep at 900° F and then fractured in tension at room temperature.*

Longitudinal sections, etched in 6 parts of concentrated nitric and 4 parts of glacial acetic acids. × 100.
A, Near axis at fracture; B, near outer surface at fracture; C, near outer surface 0.1 in. from fracture; D, near outer surface 0.3 in. from fracture; E, near axis 0.1 in. from fracture; F, near axis 0.3 in. from fracture.

stage of creep at 700°, then annealed at 1,750° F before fracturing in tension at room temperature, the fracture was transcrystalline (fig. 33,A). The pronounced elongation of the grains at the outer surface and the intensification of strain marking within these grains (fig. 33,B) also indicate that the fracture of this specimen started at or near the axis and propagated outward. It is of interest to note that no general disintegration occurred in this specimen and the wavy strain markings or bands become wider as the distance from complete fracture is increased up to 0.3 in. (fig. 33,A, C, and D). Some of the strain markings also cross the grain boundaries, as is clearly illustrated in figure 33,C.

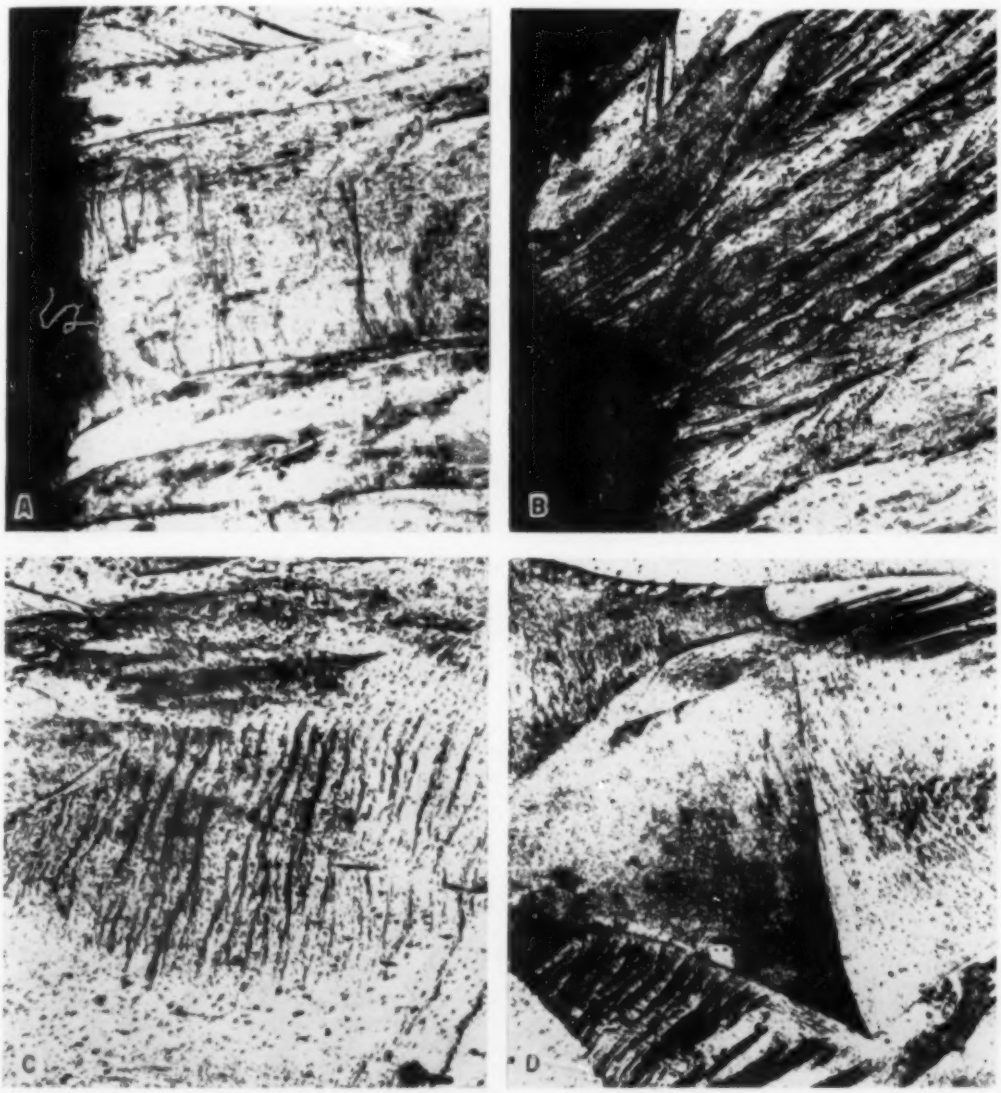


FIGURE 33. *Effect of intermediate annealing at 1,750° F on the structure of a specimen previously extended in creep at 700° F and subsequently fractured in tension at room temperature.*

Longitudinal sections etched in 6 parts of concentrated nitric and 4 parts of glacial acetic acid. × 100.
A, Near axis at fracture; B, near outer surface at fracture; C, near axis 0.1 in. from fracture; D, near axis 0.3 in. from fracture.

## 5. Summary

Tests were made to determine the influence of stress, temperature, and prior-strain history on the creep behavior of initially annealed high-purity nickel. An evaluation was also made of the effect of prestraining in creep, with and without subsequent annealing, on the hardness and tensile properties at room temperature. A metallographic study was made of all the specimens fractured in creep and of specimens fractured in tension at room temperature after prestraining in creep. The results are summarized in figures and tables and discussed in some detail in the text.

Discontinuous flow was observed in creep at 300°, 700°, 900°, and 1,200° F. The magnitude and position of the serrations in the creep-rate–extension curves varied with the test temperatures, and they were affected by such factors as strain aging, strain hardening, recovery, Curie-point behavior, recrystallization, and grain growth.

The experimental values for primary creep agreed fairly closely with the results predicted by the theory of exhaustion and generation of dislocations as proposed by Mott and Nabarro and modified by others.

Although the resistance of the nickel to creep increased as the test temperature decreased, the resistance was especially high at a temperature of 300° F. This high resistance is attributed to a combination of strain aging and age hardening and relatively low rate of recovery. The phenomenon of strain aging was especially prominent in the creep tests carried out at 300° F. Nonlinear relations were generally obtained between the stress and secondary creep rate when the experimental values were plotted on log-log or semilog (log of rate) bases. Moreover, the second-stage creep rate was not a consistent index to the ductility of the nickel at the beginning of the third stage of creep or at fracture.

The ductility at fracture was relatively high for all creep conditions except for one specimen that showed evidence of brittle behavior. This specimen was tested at 1,200° F at a slow secondary creep rate, and it showed a general deterioration at the time of fracture. Internal disintegration was confined to the region of complete fracture in all the specimens tested in creep at 300°, 700°, or 900° F, and the fractures were preceded by appreciable necking. Cracks of microscopic dimensions were not a prerequisite for the initiation of the third stage of creep.

The yield and tensile strengths of specimens tested in tension at room temperature increased with the amount of prestraining in creep at 900° F. This increase in strength properties at room temperature was accompanied by a decrease in elongation, whereas the total reduction of area was independent of the prior-strain history.

The Rockwell B hardness at room temperature of each specimen fractured in creep at 300°, 700°, or 900° F increased with an increase in deformation in the vicinity of complete fracture. This trend was also observed in a specimen tested at a relatively high secondary creep rate at 1,200° F, but with slower rates at this temperature, the hardness decreased as the deformation increased in the vicinity of fracture.

Recrystallization occurred in the specimens fractured in creep at 1,200° F; in some cases, recrystallization was accompanied by grain growth. However, no evidence of recrystallization was detected in a metallographic study of all the specimens fractured in creep at the lower temperatures. The fractures appeared to be predominantly transcrystalline at 300°, 700°, or 900° F and intercrystalline at 1,200° F.

The prior-strain history of the nickel also had a very marked effect on the second-stage creep rate, and the experimental results again serve to emphasize the importance of controlling the rate of loading in creep testing.

## 6. References

[1] William D. Jenkins and Thomas G. Digges, Creep of high-purity copper, J. Research NBS **45,** 153 (1950) RP2121.

[2] William D. Jenkins and Thomas G. Digges, Creep of annealed and cold-drawn high-purity copper, J. Research NBS **47,** 272 (1951) RP2254.

[3] William D. Jenkins and Thomas G. Digges, Effect of temperature on the tensile properties of high-purity nickel, J. Research NBS **48,** 313 (1952) RP2317.

[4] William D. Jenkins and Thomas G. Digges, Influence of prior strain history on the tensile properties and structures of high-purity copper, J. Research NBS **49,** 167 (1952) RP2354.

[5] M. W. Nathans, E. L. Parker, and T. H. Hazlett, A survey of theories of creep of metals, First Technical Report Under U. S. Atomic Energy Commission Contract AT–11–1–Gen 10, Project 1 (Nov. 15, 1949).

[6] A. D. Schwope and L. R. Jackson, A survey of creep in metals, NACA Tech. Note 2516 (Nov. 1951).

[7] T. H. Hazlett and E. R. Parker, Nature of the creep curve, J. Metals **5,** 318 (Feb. 1953).

[8] Metals Handbook, 1047 (1948).

[9] W. Köster, Die Temperaturabhängigkeit des Elastizitätsmoduls reiner Metalle, Z. Metallkunde **39,** 1 (1948).

[10] N. F. Mott and F. R. N. Nabarro, Dislocation theory and transient creep, Report of a Conference on Strength of Solids, Phys. Soc. p. 1 (1948).

[11] E. N. da C. Andrade, The creep of metals, Report of a Conference on Strength of Solids, Phys. Soc., p. 20 (1948).

[12] M. Davis and N. Thompson, Creep in a precipitation-hardened alloy, Proc. Phys. Soc. [B] **63,** 847 (1950).

[13] J. D. Lubahn, Strain aging effects, Trans. Am. Soc. Metals **44,** 643 (1952).

WASHINGTON, May 26, 1954.

rnal of Research of the National Bureau of Standards Vol. 53, No. 6, December 1954 Research Paper 2552

# Determination of Nickel, Manganese, Cobalt, and Iron in High-Temperature Alloys, Using Anion-Exchange Separations

John L. Hague, Edwin E. Maczkowske, and Harry A. Bright

A procedure is given for the determination of nickel, manganese, cobalt, and iron in a high-temperature alloy. Niobium, tantalum, tungsten, and silicon are rendered insoluble by hydrochloric acid dehydration after solution of the alloy in aqua regia. Molybdenum and copper are precipitated with hydrogen sulfide, and the solution is filtered. The filtrate is evaporated several times with hydrochloric acid and hydrogen peroxide to obtain a chloride solution of these elements in the proper valence. The resulting solution is transferred to an anion-exchange column containing Dowex-1. The nickel and manganese, with chromium and some other elements, are collected in the first fraction by elution with 9 *N* hydrochloric acid. Cobalt is collected in a second fraction by elution with 4 *N* hydrochloric acid, and iron in a third by elution with 1 *N* hydrochloric acid. The cobalt is determined by electrolysis from a weakly ammoniacal chloride solution containing hydroxylamine hydrochloride, and the other elements are determined by conventional methods.

## 1. Introduction

The increased use in recent years of high-temperature alloys and alloys of controlled temperature-expansion characteristics has made the problem of determining cobalt, iron, nickel, and manganese in appreciable quantities and in combination a pressing one. Some of the difficulties encountered in this field of analysis have been summarized by Chirnside, Cluley, and Proffitt [3] [1] in dealing with a ternary alloy of iron, nickel, and cobalt. Many of the alloys manufactured today may contain, in addition, appreciable percentages of chromium, molybdenum, titanium, tungsten, niobium, and other elements. The problem of obtaining analyses of sufficient accuracy for the establishment of standards of composition is not an easy one; even the usually simple determination of nickel may become quite complex in these mixtures [7]. A new approach to the problem seems needed in order to put such methods on a basis of accuracy comparable to other less difficult combinations.

The present paper describes the application of anion-exchange separations to the analysis of high-temperature alloys. Kraus and Moore [8, 12] have shown that nickel, manganese, cobalt, and iron, as well as certain other elements, can be separated by selective elution from an anion-exchange resin with hydrochloric acid solutions. These separations depend on the fact that a number of metallic elements [10] can exist in aqueous solutions either as cations or as complex chloro-anions, the relative amounts depending on the element and on the concentration of chloride ions in the solution. The exact mechanism of the combination (or adsorption) of these complexes with the resin has not been established, but it may be related to the existence of these complex anions in solution as strong acids. For example, iron is probably combined in the form of a complex anion, such as $(H_2FeCl_6)^-$, that is free to compete with the chloride ions for a position on the resin column, much as the competition that exists between chloride and bisulfate ions [9]. Though suggested mechanisms are at present speculative, practical and efficient quantitative separations can be made with quantities and volumes commonly used in analytical work.

The procedure outlined below was designed particularly with the analysis of an S–816 type of alloy [2] in mind. After solution of the alloy in aqua regia, the niobium, tantalum, tungsten, and silicon are rendered insoluble by hydrochloric-acid dehydration. The solution is treated with hydrogen sulfide to precipitate molybdenum and copper, and filtered. The filtrate is evaporated several times with hydrochloric acid and hydrogen peroxide to obtain a chloride solution of the elements in the proper valence. The resulting solution is transferred to an anion-exchange column, and the nickel and manganese, with chromium and some other elements, are collected in the first fraction by elution with 9 *N* hydrochloric-acid solution. Cobalt is collected in a second fraction by elution with 4 *N* hydrochloric acid, and iron in a third by elution with 1 *N* hydrochloric acid. Manganese and nickel are determined in aliquots of the first fraction by the persulfate-arsenite titration and dimethylglyoxime gravimetric methods, respectively. Cobalt is determined in the second fraction by electrolysis from a weakly ammoniacal chloride solution containing hydroxylamine hydrochloride, and iron is determined in the third fraction by reduction with stannous chloride and titration with dichromate.

The method requires several days to carry to completion as about 3 hr are required for each of the ion-exchange fractionations. The method is not intended to replace rapid routine procedures, where they can be developed for a particular type [3] of material, but provides an independent checking procedure of general application.

[1] Figures in brackets indicate the literature reference at the end of this paper.

[2] This alloy contains approximately 40 percent of cobalt, 20 percent of nickel, 20 percent of chromium, and 4 percent each of niobium, tungsten, and molybdenum, the remainder being largely iron, manganese, carbon, and silicon.

## 2. Apparatus and Resins

The apparatus required for an ion-exchange separation is simple, consisting of a glass column to hold the resin. The column used in this investigation, illustrated in figure 1, is 1 in. in internal diameter and 12 in. long. As most of these separations require several hours, it is convenient to so arrange the columns that a number can be operated with minimum attention. Such an assembly is illustrated in figure 2. The solutions necessary for elution are delivered by gravity flow from bottles, placed on the top stand, through a system of stopcocks and capillary tubing, to the columns. Because most of the usable resins are fine-mesh materials that tend to slow the flow of liquid, it is advantageous to have a several-foot head of liquid to control the flow rate.

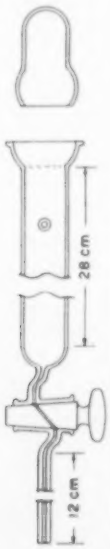


FIGURE 1. *Ion-exchange column.*

FIGURE 2. *Assembly of ion-exchange columns.*

The resin selected for these columns was 200- to 400-mesh Dowex–1, with 8- or 10-percent cross-linkage.[3] The finest and the coarsest materials are removed by settling the resin in diluted hydrochloric acid (1+19).[4] After several cycles of successively decanting the fine and main portions from the coarse fraction, the column is filled with a slurry of the main portion of the resin to a settled height of 20 to 23 cm (equivalent to approximately 75 g of resin). A plug of glass wool in the bottom of the column serves to retain the resin, and a disk of plastic cloth is placed on top to minimize the disturbance of the resin when solutions are added.

## 3. Procedures

### 3.1. Preparation of the Solution of the Sample for Ion-Exchange Separation

Transfer an accurately weighed 1 g sample to a 600-ml beaker. Cover the beaker and add 20 ml of aqua regia (3 parts of hydrochloric acid and 1 part of nitric acid). Set the beaker on the side of a steam bath until the reaction ceases, and then warm it gently until the sample is in solution,[5] except for small amounts of carbides and silica.

Wash the cover glass and wall of the beaker with a little diluted hydrochloric acid (1+19) and evaporate to dryness on a steam bath. Treat the dry residue with 10 ml of diluted hydrochloric acid (1+1), warm and mix well with a glass rod, and again evaporate to dryness. Repeat the addition of diluted hydrochloric acid and the evaporation to dryness four times to insure the removal of nitric acid.[6] Finally, add 15 ml of diluted hydrochloric acid (1+1) and warm the solution on the steam bath until the cake is dissolved. Dilute to 300 ml with hot water, and pass a brisk stream of hydrogen sulfide through the solution for 30 min.[7] Let stand for 30 min and filter through a close-textured 11-cm paper containing a little paper pulp. Transfer the precipitate to the paper[8] and wash with a diluted hydrochloric acid (3+97) solution saturated with hydrogen sulfide until the volume of the filtrate and washings is at least 450 ml. Transfer the filtrate and washings to a steam bath and evaporate to dryness.

[3] The fine-mesh resins were obtained from The Dow Chemical Co., Technical Service and Development, Midland, Mich.

[4] This denotes 1 volume of concentrated hydrochloric acid, sp gr 1.18, diluted with 19 volumes of water. If no dilution is specified, the concentrated reagent is meant.

[5] Some alloys dissolve slowly, but will dissolve more readily if the chlorine generated by the acid mixture is not driven off by heat.

[6] Manganese appears to form a complex chloromanganite anion of unknown composition in strong hydrochloric acid solutions in the presence of oxidizing agents.

[7] Molybdenum is absorbed in part by the ion-exchange column and soon contaminates all fractions during the separation procedure. It is conveniently removed at this point, along with the dehydrated silica, tungsten, tantalum, and niobium.

[8] This paper can be ignited and the residue examined for manganese, nickel, cobalt, and iron. Examination of residues from an S–816 alloy indicated negligible quantities of manganese and iron, 0.01 percent of nickel, and 0.02 to 0.03 percent of cobalt to be retained by this precipitate.

To the residue add 10 ml of diluted hydrochloric acid (1+1), cover the beaker with a watchglass, and warm. Add 50 ml of warm water, and dissolve any residue on the walls of the beaker by manipulation of the solution with a glass rod. Add 10 drops of hydrogen peroxide (30%) to the covered beaker and digest on a steam bath until reaction stops, then add an additional 10 drops of hydrogen peroxide.[9] When reaction has ceased, wash the cover glass and beaker wall, and evaporate the solution to dryness. Add 10 ml of diluted hydrochloric acid (1+1), warm to dissolve salts, and again evaporate to dryness. Repeat the addition of diluted hydrochloric acid and evaporation to dryness four times.

Add 10 ml of diluted hydrochloric acid (1+1) to the residue, cover the beaker, and warm until the solution clears. Cool, add 10 ml of hydrochloric acid, and mix well with a stirring rod.[10] The solution is now ready for passage through the anion-exchange column.

### 3.2. Ion-Exchange Separation of Nickel and Manganese, Cobalt, and Iron

Transfer 50 ml of diluted hydrochloric acid (3+1) to the column in small increments (5 to 10 ml), and drain the acid to about 1 cm above the top mat. Place a small funnel in the top of the column. Transfer the concentrated solution of the sample in small increments (5 ml) to the column with the bottom stopcock open. Add the sample as the solution moves down the column until all the sample has been transferred to the column. Always keep the resin completely covered with solution to prevent the formation of air pockets. Replace the "waste" beaker under the column with a clean 600-ml beaker. Wash the beaker that contained the sample with 5-ml portions of diluted hydrochloric acid (3+1), policing the walls with a glass rod, and transfer the washings to the funnel and column until 10 washings have been made. The important point is to get all of the sample solution onto the resin bed. Finally, wash the funnel and the walls of the column above the resin with several small portions of the diluted hydrochloric acid (3+1); a dropping tube and bulb is useful at this point.

Place the cap on the column top, lubricating the joint with a drop or two of water to prevent air leakage, and clamp. Adjust the stopcocks to deliver the diluted hydrochloric acid (3+1) from the reservoir bottle to the column, and adjust the bottom stopcock on the column to a flow rate of 100 to 125 ml/hr. Collect 425 ml of solution, then adjust the stopcocks to deliver diluted hydrochloric acid (1+2) to the column. After 15 min the more dilute acid will be about half way down the column, the beaker containing the nickel and manganese, along with chromium and some other elements, is then replaced with a clean 600-ml beaker. Place the beaker containing the nickel and manganese on a steam bath and evaporate to dryness.

Continue the flow of diluted hydrochloric acid (1+2) at a rate of 100 to 125 ml/hr [11] until 425 ml of the cobalt fraction is obtained, then change the stopcocks to deliver diluted hydrochloric acid (1+11). Replace the beaker containing the cobalt with a clean 600-ml beaker and follow the procedure outlined in the previous paragraph. Place the beaker containing the cobalt on a steam bath, and evaporate the solution to dryness.

Continue the flow of diluted hydrochloric acid (1+11), at a rate of 100 to 125 ml/hr, until 450 ml of the iron fraction is obtained. Close the stopcocks, transfer the beaker to a steam bath, and evaporate the solution to dryness.

### 3.3. Determination of Nickel, Manganese, Cobalt, and Iron

#### a. Nickel

#### Reagents

*Citric acid solution (250 g/liter).* Dissolve 250 g of citric acid in 600 to 800 ml of water, add 20 ml of diluted sulfuric acid (1+1), and dilute to 1,000 ml with water. Filter, if necessary.

*Dimethylglyoxime solution (10 g/liter of ethanol).* Dissolve 10 g of dimethylglyoxime in 1 liter of ethanol, and filter.

#### Procedure

Add 10 ml of diluted hydrochloric acid (1+1) to the reserved beaker containing the first fraction from the ion-exchange column, and warm to dissolve the residue. Dilute to 25 ml with warm water, transfer to a 200-ml volumetric flask, policing the beaker well. Cool to room temperature, dilute to the mark, and mix well. Transfer a 50-ml aliquot to a 400-ml beaker, and reserve the remainder of the solution in the volumetric flask for the determination of manganese.

Add 5 ml of hydrochloric acid and 25 ml of citric acid solution to the aliquot in the beaker. Dilute to 100 ml with warm water, and neutralize with ammonium hydroxide, using litmus paper as an indicator. Filter the solution [12] through a 9-cm close-textured paper containing a little pulp into a 600-ml beaker and wash well with hot water.

Adjust the filtrate to a volume of 300 ml and add an excess of 2 to 3 ml of ammonium hydroxide. Add 0.4 ml of dimethylglyoxime solution for each milligram of nickel (in the aliquot) and then 5 ml in excess. Digest for 30 min on a steam bath with occasional stirring, and cool to room temperature. Filter through a weighed 30-ml fritted-glass crucible of medium or fine porosity. Transfer the precipitate to the crucible and finally wash 4 or 5 times with cold water. Dry the precipitate to constant weight at

[9] This treatment is to remove any residual sulfide by oxidation. It also serves to oxidize any iron to the trivalent form required for the ion-exchange separation.

[10] This treatment adjusts the solution to approximately 9 *N* hydrochloric acid, which is the correct acidity for the first step of the ion-exchange separation.

[11] The lower viscosity of the more dilute acid usually requires a readjustment of the stopcock at the bottom of the column to maintain the specified flow.

[12] The solution is usually cloudy with resin dissolved in the strong hydrochloric acid used for elution. The paper can be ignited, treated with $H_2SO_4$-HF to eliminate silica, and the residue dissolved in a few drops of HCl and returned to the main solution.

150° C. Cool in a desiccator and weigh as nickel dimethylglyoxime.

b. Manganese

REAGENTS

*Sodium hydroxide solution (300 g/liter).* Transfer 30 g of NaOH to a 250-ml beaker, dissolve in 50 ml of water, and dilute to 100 ml.

*Sodium bromate.*

*Mixed-acid solution.* Add 100 ml of sulfuric acid to 675 ml of water slowly with good stirring. Cool, and add 125 ml of phosphoric acid (85%) and 100 ml of nitric acid.

*Standard sodium arsenite solution (1 ml=0.4 mg of* Mn). Transfer 4.8 g of $As_2O_3$ to a 600-ml beaker, add 50 ml of water and 6 g of NaOH. Stir until the oxide has dissolved, dilute to 300 ml with water, and bubble a stream of carbon dioxide into the solution until it is saturated with $CO_2$. Dilute with water to 4 liters in a glass-stoppered bottle, and mix well. The solution is standardized by titration of known amounts of manganese oxidized with persulfate.

*Silver nitrate solution (8 g per liter).*

*Ammonium persulfate solution (250 g per liter).* This solution is not stable, and should be prepared as needed.

PROCEDURE

Transfer a 100-ml aliquot of the solution reserved from the nickel determination to a 400-ml beaker, and dilute to a volume of about 225 ml with warm water. Add the sodium hydroxide solution dropwise until the solution is faintly acid, as judged by the redissolving of the precipitate. Add 3 g of sodium bromate and slowly bring to boiling temperature to oxidize the chromium. Remove from the heat, make just alkaline with the sodium hydroxide solution, and then add 10 ml in excess. Boil gently a minute or two, and allow the precipitate containing the manganese to settle on a steam bath for a few minutes. Filter the hot solution through an 11-cm loose-textured paper containing a little paper pulp and wash 2 or 3 times with a little hot water. Return the paper and precipitate to the beaker,[13] add 10 ml of nitric acid, and macerate the paper with a glass rod. Warm on a steam bath for a few minutes until the filter is disintegrated, and add 10 ml of water containing a few drops of sulfurous acid. Digest until the precipitate dissolves, dilute with 50 ml of hot water, and boil gently a minute or two. Allow to settle, filter [14] through a 9-cm loose-textured paper, and wash well with hot diluted nitric acid (5+95). Evaporate the filtrate to dryness.

Add 30 ml of acid mixture to the dry residue and digest until complete solution is obtained. Add 100 ml of hot water, 10 ml of silver nitrate solution, and 10 ml of ammonium persulfate solution. Bring to a boil, and boil briskly for 60 to 90 sec. Cool to a temperature of 15° C or lower, add 75 ml of cold water with stirring, and titrate potentiometrically with the standard sodium arsenite solution to the first permanent break.

c. Cobalt

PROCEDURE

Add 20 ml of diluted nitric acid (1+1) to the cobalt residue obtained from the second fraction of the ion-exchange separation. Cover the beaker and digest on a steam bath until the salts are in solution. Add 3 ml of perchloric acid, and dissolve any residue on the walls of the beaker by manipulation of the solution with the glass rod. Transfer the beaker to a hot plate and evaporate to fumes of perchloric acid. Cool, add 5 ml of nitric acid, police the walls of the beaker, and again evaporate the solution to fumes of perchloric acid. Repeat the procedure twice more to destroy the resin.[15] Continue the heating to volatilize most of the perchloric acid, and to convert most of the salt to black oxide.

Cool, add 10 ml of diluted hydrochloric acid (1+1), and warm to dissolve the oxide. Add 10 ml of hot water, and digest until the oxide is in solution. Remove and wash the cover glass, and evaporate the solution to dryness. Repeat the addition of 10 ml of diluted hydrochloric acid (1+1) and evaporation to dryness twice to insure decomposition of nitrates.[16]

Add 30 ml of diluted hydrochloric acid (1+1) to the dried residue and warm to dissolve the salts. Transfer the solution to a 400-ml beaker, washing well with hot water. Adjust the volume to about 150 ml and cool. Neutralize the solution by the dropwise addition of ammonium hydroxide.[17] Add 1 g of hydroxylamine hydrochloride and stir well for a minute or two while the salt is dissolving. Add 5 ml of ammonium hydroxide in excess, and dilute to approximately 275 ml with water.

Transfer the solution to an electrolysis apparatus, cover with a split watchglass, and electrolyze overnight with platinum-gauze electrodes, using a current density of 0.4 amp/dm$^2$. In the morning, wash the underside of the cover glass, and continue the electrolysis for 30 min. Without interrupting the current, slowly lower the beaker, and at the same time, wash the electrodes with a stream of water.[18] Immediately immerse the electrodes several times in a beaker of water. Interrupt the current and remove the cathode. Rinse the cathode with ethyl alcohol, shake off the excess alcohol, and dry at 110° C in an an oven for a few minutes. Cool in a desiccator, and weigh the deposit as metallic cobalt.

[13] Alternatively, the paper can be decomposed by fuming with the mixed acid solution and several additions of $HNO_3$ to destroy the paper. The final nitric acid concentration during the development of the permanganate color is critical, and the solution should contain no more than 3 ml of $HNO_3$.

[14] The paper can be ignited, treated with $H_2SO_4$-HF, and any residue can be dissolved in a few drops of $HNO_3$ and added to the main solution.

[15] Anion-exchange resins usually contain quaternary amine cations and may contaminate a cathode deposit in the electrolysis that follows.

[16] Nitrates inhibit or completely prevent the deposition of cobalt.

[17] A small strip of Hydrion paper will conveniently indicate approximate neutrality.

[18] The electrolyte usually contains from 0.2 to 1 mg of Co. A suitable aliquot can be heated with nitric acid to destroy ammonium salts, and the cobalt determined by the nitroso-R photometric method.

d. Iron

### Reagents

*Potassium-permanganate solution (25 g/liter).*

*Stannous chloride solution (150 g/liter of diluted hydrochloric acid (1+3)).* Dissolve 150 g of $SnCl_2 \cdot 2H_2O$ in 500 ml of diluted hydrochloric acid (1+1), warming if necessary. Cool and dilute to 1 liter with water.

*Mercuric chloride solution (approximately 60 g/liter).* Prepare a saturated solution of $HgCl_2$ in water.

*Sulfuric-phosphoric acid solution.* Mix 150 ml of sulfuric acid with 300 ml of water, cool, add 150 ml of phosphoric acid (85%), and dilute to 1 liter with water.

*Sodium diphenylamine sulfonate indicator solution (0.01M).* Transfer 0.32 g of barium diphenylamine sulfonate and 0.5 g of $Na_2SO_4$ to a 250-ml Erlenmeyer flask, add 100 ml of water, and mix well. Decant the supernatant liquid from the precipitated $BaSO_4$.

*Standard potassium dichromate solution (0.1N).* Transfer 4.904 g of $K_2Cr_2O_7$ (National Bureau of Standards Standard Sample 136) to a 1-liter volumetric flask, dissolve in a little water, dilute to the mark, and mix well.

### Procedure

Add 10 ml of diluted hydrochloric acid (1+1) to the beaker containing the dried residue from the third fraction containing the iron. Cover the beaker, and warm until a clear solution is obtained. Dilute to about 25 ml with hot water and add five drops of $KMnO_4$ solution and stir. Heat to boiling, and boil gently for a few minutes to expel free chlorine. Add stannous chloride solution dropwise and with good stirring, until the color of the ferric chloride is discharged, and then 1 or 2 drops (no more) in excess. Wash down the inside of the beaker and cover glass, and quickly cool in ice water. Add, at one stroke, 10 ml of saturated mercuric chloride solution, stir well, and again wash down the inside of the beaker with cool water. Allow the solution to stand for 2 to 5 min.

Dilute to 200 ml with cold water, add 20 ml of sulfuric-phosphoric acid mixture and 4 drops of indicator solution. Titrate the reduced iron with a standard potassium dichromate solution to a clear blue or blue-green end point, which should be permanent for 30 sec.

## 4. Results and Discussion

The results obtained on a series of synthetic solutions made to simulate some of the cobalt- and nickel-base alloys of interest are given in table 1. Nickel and iron were added as weighed portions of the high-purity metals, manganese was added as aliquots of a manganous nitrate solution prepared from high-purity manganese metal, and cobalt was added as aliquots of a cobalt chloride solution standardized by electrolysis.

The nickel and manganese values require little comment, recoveries being within the limits usually obtained in conventional methods of analysis.

The cobalt recoveries are based on a solution standardized by electrolysis and on a determination finished by electrolysis, and demonstrate the completeness of the recovery in the analytical procedure. They do not, however, indicate the accuracy of the electrolytic procedure for the determination of cobalt. To learn something of the accuracy of the electrolytic deposition method for the determination of cobalt, a batch of approximately 250 g of $Co(NH_3)_6Cl_3$ was prepared [4] from reagent grade $CoCl_2 \cdot 6H_2O$.

The salt was purified by precipitating three times from diluted hydrochloric acid (1+10), finally recrystallizing from water, and drying in a vacuum desiccator over magnesium perchlorate and soda-asbestos. Weighed portions of 3 to 5 g were assayed by reduction to metal under hydrogen in a Rose-type crucible constructed of Vycor. The average of five determinations, involving 21 g of the salt, was 22.041 percent of cobalt, compared to a calculated value of 22.046 percent of cobalt, based on the weight in air of the salt. The salt was apparently quite uniform, the individual values all being within one part in a thousand of the average. The purification process was also effective in reducing the nickel content of the original cobalt salt from 0.08 percent to approximately 0.001 percent of nickel.

Portions of the salt were converted to cobalt sulfate by solution in 20 ml of water and 20 ml of diluted sulfuric acid (1+1) and evaporation to fumes. Cobalt was deposited electrolytically from an ammoniacal ammonium sulfate-sulfite electrolyte, as usually recommended [5]. The values obtained are given in table 2, along with similar data obtained by plating the salt in ammoniacal ammonium chloride solution containing hydroxylamine hydrochloride under the conditions of the recommended procedure. The deposits from the sulfate-sulfite electrolytes are corrected for deposited sulfide sulfur, and all deposits are corrected for the cobalt remaining in the electrolyte. The latter correction was made in a suitable aliquot of the electrolyte by the Nitroso-R-photometric method. The electrolyte contained an average of 0.8 mg of cobalt with a plating current of 0.25 amp/dm$^2$, and an average of 0.6 mg of cobalt with 0.4 amp/dm$^2$.

The data demonstrate that the electrolytic method for cobalt gives high values similar to those obtained for nickel [6] and that the values obtained by deposition from the chloride solutions are the more nearly correct. The data are typical of approximately 100 determinations [11] made under both conditions from aliquots of several cobalt chloride solutions. The deposition from chloride solution eliminates the necessity for making a sulfur correction.

The recovery of iron is not entirely satisfactory as shown in table 1, the values tending to run 5 or 6 parts in a thousand low. Experiments to determine where the iron was lost in the procedure showed approximately one part in a thousand to be in the

TABLE 1. *Results obtained for nickel, manganese, cobalt, and iron by the recommended procedure on synthetic mixtures*

| Experiment number | Nickel | | | Manganese | | | Cobalt | | | Iron | | |
|---|---|---|---|---|---|---|---|---|---|---|---|---|
| | Taken | Found | Difference | Taken | Found | Difference | Taken | Found | Difference | Taken | Found | Difference |
| | *g* | *g* | *g* | *mg* | *mg* | *mg* | *g* | *g* | *g* | *g* | *g* | *g* |
| 1 | 0.4000 | 0.3998 | −0.0002 | 10.0 | 10.01 | 0.01 | 0.4210 | 0.4212 | 0.0002 | 0.2005 | 0.1960 | −0.0045 |
| 2 | .4004 | .4000 | −.0004 | 10.0 | 10.02 | .02 | .4210 | .4215 | .0005 | .1004 | .0967 | −.0037 |
| 3 | .4002 | .4001 | −.0001 | 10.0 | 10.01 | .01 | .4210 | .4211 | .0001 | .0509 | .0504 | −.0005 |
| 4 | .0505 | .0503 | −.0002 | 10.0 | 9.99 | −.01 | .6311 | .6313 | .0002 | .3008 | .2961 | −.0047 |
| 5 | .0500 | .0499 | −.0001 | 10.0 | 9.99 | −.01 | .6311 | .6306 | −.0005 | .1004 | .0994 | −.0010 |
| 6 | .4003 | .4006 | .0003 | 10.0 | 10.01 | .01 | .4212 | .4219 | .0007 | .2005 | .1993 | −.0012 |
| 7 | .4004 | .4007 | .0003 | 10.0 | 10.02 | .02 | .4212 | .4222 | .0010 | .1005 | .1000 | −.0005 |
| 8 | .4004 | .4004 | .0000 | 10.0 | 10.02 | .02 | .4212 | .4219 | .0007 | .0503 | .0498 | −.0005 |
| 9 | .0506 | .0508 | .0002 | 10.0 | 9.95 | −.05 | .6314 | .6314 | .0000 | .3004 | .2993 | −.0011 |
| 10 | .0507 | .0508 | .0001 | 10.0 | 9.97 | −.03 | .6314 | .6311 | −.0003 | .1000 | .0994 | −.0006 |
| 11 | .4002 | .3998 | −.0004 | 10.0 | 10.04 | .04 | .4211 | .4216 | .0005 | .2000 | .1993 | −.0007 |
| 12 | .4004 | .4001 | −.0003 | 10.0 | 10.03 | .03 | .4211 | .4217 | .0006 | .1007 | .1002 | −.0005 |
| 13 | .4004 | .4000 | −.0004 | 10.0 | 10.03 | .03 | .4211 | .4215 | .0004 | .0504 | .0500 | −.0004 |
| 14 | .0503 | .0500 | .0000 | 10.0 | 10.03 | .03 | .6313 | .6311 | −.0002 | .3006 | .2995 | −.0011 |
| 15 | .0503 | .0504 | .0001 | 10.0 | 10.03 | .03 | .6313 | .6310 | −.0003 | .1004 | .0996 | −.0008 |

TABLE 2. *Results obtained for cobalt by the electrolysis of* $Co(NH_3)_6Cl_3$

| Taken | | Weight of deposit | Cobalt in electrolyte | Sulfur in deposit | Cobalt found | Difference | Remarks |
|---|---|---|---|---|---|---|---|
| $Co(NH_3)_6Cl_3$ | Cobalt | | | | | | |
| *g* | *g* | *g* | *g* | *g* | *g* | *g* | |
| 0.2500 | 0.0551 | 0.0555 | 0.0009 | 0.0003 | 0.0561 | 0.0010 | 0.25 amp/dm². Ammoniacal ammonium sulfate-sulfite electrolyte. |
| .2500 | .0551 | .564 | .0008 | .0002 | .0570 | .0019 | |
| 2.0000 | .4408 | .4426 | .0017 | .0014 | .4429 | .0021 | |
| 2.0000 | .4408 | .4438 | .0009 | .0015 | .4432 | .0024 | |
| 3.0000 | .6612 | .6647 | .0008 | .0022 | .6633 | .0021 | |
| 3.0000 | .6612 | .6641 | .0009 | .0018 | .6632 | .0020 | |
| 0.2500 | .0551 | .0555 | .0005 | .0003 | .0557 | .0006 | 0.4 amp/dm². Ammoniacal ammonium sulfate-sulfite electrolyte. |
| .2500 | .0551 | .0562 | .0006 | .0003 | .0565 | .0014 | |
| 2.0000 | .4408 | .4433 | .0008 | .0015 | .4426 | .0018 | |
| 2.0000 | .4408 | .4438 | .0007 | .0017 | .4428 | .0020 | |
| 3.0000 | .6612 | .6648 | .0007 | .0020 | .6635 | .0023 | |
| 3.0000 | .6612 | .6646 | .0006 | .0020 | .6632 | .0020 | |
| 0.2500 | .0551 | .0551 | .0006 | | .0557 | .0006 | 0.25 amp/dm². Ammoniacal ammonium chloride-hydroxylamine hydrochloride electrolyte. |
| .2500 | .0551 | .0556 | .0006 | | .0562 | .0011 | |
| 1.0000 | .2204 | .2206 | .0004 | | .2210 | .0006 | |
| 2.0000 | .4408 | .4415 | .0006 | | .4421 | .0013 | |
| 2.0000 | .4408 | .4409 | .0007 | | .4416 | .0008 | |
| 3.0000 | .6612 | .6613 | .0008 | | .6621 | .0009 | |
| 3.0000 | .6612 | .6614 | .0008 | | .6622 | .0010 | |
| 0.2500 | .0551 | .0554 | .0006 | | .0560 | .0009 | 0.4 amp/dm². Ammoniacal ammonium chloride-hydroxylamine hydrochloride electrolyte. |
| .2500 | .0551 | .0554 | .0004 | | .0558 | .0007 | |
| 1.0000 | .2204 | .2206 | .0005 | | .2211 | .0007 | |
| 2.0000 | .4408 | .4416 | .0007 | | .4423 | .0015 | |
| 2.0000 | .4408 | .4412 | .0006 | | .4418 | .0010 | |
| 3.0000 | .6612 | .6616 | .0006 | | .6622 | .0010 | |
| 3.0000 | .6612 | .6612 | .0009 | | .6621 | .0009 | |
| 0.2500 | [1] .0551 | .0552 | .0003 | | .0555 | .0004 | Plated, with stirring, at 1 amp/dm². Ammoniacal ammonium chloride-hydroxylamine hydrochloride electrolyte. |
| .2500 | [1] .0551 | .0556 | .0005 | | .0561 | .0010 | |
| 3.0000 | [2] .6612 | .6620 | .0003 | | .6623 | .0011 | |
| 3.0000 | [2] .6612 | .6616 | .0006 | | .6622 | .0010 | |

[1] 3-hr plating time. [2] 7-hr plating time.

TABLE 3. *Results obtained for nickel, manganese, cobalt, and iron by the recommended procedure on a synthetic mixture approximating a high-temperature alloy and on a high-temperature alloy*

| Sample number | Nickel | | | Manganese | | | Cobalt | | | Iron | | |
|---|---|---|---|---|---|---|---|---|---|---|---|---|
| | Taken | Found | Difference | Taken | Found | Difference | Taken | Found | Difference | Taken | Found | Difference |
| | *g* | *g* | *g* | *g* | *g* | *g* | *g* | *g* | *g* | *g* | *g* | *g* |
| 1 | 0.2071 | 0.2071 | 0.0000 | 0.0165 | 0.0165 | 0.0000 | 0.3970 | 0.3971 | 0.0001 | 0.0193 | 0.0193 | 0.0000 |
| 2 | .2070 | .2072 | .0002 | .0165 | .0165 | .0000 | .3970 | .3970 | .0000 | .0193 | .0192 | −.0001 |
| 3 | .2072 | .2073 | .0001 | .0165 | .0166 | .0001 | .3972 | .3977 | .0005 | .0193 | .0194 | .0001 |
| 4 | .2070 | .2071 | .0001 | .0165 | .0165 | .0000 | .3972 | .3980 | .0008 | .0193 | .0193 | .0000 |
| High-temperature alloy | | .2071 | | | .0164 | | | .4286 | | | .0214 | |
| | | .2070 | | | .0164 | | | .4286 | | | .0215 | |
| | | .2071 | | | .0164 | | | .4290 | | | .0213 | |
| | | .2069 | | | .0164 | | | .4292 | | | .0213 | |
| | | .2066 | | | .0163 | | | .4288 | | | .0214 | |
| | | .2067 | | | .0164 | | | .4291 | | | .0213 | |

cobalt fraction. This loss may possibly be due to a photoreduction [1] of the iron similar to that occurring in the ether-extraction of ferric chloride, because ferrous iron is eluted sufficiently rapidly in 4 *N* hydrochloric acid to be collected in the cobalt fraction. The remainder was retained by the resin and could be recovered by elution after allowing the resin to equilibrate a day with the 1 *N* hydrochloric acid.

This slightly low recovery of iron appears to be largely due to the unfavorable diffusion characteristics [14] in the resin column. Qualitative experiments, using commercially available resins of 1- to 10-percent divinylbenzene cross-linkage, indicate the diffusion rates to be more rapid at the 2-percent divinylbenzene level. However, these resins expand and contract so much in going through the analysis cycle that the operation of this type of column is not attractive. Further, a longer column is required, as the bands move much faster under comparable conditions of acidity. The use of colloidal aggregates of the higher cross-linkage resins may be the best answer for quantitative work with this particular type of resin, if the resins can be commercially prepared to allow reasonably rapid flow rates (25 ml or more per hour per square centimeter of cross section).

The results obtained in the analysis of an S–816 type alloy are given in table 3. The values for nickel, manganese, and iron on synthetic control solutions are satisfactory, and good replication of values on the sample is evident, the iron difficulties not being serious at the percentage level of iron in this sample. The cobalt values are subject to the errors of the electrolytic method and are probably 0.5 to 0.8 mg too high as recorded.

It may be mentioned that the ferricyanide titration procedure [2, 13] may prove somewhat more attractive for the rapid determination of cobalt, particularly if good cobalt standards become available. However, it should be kept in mind that manganese interferes quantitatively in this procedure, and that chromium is a disturbing element and must usually be removed if present in any appreciable percentage. Furthermore, the ferricyanide method is limited to approximately 100- to 125-mg quantities of cobalt if good end points are to be obtained.

## 5. References


[1] S. E. Q. Ashley and W. M. Murray, Jr., Ind. Eng. Chem., Anal. Ed. **10,** 367 (1938).
[2] B. Bagshaw and J. D. Hobson, Analyst **73,** 152 (1948).
[3] R. C. Chirnside, H. J. Cluley, and P. M. C. Proffitt, Analyst **72,** 351 (1947).
[4] W. Conrad Fernelius, Editor, Inorganic syntheses, vol. II, p. 217 (McGraw-Hill Book Co., Inc., New York, N. Y., 1946).
[5] W. H. Hillebrand, G. E. F. Lundell, H. A. Bright, and J. I. Hoffman, Applied inorganic analysis, 2d ed., p. 413 (J. Wiley & Sons, Inc., New York, N. Y., 1953).
[6] W. H. Hillebrand, G. E. F. Lundell, H. A. Bright, and J. I. Hoffman, Applied inorganic analysis, 2d ed., p. 413, footnote 26, (J. Wiley & Sons, Inc., New York, N. Y., 1953).
[7] H. Kirtchik, Anal. Chem. **19,** 55 (1947).
[8] K. A. Kraus and G. E. Moore, J. Am. Chem. Soc. **75,** 1460 (1953).
[9] K. A. Kraus, F. Nelson, and J. F. Baxter, J. Am. Chem. Soc. **75,** 2768 (1953).
[10] K. A. Kraus, F. Nelson, and G. W. Smith, J. Phys. Chem. **58,** 11 (1954).
[11] E. E. Maczkowske and J. L. Hague (unpublished data).
[12] G. E. Moore and K. A. Kraus, J. Am. Chem. Soc. **74,** 843 (1952).
[13] J. J. Phelan, Gen. Elec. Rev. **42,** 218 (1939).
[14] B. A. Soldano and G. E. Boyd, J. Am. Chem. Soc. **75,** 6101 (1953).



Washington, July 21, 1954.

Journal of Research of the National Bureau of Standards Vol. 53, No. 6, December 1954 Research Paper 2553

# Thermal Degradation of Polymers as a Function of Molecular Structure[1]

S. L. Madorsky and S. Straus

When heated in a vacuum at temperatures of about 200° to 500° C, polymer chains break up into volatile fragments of various sizes, depending on the nature of the polymer. Some polymers, like poly-alpha-methylstyrene, yield the monomer exclusively. Other polymers, like polymethylene, yield a whole spectrum of fragments consisting of 2 carbon atoms in the chain to about 50 or more. Intermediate between these two types of polymers are those like polyisobutylene, which yield partly monomer and partly large fragments. The rates at which these fragments are formed and vaporized also vary for different polymers. On comparing rates of volatilization of a series of polymers at 350° C, we find that polytetrafluoroethylene is the most thermally stable polymer, having an initial rate of volatilization of 0.0000016 weight percent per minute, whereas poly-alpha-methylstyrene is the least stable, having a rate of volatilization of 230 percent per minute. These differences in the thermal behavior of polymers can be correlated with the molecular structure of the polymer chains and with the nature and frequency of side groups.

## 1. Introduction

When heated in a vacuum at temperatures of about 200° to 500° C, organic polymers usually degrade to yield molecular fragments of various sizes. Some polymers, like poly-alpha-methylstyrene and polymethyl methacrylate, yield almost exclusively the monomer, whereas other polymers, such as polymethylene, yield a whole spectrum of molecular fragments volatilizable at the temperatures employed. Intermediate between these two extremes are polymers like polyisobutylene that yield part monomer and part larger fragments. The rates of degradation are also different for different polymers. In the case of some polymers, degradation by heat, as expressed by loss of weight through volatilization, is almost complete in less than an hour at about 300° C, whereas in the case of others there is very little loss of weight during the same period, even at 450° C. The difference in the thermal behavior of polymers has been the subject of a number of papers by various authors in the last few years [1 to 12].[2]

In this investigation a systematic study was initiated to determine the effect of molecular structure of chains and side groups of polymers on the rate of their degradation and the nature and relative amounts of the volatile products obtained when these polymers are heated in a vacuum. The following polymers were used:

1. A pure grade of polymethylene,

of high molecular weight prepared by the decomposition of diazomethane, using trimethyl borate as catalyst. This material is the same as was used in the study of melting transition of polymethylene [13]. Unlike polyethylene, this polymer consists of a nonbranched hydrocarbon chain.

2. Polyisobutylene,

of high purity was obtained by repeatedly dissolving the commercial polymer in benzene and precipitating with methanol. It had a molecular weight of 1,500,000, as determined by light-scattering.

3. Polypropylene,[3]

A 90-g sample of number-average molecular weight of about 5,000 was reduced to 6 g of a higher molecular weight material by six fractionation steps. In each step the material was dissolved in benzene and then precipitated with acetone.

4. A pure grade of polybenzyl,[4]

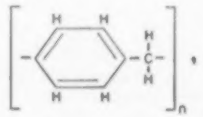

[1] This work was performed as a part of the research project sponsored by the Federal Facilities Corporation, Office of Synthetic Rubber Research and Development Division, Polymer Science Branch.

[2] Figures in brackets indicate the literature references at the end of this paper.

[3] The authors are indebted to C. M. Fontana, Socony Vacuum Co., for supplying this polymer.

[4] The authors are indebted to Daniel I. Livingston, Polaroid Corporation, for this polymer.

of molecular weight of 4,300 ±10 percent, as determined cryoscopically.

5a. Poly-beta-deuterostyrene,

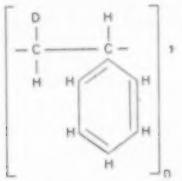

molecular weight 220,000 by light-scattering. The same material was used by Wall, Brown, and Hart [14] in their studies on pyrolysis of alpha- and beta-deuterostyrene polymers. The monomer used in the preparation of this polymer contained about 15 percent of normal styrene.

5b. Poly-beta-deuterostyrene of much higher molecular weight than 5a. The monomer used in its preparation contained only a few percent of normal styrene.

## 2. Apparatus and Experimental Procedure

The work described in this paper was carried out in two parts: (1) pyrolysis of polymer samples and fractionation of the volatile products, and (2) a study of rates of thermal degradation and the activation energies involved.

### 2.1. Pyrolysis

Pyrolysis experiments were carried out on polymethylene, polypropylene, polybenzyl, and poly-beta-deuterostyrene. Pyrolysis of polyisobutylene has been studied and described [5]. The apparatus consisted of a Dewar-like molecular still provided with a platinum tray resting on a platinum-wire-wound heater placed inside. This apparatus and the experimental procedure have been described [1, 5, 6]. Only a few salient points of the procedure will be recounted here. The samples were limited to a maximum of about 40 mg to avoid spattering that might occur if larger amounts were used. Polymethylene and polybenzyl were used in powdered form, polypropylene and poly-beta-deuterostyrene as solutions in benzene. In either case the samples were preheated in a vacuum for about 1½ hr at 160° C, and the volatiles were rejected before starting pyrolysis. In all experiments it took 45 min to heat the tray containing the sample to the pyrolysis temperature. This temperature was then maintained constant to about ±1.5 deg C for 30 min. The following fractions were obtained: A residue, I, except when pyrolysis was carried to completion; a heavy fraction, II, volatile at the temperature of pyrolysis; a light fraction, III, volatile at room temperature. In some cases fraction III was separated by molecular distillation at −80° C into a more volatile fraction, IIIA, and a less volatile fraction, IIIB. A gaseous fraction, IV, not condensable at liquid-nitrogen temperature, was also collected. The weights of all these fractions were determined directly or indirectly. Fraction II was tested for average molecular weight by a microcryoscopic method in a suitable solvent. Fractions III, IIIA, and IIIB were analyzed in the mass spectrometer. Fraction IV amounted in all cases to less than 0.1 percent by weight of the sample, and was found on mass-spectrometer analysis to consist of a small amount of hydrogen mixed with air, carbon dioxide, and carbon monoxide.

### 2.2. Rates

Rates of degradation, as expressed by loss in weight of polymer samples when heated in a vacuum, were determined by means of a very sensitive tungsten helical-spring balance. The method and the apparatus used in this part of the work have also been described [7, 8, 9]. Samples were limited to 5 to 6 mg and were used in dry state, after preheating for several hours in a vacuum of about 100 mm at 175° C to a constant weight, in order to eliminate traces of solvents.

## 3. Results

### 3.1. Pyrolysis

Results of pyrolysis experiments at various temperatures are shown in table 1. Fractions I, II, and III add up to 100-percent material balance because the gaseous fraction, IV, is very small. Polymethylene, like polyethylene, yields mostly fraction II. Polypropylene and polybenzyl yield more of fraction III and less of fraction II than polymethylene. Low and high molecular weight poly-beta-deuterosytrene (5a and 5b) yield a fraction III equal to 42.2 and 41.0 percent, respectively, of the total volatilized part, about the same as in the case of polystyrene.

Mass-spectrometer analyses of fraction III or IIIA are shown in tables 2, 3, 4, 5, and 6. In the case of polymethylene, fraction III was separated into IIIA, comprising 20 percent, and IIIB, 80 percent, of its total weight. This was done in order to facilitate mass-spectrometer analysis. As seen from table 2, the components of IIIA consist of saturated and unsaturated hydrocarbons up to and including six carbon atoms. Fraction IIIB was also analyzed in the mass spectrometer and was found to contain similarly saturated and unsaturated hydrocarbons, but of 7 to 12 carbon atoms.

On comparing table 2 with table 14 of reference [5],[5] which shows the mass-spectrometer analysis of fraction IIIA from polyethylene pyrolysis, we find that in the case of polymethylene this fraction has about twice as many double bonds as the corresponding fraction from polyethylene.

Polypropylene, like polymethylene, yields a large number of constituents in fraction III, and this fraction was therefore separated into subfractions IIIA and IIIB in the weight-percent ratio of 25:75.

[5] In this reference the ratio of IIIA to IIIB fraction for polyethylene is not shown. This ratio is the same (20:80) as for polymethylene.

Mass-spectrometer analysis of IIIA is shown in table 3 for three experiments. There is some disagreement in the analysis of this fraction from the three experiments, much more so than in the case of polymethylene reported in table 2. This difference does not seem to be due to a temperature effect. It is most likely due to experimental error

TABLE 1. *Pyrolytic factionation of polymers*

| Experiment | Temperature | Fractions of original sample | | | Fraction III of total volatilized part |
|---|---|---|---|---|---|
| | | I. Residue | II. Non-volatile at room temperature | III. Volatile at room temperature | |
| **Polymethylene** [a] | | | | | |
| | °C | wt % | wt % | wt % | wt % |
| 1 | 393 | 92.8 | 6.9 | 0.3 | 4.1 |
| 2 | 407 | 71.5 | 27.6 | .9 | 3.3 |
| 3 | 410 | 70.8 | 28.0 | 1.2 | 4.1 |
| 4 | 415 | 52.5 | ---- | --- | --- |
| 5 | 419 | 29.7 | 69.2 | 1.1 | 2.4 |
| 6 | 425 | 23.0 | 75.2 | 1.8 | 2.3 |
| 7 | 444 | 1.5 | 96.2 | 2.3 | 2.4 |
| 8 | 449 | 2.9 | 93.4 | 3.7 | 3.9 |
| | | | | Average | 3.2±0.7 |
| **Polypropylene** | | | | | |
| 1 | 328 | 91.8 | 6.7 | 1.5 | 17.7 |
| 2 | 374 | 71.4 | 24.4 | 4.2 | 14.8 |
| 3 | 380 | 58.5 | 35.7 | 5.8 | 14.0 |
| 4 | 384 | 53.9 | 39.4 | 6.7 | 14.5 |
| 5 | 393 | 36.8 | 54.3 | 8.9 | 14.0 |
| 6 | 395 | 39.2 | 62.8 | 8.0 | 11.3 |
| 7 | 400 | 13.2 | 76.9 | 9.9 | 11.5 |
| 8 | 410 | 3.6 | 85.3 | 11.1 | 11.6 |
| | | | | Average | 13.7±1.7 |
| **Polybenzyl** | | | | | |
| 1 | 412 | 81.5 | 16.9 | 1.6 | 8.9 |
| 2 | 427 | 74.4 | 23.3 | 2.3 | 9.0 |
| 3 | 431 | 48.2 | ---- | --- | --- |
| 4 | 444 | 28.1 | 67.5 | 4.4 | 6.2 |
| 5 | 462 | 5.6 | 89.1 | 5.3 | 5.6 |
| | | | | Average | 7.4±1.5 |
| **Poly-beta-deuterostyrene of low molecular weight (5a)** | | | | | |
| 1 | 314 | 87.3 | 7.8 | 4.9 | 38.6 |
| 2 | 334 | 77.0 | 13.7 | 9.3 | 40.3 |
| 3 | 341 | 69.0 | 19.7 | 11.3 | 36.5 |
| 4 | 355 | 40.8 | 33.9 | 25.3 | 42.6 |
| 5 | 361 | 36.2 | 36.7 | 27.1 | 42.4 |
| 6 | 366 | 21.2 | 44.2 | 34.6 | 43.8 |
| 7 | 371 | 18.8 | 46.0 | 35.2 | 43.3 |
| 8 | 374 | 8.8 | 51.9 | 39.3 | 43.0 |
| 9 | 374 | 7.8 | 50.5 | 41.7 | 45.1 |
| 10 | 399 | 1.0 | 52.7 | 46.3 | 46.6 |
| | | | | Average | 42.2±2.3 |
| **Poly-beta-deuterostyrene of high molecular weight (5b)** | | | | | |
| 1 | 345 | 98.8 | (b) | (b) | (b) |
| 2 | 360 | 86.6 | 8.0 | 5.4 | 40.0 |
| 3 | 376 | 28.9 | 40.8 | 30.3 | 42.6 |
| 4 | 384 | 6.6 | 55.8 | 37.6 | 40.3 |
| | | | | Average | 41.0±0.6 |

[a] The thermal-stability curve for polymethylene in figure 2 of reference [9] should have been drawn at 10 deg C above its present position.
[b] Amount of volatiles is too small for accurate weighing.

TABLE 2. *Mass-spectrometer analysis of fraction IIIA collected at −80° C in the pyrolysis of polymethylene*

| Component | Temperature of pyrolysis, ° C | | | | Average |
|---|---|---|---|---|---|
| | 398 | 410 | 416 | 435 | |
| | Mole % | Mole % | Mole % | Mole % | Mole % |
| Ethylene | 18.3 | 2.6 | 21.0 | 7.3 | 12.3 |
| Ethane | 8.1 | ------ | 9.1 | ------ | 4.3 |
| Propadiene | 1.6 | 1.1 | 1.3 | 1.5 | 1.4 |
| Propylene | 19.2 | 22.8 | 19.0 | 21.9 | 20.7 |
| Propane | ------ | 2.9 | ------ | 11.4 | 3.6 |
| Butadiene | 2.6 | .6 | ------ | 5.4 | 2.1 |
| Butene | 13.8 | 15.5 | 7.3 | 15.5 | 13.0 |
| Butane | 9.5 | 11.4 | 9.6 | 14.4 | 11.2 |
| Pentadiene | 2.7 | 3.3 | 2.3 | 2.7 | 2.8 |
| Pentene | 8.5 | 11.4 | 8.0 | 10.6 | 9.6 |
| Pentane | 5.7 | 7.4 | 5.7 | 5.6 | 6.1 |
| Hexadiene | 1.4 | 4.7 | 4.1 | ------ | 2.6 |
| Hexene | 7.7 | 15.9 | 11.3 | ------ | 8.7 |
| Hexane | .9 | .4 | 1.3 | 3.7 | 1.6 |
| Total | 100.0 | 100.0 | 100.0 | 100.0 | 100.0 |

TABLE 3. *Mass-spectrometer analysis of fraction IIIA collected at −80° C in the pyrolysis of polypropylene*

| Component | Temperature of pyrolysis, ° C | | | Average |
|---|---|---|---|---|
| | 390 | 395 | 410 | |
| | Mole % | Mole % | Mole % | Mole % |
| Acetylene | ------ | ------ | 1.0 | 0.3 |
| Ethylene | 5.4 | 6.1 | 1.0 | 4.1 |
| Ethane | 3.4 | 1.9 | ------ | 1.8 |
| Propadiene | ------ | 1.4 | .7 | .7 |
| Propylene | 11.0 | 2.7 | 7.1 | 6.9 |
| Butadiene | .9 | 1.1 | .5 | .8 |
| Butene | 22.7 | 9.2 | 18.5 | 16.8 |
| Butane | 13.1 | 12.7 | 12.7 | 12.8 |
| Isoprene | ------ | ------ | .8 | .3 |
| Pentadiene | .7 | .8 | 2.4 | 1.3 |
| Pentene | 20.3 | 25.1 | 13.6 | 19.7 |
| Pentane | 2.1 | 18.9 | 12.5 | 11.2 |
| Hexadiene | 3.7 | 2.8 | .3 | 2.3 |
| Hexene | 4.8 | 9.5 | 18.8 | 11.0 |
| Hexane | 7.7 | 7.2 | 6.0 | 7.0 |
| Benzene | 4.2 | .6 | 4.1 | 3.0 |
| Total | 100.0 | 100.0 | 100.0 | 100.0 |

TABLE 4. *Mass-spectrometer analysis of fraction III obtained in the pyrolysis of polybenzyl*

| Component | Temperature of pyrolysis, ° C | | | Average |
|---|---|---|---|---|
| | 412 | 431 | 444 | |
| | Mole % | Mole % | Mole % | Mole % |
| Toluene | 78.6 | 77.6 | 69.5 | 75.3 |
| Benzene | 20.3 | 21.3 | 29.6 | 23.7 |
| Xylene | 1.1 | 1.1 | .9 | 1.0 |
| Total | 100.0 | 100.0 | 100.0 | 100.0 |

TABLE 5. *Mass-spectrometer analysis of fraction III obtained in the pyrolysis of poly-beta-deuterostyrene (5a)*

| Component | Temperature of pyrolysis, ° C | | | | | Average |
|---|---|---|---|---|---|---|
| | 314 | 334 | 355 | 361 | 399 | |
| | *Mole %* | *Mole %* | *Mole %* | *Mole %* | *Mole %* | *Mole %* |
| Beta-deuterostyrene | 85.3 | 82.8 | 81.8 | 80.0 | 80.8 | 82.1 |
| Styrene | 10.2 | 11.1 | 11.1 | 10.2 | 11.3 | 10.8 |
| Toluene | 4.5 | 6.1 | 7.1 | 9.8 | 7.9 | 7.1 |
| Total | 100.0 | 100.0 | 100.0 | 100.0 | 100.0 | 100.0 |

TABLE 6. *Mass-spectrometer analysis of fraction III obtained in the pyrolysis of poly-beta-deuterostyrene (5b)*

| Component | Temperature of pyrolysis,° C | | Average |
|---|---|---|---|
| | 376 | 384 | |
| | *Mole %* | *Mole %* | *Mole %* |
| Beta-deuterostyrene | 96.9 | 96.8 | 96.8 |
| Deuterotoluene | .2 | .4 | .3 |
| Toluene | 2.9 | 2.8 | 2.9 |
| Total | 100.0 | 100.0 | 100.0 |

when dealing with quantities of the order of 1 mg. For example, the total time taken to separate fraction III into two subfractions by molecular distillation was only 2 min. A slight difference in the time from one sample to another might cause a difference in the composition of fraction IIIA or IIIB. In some experiments, IIIB was also analyzed in the mass spectrometer and was found to consist of saturated and unsaturated hydrocarbons containing 6 to 12 carbon atoms.

In the case of polybenzyl, an attempt to separate fraction III into IIIA and IIIB showed that all the material appeared in IIIA. For this reason fraction III was analyzed as such. Mass-spectrometer analysis of this fraction is shown in table 4. The main constituents are toluene and benzene. If polybenzyl were to have the structure then it should

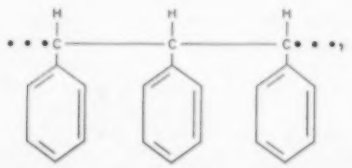

yield on pyrolysis stilbene as one of the volatile products. This compound was absent in fraction III. The vapor pressure of stilbene is given as 1 mm at 87.4° C for the *cis-* and at 113.2° C for the *trans-* variety [15]. After fraction III was separated by distillation at room temperature from the volatile products, another fraction was collected under conditions of molecular distillation at 80° C. This fraction, as shown by mass-spectrometer analysis, contained traces of toluene and benzene, but no stilbene. Another argument against the above structure is the high thermal stability of polybenzyl, as shown below. It is concluded, on the basis of these facts, that the chain structure of polybenzyl is

Haas, Livingston, and Saunders [16], on the basis of infrared, X-ray, chemical, and other evidence, suggest the following as a part of the structure of polybenzyl:

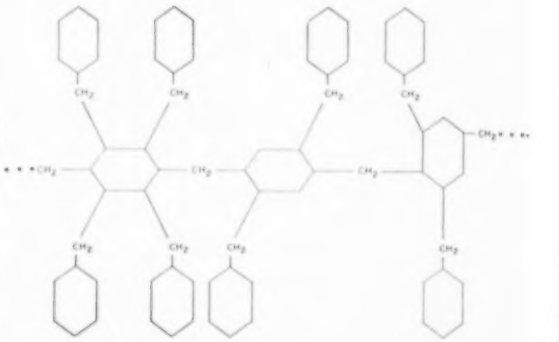

Poly-beta-deuterostyrene, like polystyrene, poly-alpha-deuterostyrene, and poly-meta-methylstyrene [5, 6], yields a fraction III not separable into IIIA and IIIB. Mass-spectrometer analysis of fraction III for polymers 5a and 5b is shown in tables 5 and 6. The appearance of normal styrene among the components shown in table 5 is due to its presence in the polymer.

Results of molecular weight determination of fraction II from pyrolysis of four polymers are shown in table 7. The values for polyethylene and polyisobutylene were given in a previous publication [5] and are shown here for comparison. Poly-beta-deuterostyrene yields a low-molecular-weight fraction II, and, as in the case of the other polystyrenes, this fraction consists most likely of the dimer, trimer, and tetramer. These compounds have molecular weights 210, 315, and 420, respectively, as compared with the average molecular weight of 318 for fraction II.

TABLE 7. *Average molecular weight of fraction II obtained in the pyrolysis of polymers*

| Polymer | Solvent | Average molecular weight |
|---|---|---|
| Polyethylene | Benzene | 692 |
| Polymethylene | Camphor | 755 |
| Polypropylene | Cyclohexane | 854 |
| Polyisobutylene | do | 543 |
| Polybenzyl | Benzene | 536 |
| Poly-beta-deuterostyrene (5b) | Cyclohexane | 318 |

### 3.2. Rates and Activation Energies of Thermal Degradation

In figures 1, 2, 3, and 4 the solid curves represent plots of percentage volatilization versus time at 4 to 5 different temperatures for polymethylene, polypropylene, polyisobutylene, and polybenzyl, respectively. All these curves show that at zero time, 1 to 3 percent (for polypropylene up to 7 percent) of the sample has already volatilized. This is due to the fact that it usually takes about 15 min to heat the crucible containing the sample from room temperature to the temperature of operation. During this time, depending on the temperature of operation, some of the material volatilized, and zero time indicated on the figures is the time the required temperature was reached. Logarithm to the base 10 of the percentage residue at any given time is shown plotted against time in the broken lines in the four figures. These lines are straight, except for a slight break in the early stage of vaporization of the samples. This break occurs anywhere between 0 and 100 min from the start of the experiment, and may be due to disturbances of operation in the early stage or to some mechanism of initiation of degradation different from that operating during subsequent degradation, or to both of these causes combined. The slope of the main part of each line, when multiplied by 2.303, represents the rate constant of volatilization of any of these polymers at the given temperature [17]. The initial rates are obtained by extrapolating the main parts of the broken lines in figures 1, 2, 3, and 4, to zero time, and are the same as the rate constants.

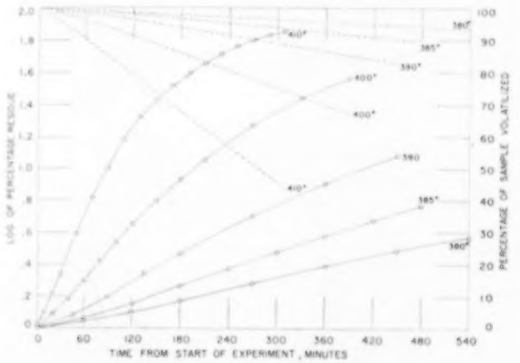


FIGURE 1. *Thermal degradation of polymethylene.*

———— Percentage of sample volatilized versus time; ..... logarithm to the base 10 of percentage residue versus time.

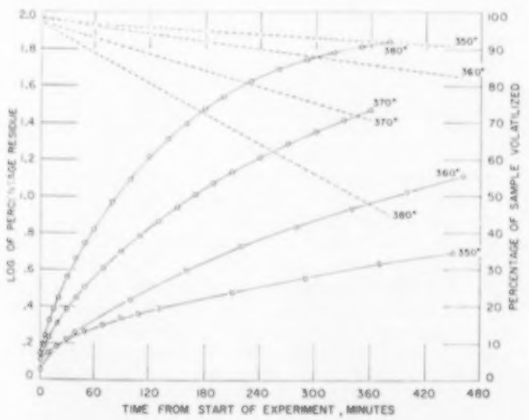


FIGURE 2. *Thermal degradation of polypropylene.*

———— Percentage of sample volatilized versus time; ..... logarithm to the base 10 of percentage residue versus time.

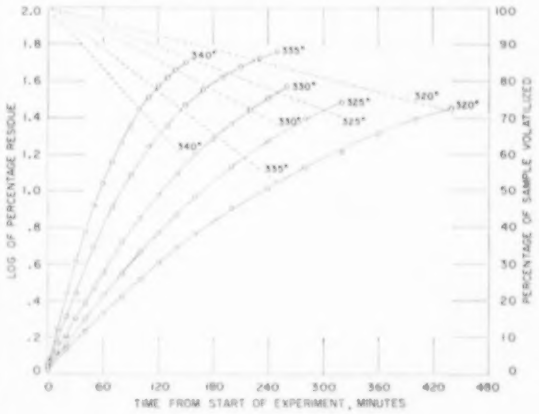


FIGURE 3. *Thermal degradation of polyisobutylene.*

———— Percentage of sample volatilized versus time; ..... logarithm to the base 10 of percentage residue versus time.

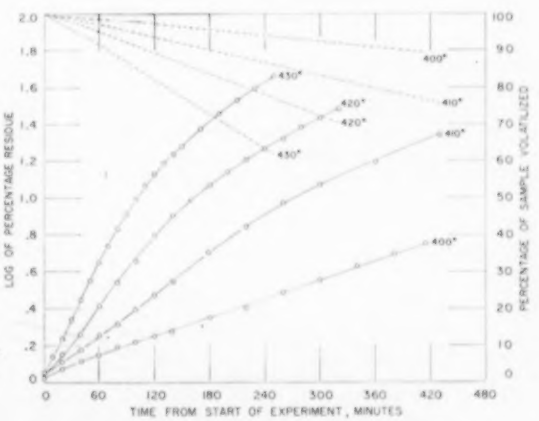


FIGURE 4. *Thermal degradation of polybenzyl.*

———— Percentage of sample volatilized versus time; ..... logarithm to the base 10 of percentage residue versus time.

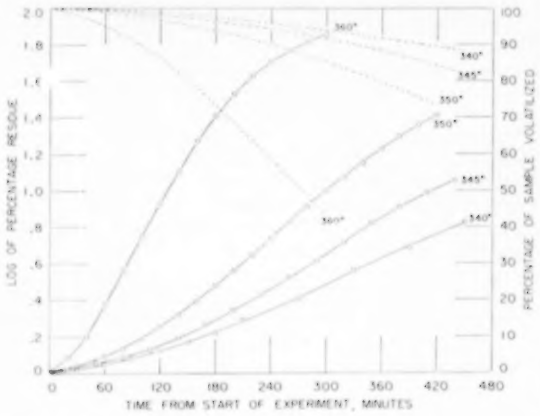


FIGURE 5. *Thermal degradation of poly-beta-deuterostyrene (5b).*

———, Percentage of sample volatilized versus time; - - - - - - - - - -, logarithm to the base 10 of percentage residue versus time.

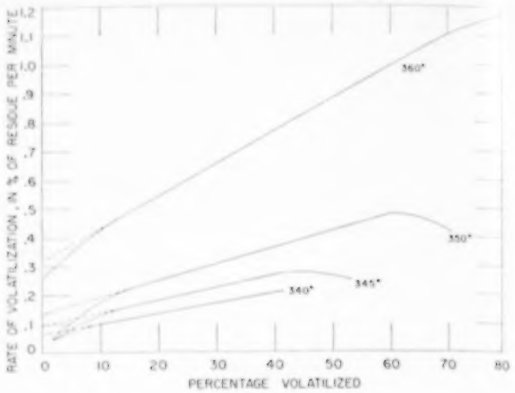


FIGURE 6. *Rate of volatilization of poly-beta-deuterostyrene (5b), in percent of residue per minute, as a function of percentage volatilization.*

———, Percentage of sample volatilized versus time; - - - - - - - - - -, logarithm to the base 10 of percentage residue versus time.

TABLE 8. *Experimental data on rates of thermal degradation of polymers*

| (1) | (2) | (3) | (4) | (5) | (6) | (7) |
|---|---|---|---|---|---|---|
| Polymer | Temperature | Duration of experiment | Total volatilized | Time after start of experiment when break in the logarithm of residue-versus-time curve occurs | Initial rate of volatilization | Activation energy |
| | °C | min | % | min | %/min | kcal |
| Polymethylene  | 380 | 540 | 28.4 | 20 | 0.063 | 76 |
| | 385 | 480 | 38.1 | 100 | .109 | |
| | 390 | 450 | 54.1 | 80 | .178 | |
| | 400 | 390 | 78.2 | 60 | .413 | |
| | 410 | 310 | 92.8 | 40 | .860 | |
| Polypropylene  | 350 | 450 | 34.9 | 80 | 0.069 | 61 |
| | 360 | 450 | 55.4 | 80 | .158 | |
| | 370 | 300 | 73.6 | 40 | .338 | |
| | 380 | 280 | 92.0 | 20 | .666 | |
| Polyisobutylene  | 320 | 440 | 72.6 | 0 | 0.268 | 52 |
| | 325 | 320 | 74.2 | 80 | .431 | |
| | 330 | 260 | 78.4 | 80 | .612 | |
| | 335 | 250 | 87.8 | 0 | .869 | |
| | 340 | 150 | 85.1 | 30 | 1.278 | |
| Poly-beta-deuterostyrene (5b)  | 340 | 450 | 41.5 | ---------- | 0.065 | 59 |
| | 345 | 440 | 53.0 | ---------- | .095 | |
| | 350 | 420 | 70.6 | ---------- | .135 | |
| | 360 | 300 | 93.0 | ---------- | .329 | |
| Polybenzyl  | 400 | 414 | 37.7 | 100 | 0.118 | 53 |
| | 410 | 430 | 67.0 | 60 | .265 | |
| | 420 | 320 | 74.3 | 40 | .438 | |
| | 430 | 250 | 82.9 | 50 | .724 | |

In figure 5 the curves of percentage volatilization plotted against time for poly-beta-deuterostyrene (5b), just as for polystyrene and poly-alpha-dueterostyrene [7, 8], show points of inflection. The broken lines in figure 5 for the logarithm of percentage residue plotted against time are curved and could not be used for calculating the rate constants. However, the initial rates are obtained by extrapolating the straight parts of the curves shown in figure 6. These lines were obtained by plotting rates of volatilization, expressed in percentage of residue per minute versus percentage of volatilization, as was done in the case of polystyrene and poly-alpha-dueterostyrene [7, 8].

Experimental conditions and results of rate studies are shown in table 8. In column 5 of table 8, the time, in minutes after the start, at which the break in the broken line for each rate experiment occurs is given. The initial rates are given in column 6. The activation energy was calculated from the initial rates by means of Arrhenius' equation [7]. These activation energies are shown in the last column of table 8.

## 4. Discussion

On the basis of experimental data on thermal degradation of polymers that have accumulated during the past few years, some conclusions can be drawn as to the mechanism of this type of degradation. It was found in the case of polyethylene [12] that even at temperatures below those at which appreciable loss by volatilization occurs, a drop in molecular weight of the polymer takes place. In the case of polystyrene [7, 14], poly-alpha- and poly-beta-dueterostyrene [14], polyisobutylene [18], high molecular weight polymethyl methacrylate [19], and polymethylene [10], it was found that at temperatures at which volatilization of the degradation products takes place, a more or less rapid drop in the molecular weight of the polymer takes place during the first few percentage losses, followed by a more gradual drop. This initial decrease in molecular weight under the influence of heat may be due to the presence of weak links caused by some foreign elements or groups of elements, such as O, $O_2$, and OH, which become incorporated in the chain during polymerization [4]. Such an assumption is legitimate because it is very difficult to carry out any polymerization in the absence of foreign materials.

The pattern of breakup of polymers, beyond the initial stage of degradation, varies with the nature of the polymer and the nature and frequency of side groups. A free-radical mechanism for the depolymerization of polymers has been proposed by Simha, Wall, and Blatz [20]. One of the important steps in this mechanism is intermolecular abstraction of hydrogen by free radicals. A free radical, which is formed initially through thermal breaks of the chains or through some other mechanism, abstracts a hydrogen from a polymer chain with which it happens to come in contact. This free radical becomes saturated in this action; the chain from which the hydrogen was abstracted breaks, for example, in the case of polymethylene, in the following manner:

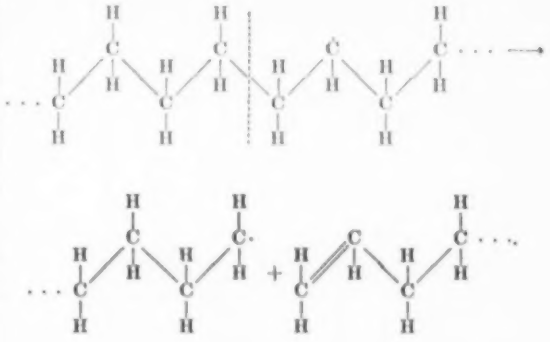

A double bond thus forms at one chain end at the break and a free radical at the other. However, instead of going through the step of abstraction, a free radical may break up into monomers:

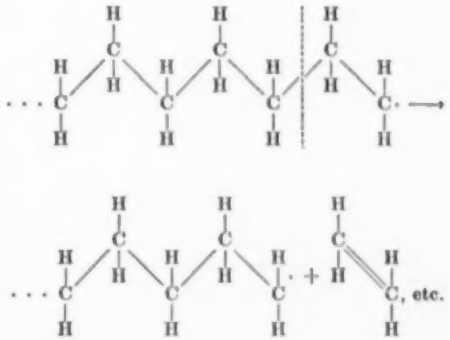


As to which of these two modes of reaction a free radical will follow depends on two factors: (1) the reactivity of the radical for abstracting hydrogen, and (2) the presence of hydrogen atoms susceptible to abstraction along the polymer chain. The reactivity of a free radical depends on its structure.

Thus, $RCH_2\cdot$, for example, is more reactive than $R_2CH\cdot$ [2]. As to the susceptibility of hydrogen on the chain, one attached to a tertiary carbon is more susceptible than a hydrogen attached to a secondary carbon in the chain.

Another mechanism of depolymerization can be visualized [8, 21] if we assume that a thermal break in a chain takes place simultaneously with an intramolecular transfer of hydrogen from the same chain

at the point of the break. Thus, taking again polymethylene as an example,

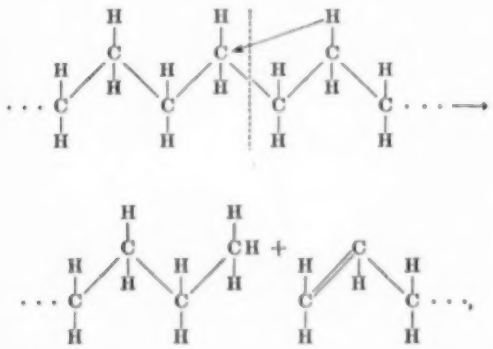

resulting in one saturated and one unsaturated end in the two parts of the chain. In the case of polymethylene, polyethylene, or polyvinylcyclohexane, where there is a large supply of hydrogen atoms attached to carbons in the chain or in the side groups, thermal breaks, proceeding as above, will result in the formation of large fragments, so that most of the volatiles from thermal degradation will be in fraction II. For poly-alpha-methylstyrene, polymethyl methacrylate, or polytetrafluoroethylene, where some or all of the hydrogen atoms are substituted by methyl groups or fluorine, thermal breaks result in two radicals formed at the break. These radicals proceed to break into monomers by a chain reaction. As a result, most of the volatiles are found in fraction III. Between these two extremes are polymers like polyisobutylene, which yield part monomer and part large fragments.

The fact that free radicals, in the case of polymethylene, for example, do not yield an appreciable amount of monomer is explained by Simha, Wall, and Blatz as due to a higher rate of transfer as compared to the rate of monomer formation. In the mechanism of thermal breaks, involving intramolecular transfer, scarcity of monomer in thermal degradation of polymethylene is evident from the nature of the thermal scission in which the free radicals become immediately saturated.

In table 9 the yield of fraction III is shown in weight and mole percent for 13 polymers. Four of these polymers have been studied in the present work; the rest were investigated previously. These polymers are arranged in two groups. In the first group, polymethylene has no side groups, polyethylene has side groups, or branches, at infrequent intervals, polypropylene has a hydrogen on every other carbon in the chain replaced with a methyl group, polyisobutylene has both hydrogens on every other carbon replaced with methyl groups, and polytetrafluoroethylene has all hydrogen atoms replaced with fluorine. Polymethylene and polyethylene yield the smallest amount of fraction III.

TABLE 9. *Yield of monomeric fraction in thermal degradation of polymers as a function of structure and side groups*

| Polymer | Yield of monomeric fraction in percentage of total volatilized part | | Reference |
|---|---|---|---|
| Group 1 | | | |
| | *wt %* | *Mole %* | |
| Polymethylene | 3 | 21 | |
| Polyethylene | 3 | 21 | [5] |
| Polypropylene | 14 | 57 | |
| Polyisobutylene | 32 | 78 | [5] |
| Polytetrafluoroethylene | 100 | 100 | [9] |
| Group 2 | | | |
| Polyvinylcyclohexane | 6 | 25 | [6] |
| Polybenzyl | 7 | 31 | |
| Polystyrene | 42 | 65 | [1] |
| Poly-beta-deuterostyrene (5a) | 42 | 68 | |
| Poly-meta-methylstyrene | 52 | 77 | [6] |
| Poly-alpha-deuterostyrene | 70 | 86 | [6] |
| Poly-alpha-methylstyrene | 100 | 100 | [6] |
| Polymethyl methacrylate | 100 | 100 | [6] |

This amount is the same for each polymer. For the other polymers of this group, there is a progressive increase of fraction III with increase of the number of replaced hydrogen atoms. It should be pointed out here, in connection with polytetrafluoroethylene, that when hydrogen and fluorine are both present on the chain, there is a tendency for some of the hydrogen to combine with fluorine to give HF [9].

In the second group of polymers we find polyvinylcyclohexane yielding only a little more of fraction III than polymethylene or polyethylene. Although here every other carbon in the chain has a cyclic group replacing hydrogen, the cyclic group itself has hydrogen available for abstraction during a thermal break, so that there is little chance for monomer formation. Polybenzyl, judging from the fact that there was no stilbene in the volatile products and that it has a high thermal stability, should have a structure in which the chain consists alternately of a phenyl and a $CH_2$ group, as pointed out before. Abstraction in such a polymer is difficult, and as a consequence, thermal breaks should result in formation of monomers. On the other hand, it is hard to see how a monomer could form from a free radical end in polybenzyl. The 31 mole percent of fraction III actually formed in the pyrolysis consists mainly of toluene and benzene and of a small amount of xylene. All these compounds require hydrogen for their formation, and this hydrogen must come by stripping the chain somewhere. Actually, the residue varied in color from light brown to almost black, depending on the extent of degradation.

Polystyrene, poly-beta-deuterostyrene, poly-meta-methylstyrene, and poly-alpha-deuterostyrene all yield considerable amounts of monomer. Although these polymers have the same amount of hydrogen atoms on the chain as polypropylene, the yield of monomer is much greater here, particularly if we consider the fact that fraction III for polypropylene, as seen from table 3, has very little monomer, whereas for polystyrenes it is almost all monomer (tables 5 and 6 and references [1, 5, 6]). Apparently

the phenyl group, because of steric hindrance, reduces the tendency of the hydrogen atoms on the chain to transfer intramolecularly during a thermal scission. This results in an increased yield of monomer. The low average molecular weight of fraction II from these styrene polymers (table 7 of the present paper and table 2 of reference [8]) indicates that this fraction consists chiefly of the dimer, trimer, and tetramer. As pointed out in a previous paper [8], the dimer, trimer, and tetramer could form, along with monomer, in the same chain reaction, at a free radical end, as follows:

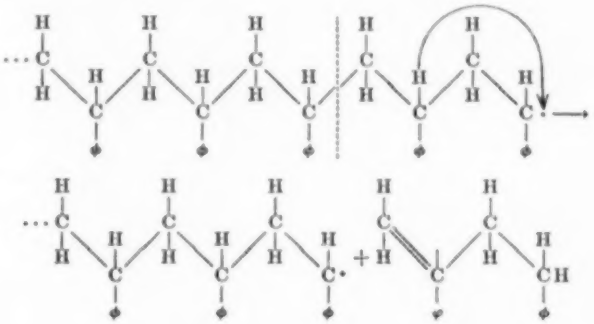

Dimer

Substitution of a beta-hydrogen with deuterium does not affect the monomer yield; substitution of a hydrogen on the phenyl group with a methyl group increases this yield; substitution of an alpha-hydrogen with deuterium increases the monomer yield considerably. When the alpha-hydrogen is substituted with a methyl group, the monomer yield reaches 100 percent. Hydrogen on the tertiary carbon (alpha-position) is more susceptible to transfer than that on a secondary carbon (beta-position) [20], and blocking the alpha-position with a deuterium atom or with a methyl group favors the formation of monomer at the expense of dimer, trimer, or tetramer. In polymethyl methacrylate the monomer is the only volatile product of degradation. Steric hindrance, caused here by the ester group, and blocking of the alpha-hydrogen with a methyl group, produce the same effect on monomer yield as in the case of poly-alpha-methylstyrene.

Table 10 shows a series of 13 polymers arranged in the order of rates of thermal degradation at 350° C. Five of these polymers have been the subject of the present investigation; the others were studied previously [7, 8, 9]. Actually, the rates of only a few polymers were measured at 350° C; the other rates were studied at temperatures either below or above 350° C. In these latter cases the rates corresponding to 350° C were calculated from the actual rates measured at other temperatures, by means of Arrhenius' equation, in the form of

$$\log_{10} k_1 = -\frac{E\left(\frac{1}{T_1}-\frac{1}{T_2}\right)}{2.303R}+\log_{10} k_2,$$

where $k_1$ and $k_2$ are rates, in percent, of original sample per minute at corresponding absolute temperatures $T_1$ and $T_2$, $R$ is the gas constant in calories, and $E$ is the activation energy, in calories.

Polymer chains when heated tend to break at their weakest points. The strength of a C—C bond in a chain follows the order given below:

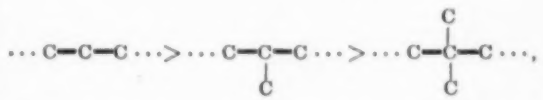

the bond shown as a heavy line being the one under consideration. Thus, breaks will occur more readily in bonds adjacent to a tertiary or quaternary carbon in the chain.

A bond in the beta-position to a double bond in the chain, or in its side groups, is another source of weakness in a C—C bond in the chain. An abundance of hydrogen on a chain facilitates saturation of the free-radical ends formed during a thermal break. When all the hydrogen atoms on the chain are replaced with fluorine atoms, this saturation does not take place due to the greater strength of the C—F bond as compared with the C—H bond.

With these considerations of bond weaknesses in mind, we find in table 10 that polytetrafluoroethylene is the most thermally stable polymer. Next to this polymer is polymethylene, which has only secondary carbons in the chain and an abundance of hydrogen atoms on the carbons. Polybenzyl occupies a position below polymethylene in this table. At a temperature of about 400° to 420° C, polybenzyl is actually more stable than polymethylene, but because of a lower activation energy than in the case of polymethylene, the position is reversed at a lower temperature. The phenyl group, which is here a part of the chain, seems to impart stability to it, perhaps through resonance. Polyethylene has an abundance of hydrogen on the chain and a few tertiary carbons. Its position in the series is next

TABLE 10. *Rates of thermal degradation of polymers in a vacuum at 350° C*

| Polymer | Volatilization, in percent, of original sample | Reference |
|---|---|---|
| | %/min | |
| Polytetrafluoroethylene | 0.000002 | [9] |
| Polymethylene | .004 | ..... |
| Polybenzyl | .006 | ..... |
| Polyethylene | .008 | [7] |
| Polypropylene | .069 | ..... |
| Poly-β-deuterostyrene (5b) | .14 | ..... |
| Polystyrene | .24 | [7] |
| Poly-α-deuterostyrene | .27 | [8] |
| Polyvinylcyclohexane | .45 | [8] |
| Poly-meta-methylstyrene | .90 | [8] |
| Polyisobutylene | 2.4 | ..... |
| Polymethyl methacrylate | 5.2 | [8] |
| Poly-α-methylstyrene | 230 | [8] |

to polymethylene and polybenzyl. Next comes polypropylene, with every other carbon in the chain of a tertiary type. Next in the series are poly-beta-deuterostyrene, polystyrene, poly-alpha-deuterostyrene, and poly-meta-methylstyrene, with every other carbon being of a tertiary type and every bond in beta-position to a double bond in the phenyl group. Polyvinyl cyclohexane, with every other carbon in the chain of tertiary type and an abundance of hydrogen available for transfer, occupies a position between two polystyrenes. Polyisobutylene and polymethyl methacrylate, both having every other carbon in the chain of the quaternary type, come next, with very high rates of volatilization. Finally, poly-alpha-methylstyrene, with every other carbon in the chain of the quaternary type and every bond in the chain in beta-position to a double bond in a phenyl group, is the most thermally unstable polymer of the series.

Thus, we see from a study of a number of polymers that the pattern of their thermal degradation, the types and relative amounts of the volatile products produced in pyrolysis, and their stability in a vacuum, in the temperature range of about 200° to 500° C, are functions of their molecular structure and of the kind and frequency of side groups.

## 5. References


[1] S. L. Madorsky and S. Straus, J. Research NBS **40,** 417 (1948) RP 1886; Ind. Eng. Chem. **40,** 484 (1948).
[2] L. A. Wall, J. Research NBS **41,** 315 (1948) RP1928.
[3] R. B. Seymour, Ind. Eng. Chem. **40,** 524 (1948).
[4] H. H. G. Jellinek, J. Polymer Sci. **4,** 13 (1949).
[5] S. L. Madorsky, S. Straus, D. Thompson, and L. Williamson, J. Research NBS **42,** 499 (1949) RP1989; J. Polymer Sci. **4,** 639 (1949).
[6] S. Straus and S. L. Madorsky, J. Research NBS **50,** 165 (1953) RP2405.
[7] S. L. Madorsky, J. Polymer Sci. **9,** 133 (1952).
[8] S. L. Madorsky, J. Polymer Sci. **11,** 491 (1953).
[9] S. L. Madorsky, V. E. Hart, S. Straus, and V. A. Sedlak, J. Research NBS **51,** 327 (1953) RP2461.
[10] L. A. Wall, S. L. Madorsky, D. W. Brown, S. Straus, and R. Simha, J. Am. Chem. Soc. **76,** 3430 (1954).
[11] N. Grassie and H. W. Melville, Proc. Royal Soc. (London) **199,** 1 (1949).
[12] W. G. Oakes and R. R. Richards, J. Am. Chem. Soc. **619,** 2929 (1949).
[13] L. Mandelkern, M. Hellmann, D. W. Brown, D. E. Roberts, and F. A. Quinn, Jr., J. Am. Chem. Soc. **75,** 4093 (1953).
[14] L. A. Wall, D. W. Brown, and V. E. Hart, J. Polymer Sci. (in press).
[15] D. R. Stull, Ind. Eng. Chem. **39,** 517 (1947).
[16] M. C. Haas, D. I. Livingston, and M. L. Saunders, Polaroid Corporation, Cambridge, Mass. (private communication).
[17] Samuel Glasstone, Textbook of physical chemistry, 2d ed., p. 1046 (D. Van Nostrand Co., New York, N. Y., 1946).
[18] V. A. Golubtzova, Doklady Akad. Nauk S. S. S. R. **84,** 701–703 (1952).
[19] V. E. Hart, National Bureau of Standards (unpublished work).
[20] R. Simha, L. A. Wall, and P. J. Blatz, J. Polymer Sci. **5,** 615 (1950).
[21] H. Staudinger and A. Steinhofer, Ann. Chem., Justus Liebigs **517,** 35 (1935).


WASHINGTON, June 14, 1954.

Journal of Research of the National Bureau of Standards Vol. 53, No. 6, December 1954 Research Paper 2554

# Some Properties of Strontium Hydroxide and Its Monohydrate

Elmer T. Carlson

Strontium hydroxide, $Sr(OH)_2$, was prepared by hydration of strontium oxide under pressure at 400° C. The monohydrate was prepared by hydration of the oxide at 168° C. and also by evaporation of a boiling solution of strontium hydroxide. Optical properties and X-ray powder diffraction patterns are given.

## 1. Introduction

Strontium hydroxide, in the form of its octahydrate, $Sr(OH)_2 \cdot 8H_2O$, is a substance familiar to the chemist. Various lower hydrates have been postulated from time to time, but there seems to be little evidence of the existence of any except the monohydrate, $Sr(OH)_2 \cdot H_2O$. Dehydration studies by several investigators [1,2,3] [1] give fairly definite data concerning the dissociation of the octahydrate and of the unhydrated hydroxide.

Equations relating the dissociation pressures of strontium hydroxide and its octahydrate to temperature are given by Tamaru and Siomi [3]. From these equations, the temperature at which the dissociation pressure reaches 760 mm is calculated to be 92° C for $Sr(OH)_2 \cdot 8H_2O$ and 701° C for $Sr(OH)_2$. The shape of the dissociation curve indicates that a monohydrate exists, but its dissociation temperature is not clearly defined.

In view of the amount of work done on $Sr(OH)_2$ and its monohydrate, it is somewhat surprising that there appears to be no published data on the optical properties of these compounds. X-ray diffraction patterns were published by Hüttig and Arbes [1], but in such form that they are very difficult to translate in terms of interplanar spacings, or even to use as a basis for identification.

In connection with some hydrothermal studies of strontium compounds, it was necessary to be able to identify the various forms of the hydroxide. Accordingly, the hydroxide and its monohydrate were prepared, and their more useful identifying properties determined.

## 2. Procedure and Results

Strontium carbonate, reagent grade, was heated at 1,300° C to convert it to the oxide. The dry oxide was then exposed to water vapor in a pressure bomb at 400° C for 3 days. The product was a dry powder containing 0.98 mole of water per mole of SrO, closely approximating the composition of $Sr(OH)_2$. The crystals averaged about 20 $\mu$ in diameter, but were somewhat rounded and irregular, so that the ideal shape could not be determined. They appeared to be in the form of relatively thick plates. The crystals described were prepared with a moderate excess of water in the bomb. Reducing the water to the stoichiometric quantity resulted in crystals that were much smaller but of the same composition. The optical properties are as follows: Refractive indices, $\alpha=1.588$, $\beta=1.599$, and $\gamma=1.610$; character, biaxial; sign, positive; and optic axial angle 2V, nearly 90°.

Hydrothermal treatment of strontium oxide at 168° C, in the presence of a slight excess of water, resulted in a product having 1.95 moles of $H_2O$ per mole of SrO, approximately the composition of $Sr(OH)_2 \cdot H_2O$. The crystals were larger than those described above but quite irregular in shape. The indices are $\alpha=1.570$, $\beta=1.589$, and $\gamma=1.610$; character, biaxial; sign, positive; and 2V nearly 90°. The similarity in optical properties points to a close relationship between the hydroxide and its monohydrate, which is borne out by the similarity of the X-ray patterns.

The monohydrate was also obtained by slow evaporation of a saturated solution of strontium hydroxide at the boiling point. Many of the larger crystals were in the form of hexagonal prisms, although it is evident from the optical properties that the symmetry cannot be truly hexagonal. The preparation, when dried at 110° C, lost weight equivalent to 1.23 moles of water. At 900° C it lost an additional 1.02 moles, corresponding to conversion to SrO. The loss at 110° C is evidently due to the expulsion of the 1 molecule of water of hydration, the small excess presumably resulting either from entrapped moisture or from the presence of a small amount of the octahydrate. Most of the precipitated hydroxide adhered tenaciously to the flask, and there was microscopic evidence of reaction with the glass, with the formation of minute crystals of strontium silicate hydrate ($3SrO \cdot 2SiO_2 \cdot 4H_2O$) [4]. The fact that strontium hydroxide monohydrate is formed under these conditions indicates that it is the stable phase at the boiling point.

[1] Figures in brackets indicate literature references at the end of this paper.

TABLE 1. *Interplanar spacings and relative intensities of X-ray diffraction lines for strontium hydroxide and its monohydrate*

| $Sr(OH)_2$ | | $Sr(OH)_2 \cdot H_2O$ | |
|---|---|---|---|
| *d* | *I* | *d* | *I* |
| Å | | Å | |
| 6.21 | 17 | 6.18 | 100 |
| 5.21 | 80 | 4.54 | 95 |
| 4.95 | 25 | 3.65 | 25 |
| 4.56 | 14 | 3.36 | 44 |
| 4.14 | 3 | 3.14 | 60 |
| 3.847 | 55 | 2.95 | 7 |
| 3.651 | 7 | 2.84 | 35 |
| 3.358 | 7 | 2.81 | 78 |
| 3.302 | 38 | 2.47 | 30 |
| 3.132 | 100 | 2.36 | 8 |
| 3.073 | 23 | 2.29 | 50 |
| 2.922 | 30 | 2.23 | 80 |
| 2.903 | 58 | 2.10 | 14 |
| 2.848 | 5 | 2.07 | 14 |
| 2.815 | 8 | 1.974 | 18 |
| 2.747 | 10 | 1.824 | 23 |
| 2.602 | 4 | 1.815 | 7 |
| 2.473 | 35 | 1.798 | 4 |
| 2.343 | 62 | 1.760 | 10 |
| 2.294 | 24 | 1.750 | 8 |
| 2.168 | 16 | 1.737 | 6 |
| 2.107 | 3 | 1.693 | 8 |
| 2.093 | 28 | 1.678 | 7 |
| 1.978 | 7 | 1.625 | 15 |
| 1.960 | 27 | 1.603 | 7 |
| 1.947 | 60 | 1.585 | 7 |
| 1.887 | 25 | 1.549 | 12 |
| 1.835 | 5 | 1.531 | 12 |
| 1.823 | 3 | 1.518 | 6 |
| 1.810 | 18 | 1.510 | 2 |
| 1.746 | 9 | 1.481 | 7 |
| 1.697 | 24 | 1.426 | 4 |
| 1.661 | 9 | 1.407 | 8 |
| 1.649 | 9 | 1.378 | 8 |
| 1.624 | 17 | 1.368 | 2 |
| 1.574 | 7 | 1.340 | 6 |
| 1.535 | 10 | 1.313 | 10 |
| 1.530 | 11 | 1.303 | 2 |
| 1.512 | 5 | 1.287 | 6 |
| 1.4942 | 4 | 1.267 | 4 |
| 1.4895 | 3 | 1.235 | 13 |
| 1.4742 | 4 | 1.227 | 4 |
| 1.4600 | 9 | 1.219 | 2 |
| 1.3764 | 3 | 1.211 | 2 |
| 1.3585 | 10 | | |
| 1.3076 | 5 | | |
| 1.2825 | 7 | | |
| 1.2664 | 8 | | |
| 1.2343 | 4 | | |
| 1.2308 | 5 | | |
| 1.2187 | 11 | | |
| 1.2065 | 4 | | |
| 1.1969 | 3 | | |
| 1.1794 | 6 | | |
| 1.1693 | 6 | | |
| 1.1288 | 7 | | |
| 1.1000 | 3 | | |
| 1.0731 | 3 | | |
| 1.0567 | 3 | | |
| 1.0297 | 3 | | |
| 1.0055 | 3 | | |

X-ray powder diffraction patterns for the two compounds are given in table 1. These were made with an X-ray Geiger-counter diffractometer, using copper K$\alpha$ radiation. It may be noted that the two patterns are quite similar, especially in the size of the larger spacings.

## 3. Summary

Strontium hydroxide and its monohydrate have been prepared, and their optical properties determined. The refractive indices are: for $Sr(OH)_2$, $\alpha=1.588$, $\beta=1.599$, and $\gamma=1.610$; for $Sr(OH)_2 \cdot H_2O$, $\alpha=1.570$, $\beta=1.589$, and $\gamma=1.610$. Both are biaxial, positive, with 2V near 90°. X-ray diffraction patterns are given.

---

The author acknowledges with thanks the assistance of G. M. Ugrinic, who prepared the X-ray patterns, and A. Van Valkenburg, who checked the refractive indices.

## 4. References

[1] G. F. Hüttig and A. Arbes, Z. anorg. u. allgem. Chem. **192,** 225 (1930).
[2] C. Nogareda, Rev. acad. cienc. exact., fís.-quím. y nat. Madrid **26,** 315 (1931); Chem. Abstr. **26,** 1869 (1932).
[3] S. Tamaru and K. Siomi, Z. physik Chem. [A] **171,** 221, 229 (1934).
[4] E. T. Carlson and L. S. Wells, J. Research NBS **51,** 73 (1953) RP2433.

WASHINGTON, August 30, 1954.

Journal of Research of the National Bureau of Standards Vol. 53, No. 6, December 1954 Research Paper 2555

# Refractivity Measurements on Canada Balsam by Interferometry

James B. Saunders

The index of refraction of three different samples of Canada balsam, each obtained from a different source, was measured for thirteen spectral lines in the visible range by means of the Fabry-Perot interferometer. This instrument permits absolute measurements when the method of coincidence (or method of exact fractions) is applied to fringes produced in thin films of the material being tested. High accuracy may be obtained by applying the method to fringes produced in films of successively increasing thickness.

## 1. Introduction

The increasing requirements for precision optical tools have expanded the need for more precise measurements on the refractive index of optical cements. The author was faced with this problem in the design of a "Kösters interferometer",[1] in which a film of optical cement appears in one of the component light beams. If white light is to be used, as was desired, the film of cement should be compensated for. This is easily effected if the two prisms, required for this instrument are made of glass that has optical properties similar to the cement used to bind them together. In order to select a suitable glass-cement combination it is necessary that the optical properties be sufficiently well known.

The basic principle used for these measurements is the determination of optical and geometrical thicknesses of a nearly parallel film by interference of light. This method of measuring refractive indices was selected because of its convenience and applicability to the measurements of indices for the many spectral lines desired. It is suitable for all transparent liquids as well as other materials that may be molded into optical films or wedges. Fair accuracy is obtainable on thin films, such as those usually used for cementing optical elements, and increasing accuracy is obtainable with films of increasing thickness. Several spectral lines are used for applying the "method of coincidence",[2] and values are obtained for each of the lines used. An accuracy of five in the fourth decimal place of index is obtainable with a single-specimen assembly, forming a film 0.1 mm thick, if the sample is completely unknown. An increase over the above-mentioned accuracy, by a factor of one hundred, is obtainable with a second specimen, if a most favorable choice of film thickness is made and temperatures are sufficiently well-controlled. The preparation of a sample that is completely unknown differs somewhat from that of a sample known to an accuracy of one or better in the second decimal place of index. If an accuracy exceeding five in the fourth decimal place is desired on an unknown sample, two or more specimens are mounted concurrently to insure homogeneity of index from one specimen to the other. The ultimate accuracy obtainable by this method is limited chiefly by temperature control, variations in index among the several assembled specimens, and the accuracy of the wavelength of the light used. Temperature appears to be the dominant factor.

[1] Werkstatts Technik und Werksleiter **23**, 23 (1938).

[2] A. Perot and Chas. Fabry, Méthodes interférentielles pour la mesure des grandes epaisseurs et la comparison des longuers d'onde, Ann. chim. et phys. **16**, 289 (1899).

## 2. Method of Test

### 2.1. Temperature Considerations

A change of 1 deg C in the temperature of Canada balsam produces a change of from 2 to 5 (depending upon wavelength) in the fourth decimal place of refractive index. The temperatures of the specimen varied between 26° and 28° C, but were measured to better than 0.1 deg C and the results corrected to 27° C. Temperature coefficients, sufficiently accurate for applying the method of coincidence, were obtained for a few spectral lines by observing the changes in orders of interference for measured temperature changes. The coefficients used in computing the final results, however, were values resulting from a statistical analysis of all the data.

### 2.2. Mounting of Specimens

Specimens of three samples of Canada balsam were cooked to a consistency considered proper for use by an experienced optical worker. As an accuracy of one in the fourth decimal place was considered adequate, two specimens of each of the three samples were mounted as follows: Two rectangular plates of glass (see fig. 1,A), approximately 2 by 7 in., with good optical surfaces, were each coated on one side with a partially transmitting, high-reflecting coat of aluminum. Samples from each of the three cements were drawn to long thin threads and placed parallel to each other on one of the coated surfaces and parallel to the long sides. Two spacers, shown in figure 1,A, that are approximately 0.1 mm thick and equal to within 0.001 mm, were also placed on this surface, and the second coated surface was placed on the three specimens. This combination

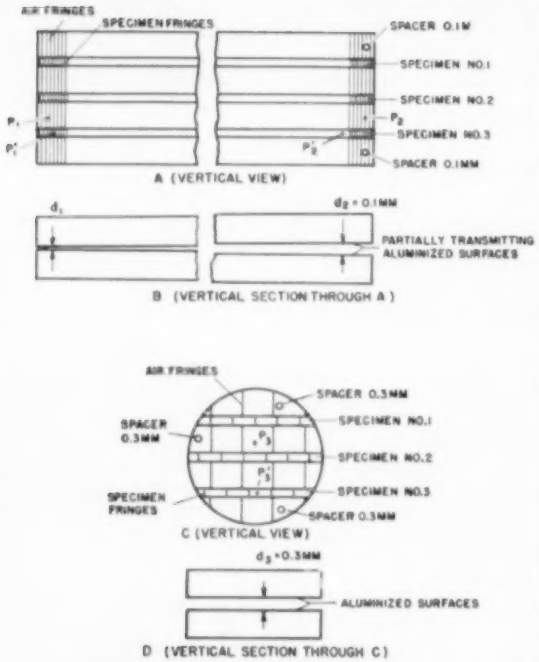


FIGURE 1. *Schematic representation of interferometer plates.*

*A* represents the assembly of the two 2- by 7-in. Fabry-Perot interferometer plates forming a wedge, with the two spacers, $S_1$ and $S_2$, controlling the angle. The three specimens conform to the wedge angle. The thickness of the wedge approximates zero at one end of the plates and the thickness of the two equal spacers at the other; *B* is a vertical section through *A*; *C* is similar to assembly *A*, except that three spacers are used to form a thicker and nearly parallel film with a specific direction for the refracting edge of the wedge; *D* is a vertical section through *C*

was then placed in an oven and heated to a temperature at which the cement softens and fuses to the aluminized surfaces. A rigid body weighing several ounces was heated with the plates. This weight was then placed on the top plate to press the cement threads into narrow ribbons that became quite thin at one end and approximately to the thickness of the two spacers at the other end.

A second set of specimens, one from each of the three samples of cement, was drawn to threads larger than those of the set shown in figure 1,A, and placed parallel to each other on circular flat plates, each of which was also coated with a partially transmitting film of aluminum. The circular plates were 1 in. in diameter. Three spacers are placed on this film, as shown in figure 1,C. The relative thicknesses of these spacers were previously adjusted by grinding to produce a most favorable wedge (approximately three fringes of green light) for reading the interference fringes when they serve as spacers between the two Fabry-Perot interferometer plates. The thickness of these spacers was approximately 0.3 mm. In order to apply the method of exact fractions the approximate thickness at the reference point is measured to within 0.01 mm. This can be obtained with a good micrometer. A second plate, similar to the one on which these last specimens were mounted, was then placed on the specimens and the assembly placed in the furnace, along with the previously described assembly. These specimens are also pressed into ribbons by means of a weight on the top plate. The thickness of these ribbons of Canada balsam will approximate that of the three spacers. If the relative thicknesses of these spacers are properly adjusted, the fringes of interference, formed by light reflected from the highly reflecting surfaces when the plates are assembled into a Fabry-Perot interferometer, will be nearly normal to the ribbons. This orientation is most favorable for reading the orders of interference. A small wedge between the reflecting surfaces, producing approximately five fringes, is also quite favorable to reading the orders of interference. With these most favorably orientated and spaced Fabry-Perot fringes, the fractional orders of interference of the several spectral lines can be measured to one-hundredth. For a thickness of 0.3 mm this corresponds to approximately one in the fifth decimal place of index. An error of 0.01 mm in the observed order of interference is, therefore, negligible. When the two assemblies are cooled to ambient temperatures the cement binds the plates together for convenience of handling.

### 2.3. Reading of Fringes

The rectangular-plate assembly was mounted vertically, with the specimen ribbons running horizontally, on a small adjustable bench milling-machine base. A collimated beam of light, from a monochromator and line source, was projected normally through the surfaces. The light was received with a low-power, short-focus telescope that was focused on the ribbon films. Multiple-beam-reflection interference fringes were observed in each of the specimens and also in the spaces between them. For purpose of discussion the fringes seen between and outside the area of the specimens will be called "air fringes," and those inside the area of the specimens, "specimen fringes."

The milling-machine base permits measurable movements of the plate in the focal plane of the telescope. Thus, a panoramic view of the whole plate is observable in the telescope, and the micrometer permits accurate measurements to be made on the fractional orders of interference.

The orders of interference of air fringes for all wavelengths of light used were determined at $P_1$, where the separation of the plates is $d_1$, by means of the method of coincidence. This is an easy and positive test because $d_1$ is known to be very small. With all orders of interference known at $P_1$, the orders of interference are determined at $P_2$ by counting the number of fringes between these two points and adding them to the order values at $P_1$. The narrowness of the samples, with the fringes nearly normal to their lengths, permits a determination of the orders of the air fringes interpolated to points

$P_1'$ and $P_2'$, although these points are in the region of the specimen fringes. If the reflecting surfaces are plane (resulting in straight fringes), the order of interference, at a point in the wedge that is adjacent to but outside the area of the fringes, may be accurately measured with a moveable reticule in the eye piece of the viewing instrument.[3]

The number of specimen fringes between points $P_1'$ and $P_2'$ is obtained by counting as the plates are moved, with the adjustable support, so as to cause $P_2'$ to move into the position of $P_1'$. The ratio of the number of specimen fringes to the number of air fringes between $P_1'$ and $P_2'$ is the refractive index of the specimen relative to air. This ratio is also equal to the corresponding ratios of orders of interference at any point. As the order is low at $P_1$ (10 to 20 in the case of this test), the computed order for the specimen fringes at $P_1'$ will give the integral part of the order number to absolute accuracy, and the fractional part is observed directly. The order at $P_1'$ plus the number of fringes between $P_1'$ and $P_2'$ is the absolute order at $P_2'$. The ratio of orders of specimen and air fringes at $P_2'$ is the accepted value for the refractive index of the specimen obtainable with this assembly.

By using the above procedure, the refractive index is obtained for all spectral lines used. A similar treatment also permits measurements for the other two specimens. The order number of the air fringes at $P_2'$ was approximately 400 ($\lambda$=0.5 $\mu$), and the fraction is known to one-tenth, even though these narrow fringes are unfavorable for best precision. This, however, corresponds to a precision of about four in the fourth decimal place of refractive index.

The accuracy of index values, determined by this method and assuming constant temperature control, depends upon the thickness of the specimen and the accuracy with which the fractional parts of the orders can be determined. The second set of specimens, assembled concurrently with the set discussed above and shown in figure 1, C, permit an increased accuracy of the measured indices. The rectangular plates are replaced by the circular plates on the adjustable base, and the order numbers for the air fringes are determined at some chosen point, $P_3$, by means of the method of exact fractions. The thickness of the air film at $P_3$ is approximately three times that at $P_2$, consequently the computed orders for the specimen fringes at $P_3'$, using the results obtained at $P_2'$, will be in error by not more than three-tenths of a unit. The integral part is, therefore, determined with absolute certainty. As the fringes are very narrow relative to their spacing and as a most favorable spacing was chosen, the errors in the fractional parts are believed to be less than one-hundredth of a unit. The order number at $P_3'$ was approximately 1,200 ($\lambda$=0.5 $\mu$). Consequently, errors in the refractive indices, resulting from the order determinations, are negligible compared to those resulting from temperature.

[3] J. B. Saunders, J. Research NBS **23**, 182 (1939) RP1227.

## 3. Results

Three different samples of Canada balsam, each obtained from different places, were measured for 13 visible spectral lines, distributed as uniformly as available sources permitted. Sample 1 had been bleached for a prolonged period by continuous outdoor exposure over a period of approximately 2 years in direct sunlight and was almost free from color. Sample 2 was light yellow and is believed to have been chemically bleached. Sample 3 was dark brown and unbleached. All three were in liquid form.

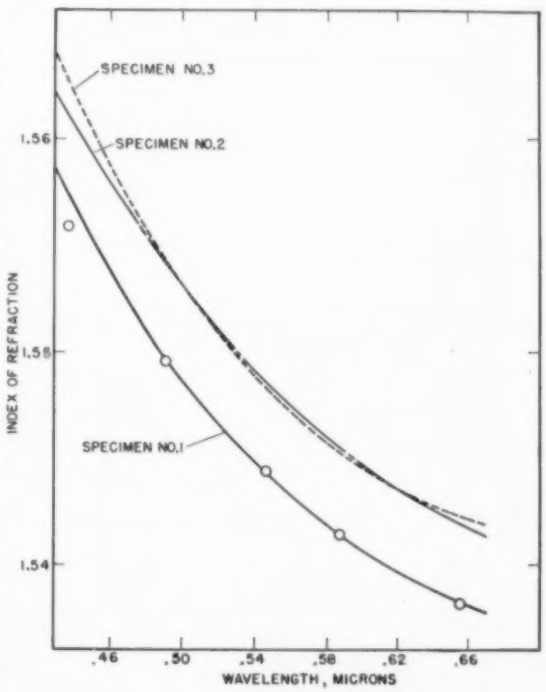


FIGURE 2. *Graphical representation of results.*

The curves represent the refractive index of three samples of Canada balsam. The circles represent discrete values for an available optical glass, chosen as most similar to that of specimen 1.

The three curves in figure 2 represent the most probable index values, corrected to 27° C. The values for these curves were computed from an equation relating index to wavelength and temperature. The parameters were evaluated statistically. The computed dispersions ($\mu$-values) for samples 1, 2, and 3 are 43.5, 41.1, and 42.4, respectively. The circles in figure 2 represent index values for an available optical glass. Except for short wavelengths, specimen 1 is seen to be quite adequate for the construction of a Kösters interferometer prism from the glass represented.

WASHINGTON, July 15, 1954.

Journal of Research of the National Bureau of Standards Vol. 53, No. 6, December 1954 Research Paper 2556

# Bounds on a Distribution Function That Are Functions of Moments to Order Four[1]

Marvin Zelen

Explicit expressions are presented for bounds on a distribution function when moments to order four are known. These inequalities are given in a form suitable for applications.

## 1. Introduction and Statement of Problem

Tchebycheff [7] [2] in 1874 proposed a problem that can be stated as follows: Let $F(y)$ be an unknown distribution function over the closed interval [3] $[a, b]$, and satisfying the conditions

$$F(a-0)=0$$

$$m_j=\int_a^b y^j dF(y) \qquad (j=0, 1, \ldots, k).$$

If the moments $m_j$ for $j=0,1, \ldots, k$ are known, then for a given value of $x$, $(a<x<b)$, what are the (sharp) upper and lower bounds on $F(x)$?

Tchebycheff presented without proof a solution to the above problem, which is sometimes called the reduced-moment problem. Proofs were later given by Markoff [1], Possé [2], and Stieltjes [5,6]. The book by Shohat and Tamarkin [4] gives an account of some of the modern-day treatments of the subject.

This paper presents the explicit expressions for solutions of the moment problem (often referred to as the Tchebycheff-Markoff inequalities) for the cases $k=2,3,4$. Inequalities that are functions of moments to order two were given by Tchebycheff [7] for distributions over the interval $[0,b]$. Inequalities that are functions of moments to order three were given by Possé [2]. Possé also solved the case of four moments for distributions over the interval $[a, \infty)$.

## 2. Explicit Expressions for Bounds

This section presents without proof the explicit expressions for bounds on a distribution function. Proofs may be found in [9]. These are derived as special cases of the Tchebycheff-Markoff inequalities.

In all that follows it will be assumed that

$$m_0=1, \quad m_1=0, \quad m_2=1. \tag{1}$$

This will result in no loss of generality, as any distribution function can be made to conform to these conditions by the use of a linear transformation. The assumption (1) implies that $a$, $b$ satisfy the inequalities

$$\left.\begin{aligned} &a<0<b \\ &1+ab\leq 0. \end{aligned}\right\} \tag{2}$$

This follows from the necessary conditions for the solution of the moment problem (cf. Shohat and Tamarkin [4]).

[1] A condensation of certain results obtained by the author in a thesis submitted to the University of North Carolina in June 1951 in partial fulfillment of the requirements for the Master of Arts degree.

[2] Figures in brackets indicate the literature references at the end of this paper.

[3] Throughout this paper it will be understood that a distribution function over the interval $[a, b]$ is one where the range of the random variable is $[a, b]$, and the end points will belong to that interval unless the end points are $-\infty$ or $+\infty$.

### 2.1. Bounds for Two Moments

Let $F(y)$ be a distribution function on $[a, b]$ with known moments

$$m_0=1, \quad m_1=0, \quad m_2=1$$

then for a given $x$, $(a<x<b)$,

$$0\leq F(x)\leq \frac{1}{1+x^2} \qquad \text{if } a<x\leq -\frac{1}{b} \tag{3}$$

$$\frac{1+bx}{(a-b)(a-x)}\leq F(x)\leq 1-\frac{1+ax}{(b-a)(b-x)} \qquad \text{if } -\frac{1}{b}\leq x\leq -\frac{1}{a} \tag{4}$$

$$\frac{x^2}{1+x^2}\leq F(x)\leq 1 \qquad \text{if } -\frac{1}{a}\leq x<b. \tag{5}$$

For any distribution defined over $(-\infty, \infty)$ inequalities (3) and (5) hold for $x<0$ and $x>0$, respectively.

### 2.2. Bounds for Three Moments

Let $F(y)$ be a distribution function on $[a, b]$ with known moments

$$m_0=1, \quad m_1=0, \quad m_2=1, \quad m_3.$$

Let $g(x)=x^2-m_3x-1$, and define

$$z_1=\frac{m_3-(a+x)}{1+ax}$$

$$z_2=\frac{m_3-(b+x)}{1+bx}$$

$$w=\frac{m_3-(a+b)}{1+ab}$$

$$A(\alpha,\beta,\gamma)=\frac{1+\alpha\beta}{(\gamma-\alpha)(\gamma-\beta)},$$

then for a given $x$, $(a<x<b)$

$$0\leq F(x)\leq A(b, z_2, x) \qquad \text{if } x<0,\ g(x)\geq 0 \tag{6}$$

$$A(x, z_1, a)\leq F(x)\leq A(x, z_1, a)+A(a, z_1, x) \qquad \text{if } g(x)\leq 0,\ x\leq w \tag{7}$$

$$A(x, b, z_2)\leq F(x)\leq A(x, b, z_2)+A(b, z_2, x) \qquad \text{if } g(x)\leq 0,\ x\geq w \tag{8}$$

$$1-A(a, z_1, x)\leq F(x)\leq 1 \qquad \text{if } g(x)\geq 0,\ x>0. \tag{9}$$

Inequalities (7) and (9) hold for any distribution $F(y)$ on $[a, \infty)$. Inequalities (6) and (8) hold for any distribution $F(y)$ on $(-\infty, b]$. Note that none of the inequalities (6) to (9) holds for distributions over $(-\infty, \infty)$.

### 2.3. Bounds for Four Moments

Let $F(y)$ be a distribution function on $[a, b]$ with moments

$$m_0=1, \quad m_1=0, \quad m_2=1, \quad m_3, \quad m_4.$$

Let

$$g(y,\gamma)=y^2+\left[\frac{\gamma-m_3+\gamma(\gamma m_3-m_4)}{1+\gamma(m_3-\gamma)}\right]y+\left[\frac{\gamma m_3-m_4+(m_3-\gamma)^2}{1+\gamma(m_3-\gamma)}\right].$$

$U(y)=g(y,a)$, $V(y)=g(y,b)$, $Z(y)=g(y,x)$, and let $u_1<u_2$, $v_1<v_2$, $z_1<z_2$ be the distinct zeros of $U(y)$, $V(y)$, $Z(y)$, respectively, then $a<v_1<u_1<v_2<u_2<b$.

Define

$$z_3=\frac{m_3(a+b+x)-m_4-ab-ax-bx}{abx+a+b+x-m_3}$$

$$A=\frac{m_4-m_3^2-1}{(1+x^2)(m_4-m_3^2-1)+(x^3-m_3x-1)^2}$$

$$B(\alpha,\beta,\gamma)=\frac{m_3-(\alpha+\beta+z_3)-\alpha\beta z_3}{(\gamma-\alpha)(\gamma-\beta)(\gamma-z_3)},$$

then for a given value of $x$, $(a<x<b)$,

$$0\leq F(x)\leq A \qquad \text{if } a<x\leq v_1. \tag{10}$$

$$B(b,x,a)\leq F(x)\leq B(b,x,a)+B(a,b,x) \qquad \text{if } v_1\leq x\leq u_1 \tag{11}$$

$$\frac{1+xz_2}{(z_1-x)(z_1-z_2)}\leq F(x)\leq \frac{1+xz_2}{(z_1-x)(z_1-z_2)}+A \qquad \text{if } u_1\leq x\leq v_2 \tag{12}$$

$$1-B(a,b,x)-B(a,x,b)\leq F(x)\leq 1-B(a,x,b) \qquad \text{if } v_2\leq x\leq u_2 \tag{13}$$

$$1-A\leq F(x)\leq 1 \qquad \text{if } u_2\leq x<b. \tag{14}$$

For any distribution defined over $(-\infty,\infty)$ inequalities (10), (12), and (14) hold, respectively, for $x<z_1$, $z_1<x<z_2$, $z_2<x$.

However, the ordering of $x$ in relation to $z_1$, $z_2$ is equivalent to the following. Let $g(x)=x^3-m_3x-1$, then

$$x>0,\quad g(x)>0 \qquad \text{if, and only if, } z_2<x. \tag{15}$$

$$x<0,\quad g(x)>0 \qquad \text{if, and only if, } z_1>x \tag{16}$$

$$g(x)<0 \qquad \text{if, and only if, } z_1<x<z_2. \tag{17}$$

Using (15) to (17), the applications of the Tchebycheff-Markoff inequalities for the case where $F(y)$ is defined over $(-\infty,\infty)$ are made particularly easy.

## 3. Application of the Tchebycheff-Markoff Inequalities

Let $F(y)$ be a distribution function whose first four moments coincide with those of the standard normal distribution, i. e., $m_0=1$, $m_1=0$, $m_2=1$, $m_3=0$, $m_4=3$. The Tchebycheff-Markoff inequalities will be used to find bounds for $F(x)$ when $x=2$, 3.

*Bounds using two moments:* Since $x>0$, inequality (5) is applicable, and we have

$$.8000\leq F(2)\leq 1$$

$$.9000\leq F(3)\leq 1.$$

*Bounds using four moments:* Since $x>0$, $g(2)>0$, $g(3)>0$, inequality (14) is applicable. Substituting the appropriate values, we have

$$1-\frac{2}{2(1+x^2)+(x^3-1)^2}\leq F(x)\leq 1 \text{ for } x=2,3$$

therefore,

$$.8947\leq F(2)\leq 1$$

$$.9777\leq F(3)\leq 1.$$

Note that there are no inequalities applicable using only moments to order three.

## 4. Appendix

Statements and proofs of the Tchebycheff-Markoff inequalities can be found in Shohat and Tamarkin [4], Uspensky [8], and Royden [3]. This section contains a statement of the Tchebycheff-Markoff inequalities as the above sources do not give the theorem in full generality, and it is not readily available in the literature.

Before stating the theorem it will be convenient to define the following: Let $T_n(y)$, $U_n(y)$, $V_n(y)$, $W_n(y)$ be polynomials of degree $n$ defined by

$$\int_a^b T_n(y)\theta_{n-1}(y)dF(y)=0 \tag{18}$$

$$\int_a^b U_n(y)\theta_{n-1}(y)(y-a)dF(y)=0 \tag{19}$$

$$\int_a^b V_n(y)\theta_{n-1}(y)(b-y)dF(y)=0 \tag{20}$$

$$\int_a^b W_n(y)\theta_{n-1}(y)(y-a)(b-y)dF(y)=0, \tag{21}$$

where $\theta_{n-1}(y)$ is any polynomial of degree $\leq n-1$, and the coefficient for $y^n$ in $T_n(y)$, $U_n(y)$ $V_n(y)$, $W_n(y)$ is unity.

*Tchebycheff-Markoff Inequalities:* Let $F(y)$ be any distribution function on $[a,b]$ with moments $m_0, m_1, \ldots, m_k$

$$m_j=\int_a^b y^j dF(y) \qquad (j=0,1,\ldots,k),$$

and let $x$ be a given number $(a<x<b)$, then

$$\sum_{y_i<x}\frac{p(y_i)}{q'(y_i)}\leq F(x)\leq\sum_{y_i<x}\frac{p(y_i)}{q'(y_i)}+\frac{p(x)}{q'(x)},$$

where

$$p(z)=\int_a^b\frac{q(z)-q(y)}{z-y}\,dF(y),$$

and $y_1<y_2<\ldots<x<\ldots$ are the zeros of the polynomial $q(y)$ of degree $r$ defined by

$$q(y)=(y-x)w(y) \qquad \text{if } k=2n,\ U_n(x)V_n(x)>0, \tag{22}$$

$$q(y)=(y-b)(y-a)(y-x)w(y) \qquad \text{if } k=2n,\ U_n(x)V_n(x)<0, \tag{23}$$

$$q(y)=(y-a)(y-x)w(y) \qquad \text{if } k=2n-1,\ T_n(x)W_{n-1}(x)>0, \tag{24}$$

$$q(y)=(y-b)(y-x)w(y) \qquad \text{if } k=2n-1,\ T_n(x)W_{n-1}(x)<0, \tag{25}$$

where $r=n+2$ for eq (23), $r=n+1$ for (22), (24), (25), and $w(y)$ is determined by

$$\int_a^b q(y)y^i dF(y)=0 \qquad \begin{matrix} i=0,1,\ldots,n-1 \text{ for (22)} \\ i=0,1,\ldots,n-2 \text{ for (23), (24), (25).}\end{matrix}$$

COROLLARY: *For eq (22) the inequalities hold for any distribution over $(-\infty,\infty)$ with moments $m_0, m_1, \ldots, m_{2n}$. The inequalities for eq (24) hold for any distribution over $[a,\infty)$ with moments $m_0, m_1, \ldots, m_{2n-1}$. The inequalities for eq (25) hold for any distribution over $(-\infty, b]$ with moments $m_0, m_1, \ldots, m_{2n-1}$.*

I wish to express my thanks to Professor Wassily Hoeffding, University of North Carolina, for his invaluable guidance during the preparation of this work.

## 5. References

[1] A. Markoff, Démonstration de certaines inégalitiés de M. Tchebycheff, Math. Ann. **XXIV,** 172–180 (1884).
[2] C. Possé, Sur quelques applications des fractions continues algebriques (Academie Imperiale des Sciences, St. Petersburg, 1886).
[3] H. L. Royden, Bounds on a distribution function when its first $n$ moments are given, Ann. Math. Stat. **24,** 361–376 (1953).
[4] J. A. Shohat and J. D. Tamarkin, The problems of moments (Am. Math. Soc., New York, 1943).
[5] T. J. Stieltjes, Sur l'évaluation approchée des intégrales, Compt. rend **XCVII,** 740–742, 798–799 (1883).
[6] T. J. Stieltjes, Recherches sur les fractions continues, Ann. faculté sciences Toulouse **VIII,** 1–22 (1894); **IX,** 45–47 (1895).
[7] P. Tchebycheff, Sur les valeurs limites des intégrales, J. de Math. [2] **XIX,** 157–160 (1874).
[8] J. V. Uspensky, Introduction to mathematical probability (McGraw-Hill Book Co., New York, N. Y., 1937).
[9] M. Zelen, Bounds on a distribution function which are functions of moments, unpublished masters thesis (University of North Carolina Library, 1951).

Washington, November 20, 1953.

Journal of Research of the National Bureau of Standards Vol. 53, No. 6, December 1954 Research Paper 2557

# Aerological Sounding Balloons[1]

Gordon M. Martin, John Mandel, and Robert D. Stiehler

A low-temperature patch test for sounding balloons is described. In this test a circular piece is cut out of the rubber film, clamped around its circumference, and inflated until it bursts. Equations applying to the patch test and to the flight of sounding balloons are developed. The important properties in determining the flight elevation are found to be the flaccid length of the balloon and the elongation of the rubber film. The effective elongation is defined as the average elongation of the entire balloon film at the pressure at which the weakest part of the balloon will fail. A method of estimating this effective elongation from patch test data is given. Correlation was found between patch-test data and night-flight elevations. On the basis of flights made with thermistors both inside and outside the balloon, the temperature of the balloon film at burst is estimated to be 0 to 4 Celsius degrees colder than the surrounding air at night and 20 to 30 Celsius degrees warmer than the surrounding air in the daytime.

## 1. Introduction

Sounding balloons are used on routine weather flights to carry radiosondes into the stratosphere. In the United States the balloons are usually made of a neoprene film with an unstretched thickness of about 0.003 in. and weigh 500 to 600 g. They are inflated with helium or hydrogen to a specified lift and, when released, rise at a rate of about 0.3 km/min to elevations of 15 to 30 km before bursting. At these altitudes the temperature may be as low as −70° C and ozone, ultraviolet radiation, and cosmic radiations are much more prevalent than at the surface of the earth. At the request of the Department of the Navy, Bureau of Aeronautics, the National Bureau of Standards has been investigating the factors involved in the flight of sounding balloons. This paper outlines some of the results obtained.

Laboratory tests have been made on special balloons and on balloons from regular production lots. Other balloons from the same lots have been flown by the Weather Bureau. Some tests that have been made are: (1) conventional tensile tests of dumbbell specimens at room temperature and at −40° C, (2) balloon inflation tests, using air at room temperature, and (3) brittleness tests at −60° C. The results of these tests did not correlate with the flight elevations attained in service. Some of the factors contributing to this lack of correlation may be: (1) tensile tests on dumbbell specimens of thin films are extremely sensitive to small variations in the character and condition of the cutting die, (2) tests of the film at room temperature and even at −40° C are not indicative of the properties at the lower temperatures encountered in service, (3) brittleness tests involve the sudden bending of the specimen at low temperature, whereas in flight the film is stretched gradually at the same time it is being cooled, and (4) conventional tensile tests involve stretching the rubber in one direction, whereas during flight the film experiences a two-dimensional stretching. These considerations indicated the advisability of using a patch test at a temperature approximating that encountered in flight. Most of recent work at NBS has been concerned with such a test.

[1] This work was financed by the Department of Navy, Bureau of Aeronautics.

## 2. Patch Test

In the patch test a circular piece of the film, or patch, is clamped around its circumference and inflated until it bursts. The film passes through a series of forms approximated by a flat surface, a hemisphere, a sphere with a section cut off at the bottom, and finally an oblate spheroid. Diagrams of these forms are given by Treloar.[2] The greatest stretching takes place near the center of the patch, and the break usually occurs in this region. In this work the inflation is conducted inside a cold box maintained at the desired temperature by a detachable servo-unit that operates with dry ice. The patch is inflated with superdry nitrogen in order to introduce as little water vapor as possible into the cold chamber. The compressed nitrogen passes from its container through a two-stage pressure regulator, a needle valve, a flowmeter, and then into a large copper tube inside the cold box, where it cools down before coming into contact with the patch. Figure 1 shows the equipment, and figure 2 shows a patch during inflation.

The quantities measured are the differential pressure across the patch, the distance between bench marks on its surface, and the maximum dimension of the patch. A circle, 1 cm in diameter, is marked at the middle of the patch. During inflation the diameter of this circle is measured by a flexible scale that rests lightly on the patch and follows the shape of its upper surface. The scale is observed through a removable thermopane window in the top of the cold box. This measurement in centimeters is equal to the elongation[3] of the region near the center of the patch. The differential pressure across the patch is measured by a mercury manometer or by a bellows sensitive to pressure that is connected to an electric-

[2] L. R. G. Treloar, Strains in an inflated rubber shell and the mechanism of bursting, Trans. Inst. Rubber Ind. [6] **19**, 201 (London, April 1944).

[3] In this paper, elongation is defined as the ratio of stretched length to unstretched length and not as the percentage increase in length.

FIGURE 1. *Patch test equipment.*

The dry-ice chamber is on the left; the cold box containing the patch is on the right.

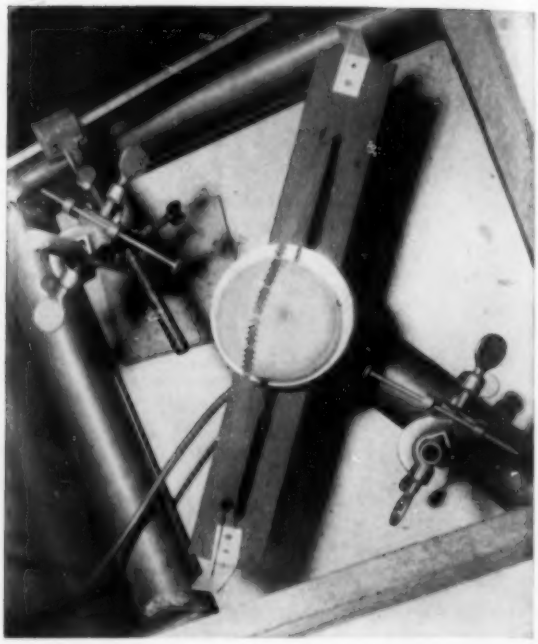

FIGURE 2. *Patch during inflation.*

The flexible scale for measuring elongation is resting on the patch, but the 1-cm circle is not visible in the photograph. The pistons for obtaining the major diameter and the large copper tube for cooling the inflating gas may also be seen.

measuring system. The major diameter at burst is measured by means of two freely moving pistons with flat heads, which are pushed outward by the expanding patch. The distance between the pistons is measured with a steel scale after the patch has burst.

Initial patch tests were made at several fixed temperatures. It was found that the ultimate elongation of the neoprene film decreased, and the stiffness and tensile strength increased as the temperature was lowered. As the temperature coefficients were different for different films, the properties at room temperature were not a good indication of the low-temperature characteristics of the rubber films.

The method finally developed for the patch tests involves a prestretching at a temperature higher than that at burst. This corresponds more closely to the way the film is stretched in flight. The patch inflation is started at −40° C. The volume rate of inflation is held constant throughout the test. When the 1-cm-diameter circle reaches a diameter of 2.5 cm, the surrounding air is cooled until the temperature is reduced to −60° C. The temperature is held at −60° C until the patch bursts. Five to 10 min are required to cool the air from −40° to −60° C, and the entire test lasts 15 to 20 min. This test is referred to in this paper as the −60° C patch test.

## 3. Equations Applicable to Patch Test

Approximate relations giving the tensile strength and elongation in a patch test have been derived by C. F. Flint and W. J. S. Naunton.[4] Their equations are

$$S_B = \frac{1.35PR_e^2}{at_0}, \tag{1}$$

$$E_B = \frac{2.60R_e}{a}. \tag{2}$$

$S_B$ is the tensile stress at burst, based on the original cross section; $P$ is the differential pressure across the patch; $R_e$ is the equatorial radius of the patch at burst; $a$ is the radius of the circular aperture, that is, half the inside diameter of the ring used to clamp the patch; $t_0$ is the thickness of the unstretched film; and $E_B$ is the ultimate elongation or the ratio of the final to the initial length of a line drawn on the film.

Solving (2) for $R_e$ and substituting in (1) gives

$$S_B = \frac{PE_B^2 a}{5t_0}. \tag{3}$$

[4] C. F. Flint and W. J. S. Naunton, Physical testing of latex films, Trans. Inst. Rubber Ind. **13**, 367 (London, 1936-37).

In the patch test used in this work, $a$ is 1.25 in. Substituting this value into (2) and (3) gives

$$E_B = 2.08R_e = 1.04D_e, \tag{2a}$$

with $R_e$ and $D_e$ in inches.

$D_e$ is the equatorial diameter of the patch at burst.

$$S_B = \frac{PE_B^2}{4t_0}, \tag{3a}$$

with $t_0$ in inches. $S_B$ is in the same units as $P$.

As the diameter of the patch at burst was measured directly with pistons and the elongation was determined from measurements on a circle, 1 cm in diameter stamped in the middle of the patch, it was possible to determine the validity of eq (2a). According to this equation, $E_B/D_e = C$, where $C$ is 1.04 in., with $D_e$ in inches. Experimental values of $C$ are: 0.97, 1.01, 0.93, 0.96, 0.98, 1.00, 1.00, 1.04, 1.00, and 1.08. Each of these 10 values represents the average for a number of patches from a particular balloon. The differences between these values and 1.04 may be the result of several causes. When the rubber film is near the glass-transition temperature, part of the film may freeze and the remainder continue to elongate, thus changing the value of $C$. Variations in the area of rubber exposed, because of wrinkles in the film or slippage in the clamp, would also affect the value of $C$. The value of $C$ is probably slightly different at different temperatures and for different compounds.

A relation between the bursting pressure, $P$, in a patch test and the differential bursting pressure, $P_d$, across the surface of a uniform spherical balloon made of the same material is given in eq (10) below and can be derived as follows:

Imagine cutting the balloon along a great circle just before it bursts. The tensile strength, based on the final cross-sectional area, $S'_B$, may be found by equating the forces pushing the halves apart to the tensile forces holding them together.

$$\pi R_B^2 P_d = 2\pi R_B t_B S'_B \tag{4}$$

or

$$S'_B = \frac{R_B P_d}{2t_B}, \tag{4a}$$

where $R_B$ is the radius of the balloon at burst, and $t_B$ is the thickness of the rubber film at burst.

Now, since $R_B = E_B R_0 = (E_B D_0)/2$, where $R_0$ is the unstretched, or flaccid, radius of the balloon, and $D_0$ is the flaccid diameter,

$$S'_B = \frac{R_0 E_B P_d}{2t_B} = \frac{D_0 E_B P_d}{4t_B}. \tag{5}$$

The tensile strength based on the original cross-sectional area, $S_B$, is found by equating the forces pushing the halves of the balloon apart to the tensile forces holding them together, expressed in terms of the unstretched cross-sectional area.

$$\pi R_B^2 P_d = 2\pi R_0 t_0 S_B \tag{6}$$

$$S_B = \frac{R_B^2 P_d}{2R_0 t_0} \tag{6a}$$

Letting $R_B = E_B R_0 = (E_B D_0)/2$ gives

$$S_B = \frac{R_0 E_B^2 P_d}{2t_0} = \frac{D_0 E_B^2 P_d}{4t_0} \tag{7}$$

Combining eq (4) and (6) gives the relation between the tensile strengths based on the final and on the original cross-sectional areas.

$$S'_B = \frac{R_0 t_0 S_B}{R_B t_B} = \frac{t_0 S_B}{t_B E_B}. \tag{8}$$

Assuming a constant volume of rubber (or constant density),

$$4\pi R_B^2 t_B = 4\pi R_0^2 t_0 \tag{9}$$

or

$$\frac{t_0}{t_B} = \frac{R_B^2}{R_0^2} = E_B^2. \tag{9a}$$

Using eq (9a), eq (5) and (8) become

$$S'_B = \frac{D_0 E_B^3 P_d}{4t_0} \tag{5a}$$

$$S'_B = S_B E_B. \tag{8a}$$

Now we assume that the tensile strength, ultimate elongation, and original thickness of the film are the same for the patch and the balloon. Equating the values of tensile strength given by eq (3) and (7) gives

$$\frac{P}{P_d} = \frac{5D_0}{4a}. \tag{10}$$

As $a$ is 1.25 in. in these tests,

$$\frac{P}{P_d} = D_0, \tag{10a}$$

with $D_0$ in inches.

It is not always convenient to measure $D_0$ in the laboratory, and the flaccid length, $L_0$, is often measured instead. This is the length of the uninflated envelope exclusive of the neck, when the balloon is suspended vertically by the neck. It is assumed that

$$D_0 = \frac{2L_0}{\pi}. \tag{11}$$

The Dewey & Almy Chemical Co.[5] has been inflating small balloons having an unstretched diameter of 4 in. at a temperature of −75° F. A typical bursting pressure from their data is 11 in. of water.

[5] Dewey & Almy Chemical Co. (private communication).

When these values are substituted in eq (10a), the bursting pressure of a patch cut from a similar film is found to be 44 in. of water. The average bursting pressures of patches from four production Dewey & Almy sounding balloons tested at −76° F (−60° C) are 47, 54, 65, and 83 in. of water. Of course, these rubber films may differ from those of the small balloons tested at the factory.

Additional tests of eq (10a) have been made by inflating pilot balloons with air at room temperature and making patch tests at room temperature on other balloons from the same lots. For example, the bursting pressure of a balloon was 0.92 in. of water, and the patch-test bursting pressure was 15.7 in. of water. By eq (10a) the unstretched diameter of the balloon is calculated to be 17 in. The balloon was not a perfect sphere when inflated just enough to remove the wrinkles, but the average horizontal diameter was measured as 16 in. The diameter calculated from the measured volume of the balloon, using the formula for a sphere, was 16.6 in.

In all these cases the bursting pressure of the patches is slightly higher than the value calculated by using the bursting pressure and flaccid diameter of the balloon in eq (10a). This difference can be attributed to the fact that the bursting pressure of the balloon does not correspond to the average bursting pressure of the patches cut from it, but to that of the weakest patch. The method of estimating the minimum bursting pressure of all the patches from the balloon is discussed in section 5.

## 4. Flight Equation

When a sounding balloon ascends into the atmosphere, it expands as the atmospheric pressure decreases until it finally bursts. The atmospheric pressure at burst, $P_a$, which determines the bursting elevation, is given by the equation

$$P_a=P_B-P_d, \tag{12}$$

where $P_B$ is the absolute pressure inside the balloon, and $P_d$ is the differential pressure across the surface of the balloon at burst.

$P_B$ may be found from the ideal gas law, because helium and hydrogen behave almost like perfect gases under these conditions and as there is not enough time for very much gas to escape through the balloon film,

$$P_B=P_i\frac{T_B}{T_i}\frac{R_i^3}{R_B^3}, \tag{13}$$

where $P$ is the absolute pressure inside the balloon, $T$ is the absolute temperature of the gas, and $R$ is the radius of the balloon. The subscript $i$ refers to the initial conditions at launching, and the subscript $B$ refers to conditions at burst.

Letting $R_B=R_0E_B$ and $R_0=\frac{L_0}{\pi}$ in eq (13) gives

$$P_B=P_i\frac{T_B}{T_i}\frac{R_i^3\pi^3}{E_B^3L_0^3}. \tag{13a}$$

The value of $R_i$ depends upon conditions at launching. Usually the balloon is inflated until it will just lift a specified weight. Assuming that the ideal gas law holds, the relation is

$$R_i^3=\frac{3V_i}{4\pi}=\frac{3}{4\pi}\cdot\frac{RT_i(F+W)}{P_i(M_a-M_g)}, \tag{14}$$

where $V_i$ is the volume of the balloon at launching, $R$ is the gas constant, $F$ is the lift, $W$ is the weight of the balloon, $M_a$ is the weight of a molal volume of air, and $M_g$ is the weight of a molal volume of inflating gas. Substituting this value for $R_i$ into eq (13a) gives

$$P_B=\frac{3\pi^2R(F+W)T_B}{4(M_a-M_g)E_B^3L_0^3}. \tag{15}$$

$P_d$, the differential bursting pressure across the surface of the balloon, may be found from eq (10a) and (11),

$$P_d=\frac{\pi P}{2L_0}, \tag{16}$$

where $P$ is the bursting pressure from the patch test and $L_0$ is the flaccid length of the balloon in inches.

Another relation for $P_d$ may be obtained by expressing the thickness of the rubber film in terms of other constants of the balloon and by using $S'_B$, the tensile strength on the final cross-sectional area, instead of $P$.

$$t_0=\frac{W}{\pi D_0^2\sigma}, \tag{17}$$

where $\sigma$ is the density of the rubber.

Solving for $P_d$ in eq (5a) and substituting for $t_0$ from eq (17), we have

$$P_d=\frac{4WS'_B}{\pi\sigma D_0^3E_B^3}=\frac{\pi^2WS'_B}{2\sigma L_0^3E_B^3}. \tag{18}$$

The equation used for predicting the performance of production sounding balloons is obtained by substituting the expressions for $P_B$ and $P_d$ from eq (15) and (16) into eq (12) and using appropriate values for some of the factors. Assume that the balloon is inflated to a lift of 3,000 g and that the temperature at burst is 213° K. The gas constant is 5,074 in.$^3$ millibars per gram mole deg K. $M_a$ is 28.96 g, and if the gas used is helium, $M_g$ is 4.00 g.

$$P_a=\frac{320{,}000(3{,}000+W)}{E_B^3L_0^3}-\frac{1.57P}{L_0}, \tag{19}$$

where $P_a$ is the atmospheric pressure at burst in millibars, $W$ is the weight of the balloon in grams, $E_B$ is the elongation at burst, $L_0$ is the flaccid length of the balloon in inches, and $P$ is the bursting pressure from the patch test in millibars.

A form of the flight equation that is more convenient for some purposes is obtained by substituting the values for $P_B$ and $P_d$ from eq (15) and (18) into

eq (12).

$$P_a=\frac{A(F+W)T_B-BWS'_B}{E'_BL_0^3}, \tag{20}$$

where

$$A=\frac{3\pi^2R}{4(M_a-M_g)} \quad \text{and} \quad B=\frac{\pi^2}{2\sigma}.$$

It is possible to obtain an approximate equation that gives the flight elevation directly. The relation between elevation and pressure for the standard atmosphere [6] in the region where the balloons burst is

$$h=89.2-14.6 \log P_a, \tag{21}$$

where $h$ is the elevation in kilometers, and $\log P_a$ is the logarithm to the base 10 of the atmospheric pressure in dynes per square centimeter.

Substituting $P_a$ from eq (20) into eq (21), we have

$$h=89.2+43.8 \log(E_BL_0)- 14.6 \log[A(F+W)T_B-BWS'_B]. \tag{22}$$

A study of this equation shows that changes in $E_B$ or $L_0$ will have a pronounced influence on the bursting elevation and that proportionate changes in the balloon weight, temperature at burst, or tensile strength will have a much smaller effect. We may substitute typical values for the less important quantities and obtain an approximate equation in a simpler form. Let $F=3{,}000$ g, $T_B=213°$ K, $W=600$ g, $S'_B=7.63\times10^8$ dynes/cm², $R=8.314\times10^7$ ergs/mole deg K, $\sigma=1.25$ g/cm³, $M_a=28.96$ g, and $M_g=4.00$ g. Then $A=2.47\times10^7$ ergs/g deg K, and $B=3.95$ cm³/g. Equation (22) becomes

$$h=43.8 \log(E_BL_0)-104.0, \tag{23}$$

with $h$ in kilometers and $L_0$ in centimeters or

$$h=43.8 \log(E_BL_0)-86.3, \tag{24}$$

with $h$ in kilometers and $L_0$ in inches.

Both eq (19) and (24) give values that are in reasonable agreement with flight results. Equation (24) indicates that the bursting elevation is linearly related to the logarithm of the product of elongation and flaccid length. A method of determining the effective elongation and minimum patch-bursting pressure used in these equations is given in section 5.

## 5. Effective Elongation

In predicting the flight performance of a group of similar balloons, the elongation and the bursting pressure determined from patch tests on some of the balloons may be used in eq (19), together with the average weight and flaccid length of the balloons to be flown. In a perfectly uniform spherical balloon a test of one patch would give the ultimate elongation and the bursting pressure characteristic of the entire balloon. Actually, there is a good deal of variation in strength (due in part to variation in thickness) over the surface of a balloon. When the weakest section fails most parts of the balloon will be considerably below their ultimate elongations. Consequently, the balloon will burst at a smaller volume and a lower elevation than would be anticipated if the average ultimate elongation and the average bursting pressure of the film were used. How much lower the altitude will be depends on the amount of variation in the stress-strain characteristics of the rubber.

The effective elongation, which is used in determining the bursting volume of the balloon, may be defined as the average elongation of the entire balloon film at the differential pressure at which the weakest part will fail. The minimum bursting pressure and the effective elongation are estimated from patch-test data. A balloon may be equivalent to as many as 1,500 patches, but only a few of them are tested. The standard deviation in bursting pressure is found for the patches tested, and a multiple of this standard deviation is subtracted from the average bursting pressure to get the estimated minimum bursting pressure. In practice, it has been found that an appropriate value for this multiple is 2. Thus, the patch bursting pressure used in the flight equation is two standard deviations below the average bursting pressure of the patches tested.

For each patch tested a plot can be made of the differential pressure corresponding to various elongations. The plots for different patches from the same balloon are usually similar. Figure 3 is an example

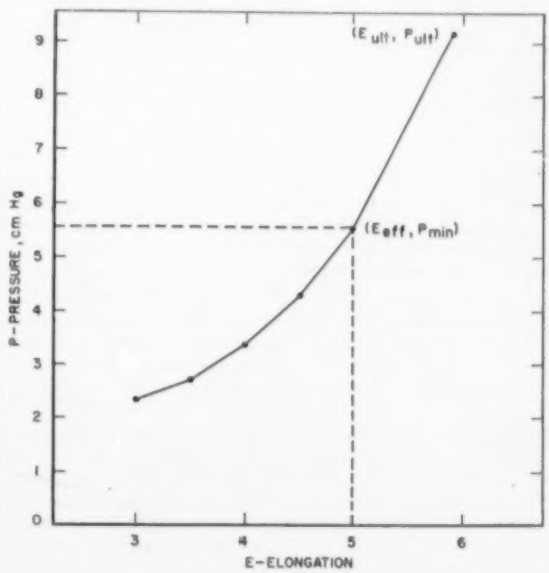


FIGURE 3. *Differential pressure versus elongation in patch tests at —60° C.*

Each point is an average for 18 patches from 1 group of balloons.

[6] Calvin N. Warfield, A tentative standard atmosphere, NACA Tech. Note 1200.

of this relationship obtained by averaging a number of patches. The curve ends at a point representing the average differential pressure and elongation at failure, that is, the average bursting pressure and the average ultimate elongation of the patches. The horizontal dashed line represents a pressure two standard deviations below the average bursting pressure. This is the estimated minimum bursting pressure in the patch test, which is related by eq (10a) to the differential pressure at which the weakest region of the balloon will fail. At that particular moment the average elongation of the balloon should have a value that can be approximated by taking the abscissa in figure 3 corresponding to the minimum pressure. The value thus obtained is the estimated effective elongation and may be used for $E_B$ in the flight equation.

An estimate was obtained for the precision of the bursting elevations predicted from the results of patch tests at $-60°$ C on the four groups used in the special experiment described in section 6. For balloons from the same group, the standard deviation of predicted elevations was found to be 2.7 km, based on tests of three patches per balloon. The standard deviation in actual night flight elevations of balloons from the same group was 2.1 km. Thus, provided that the same number of balloons are tested as are flown, the reproducibilities of laboratory and flight tests are about the same. However, the accuracy of the laboratory values may not be as good because factors other than those included in eq (19) or (20) may cause premature failure of the balloon.

Actual flight performance may differ from that predicted on the basis of the patch test because of the action of ozone at high elevations, the concentration of stresses in certain parts of the film, such as the region where the neck joins the body of the balloon, the different rate of stretching and the different temperatures experienced in flight, or possibly because of other factors that are not yet understood. Also the distribution of patch-bursting pressures may be different for different balloons, which may cause errors in the estimation of the minimum bursting pressures and effective elongations and reduce the accuracy of the predicted elevations. Nevertheless, this method gives results that show significant correlation with flight elevations.

As mentioned before, the method outlined for obtaining the minimum patch-bursting pressure for a balloon by subtracting two standard deviations from the average value is essentially an empirical one. Theoretically, statistical methods can be used to estimate the minimum pressure. This would require certain assumptions concerning the distribution function of patch-bursting pressures so that the theory of extreme values could be applied. It would then be desirable to obtain a random sample of patches from the balloon. In the work reported here the selection of patches was not entirely random because the balloon was cut into sections and one or more patches taken from each section. The information so far obtained from the investigation is not sufficient to make use of this theoretical approach.

## 6. Flight Experiments

In section 4 it is shown that there should be approximately a linear relationship between the flight elevation and the logarithm of the product of elongation and flaccid length. The relation between this logarithm and flight elevations was studied on production lots of balloons flown by the Weather Bureau in regular service. The day flights of samples from 30 lots made by three different manufacturers did not discriminate between lots that had differences as judged by both night flights and laboratory tests. Data from the $-60°$ C patch test (described in section 2) showed some correlation with the night flights of samples from 18 production lots. These data are summarized in table 1. Using the ultimate

TABLE 1. *Results of laboratory tests and night flights of production lots of balloons*

| Lot number | Number of flights | Median flight elevation | Average flaccid length, $L_0$ | Ultimate elongation, $E_{ult.}$ | Log ($L_0 \times E_{ult.}$) | Effective elongation, $E_{eff.}$ | Log ($L_0 \times E_{eff.}$) |
|---|---|---|---|---|---|---|---|
| | | *km* | *in* | | | | |
| 1 | 3 | 24.91 | 75.7 | 4.97 | 2.575 | 4.58 | 2.540 |
| 2 | 3 | 25.41 | 75.6 | 4.96 | 2.574 | 4.34 | 2.516 |
| 4 | 6 | 22.44 | 73.8 | 5.09 | 2.575 | 4.35 | 2.506 |
| 5 | 5 | 16.63 | 74.8 | 4.91 | 2.565 | 3.48 | 2.415 |
| 25 | 1 | 19.84 | 77.0 | 5.60 | 2.635 | 3.93 | 2.481 |
| 26 | 2 | 17.69 | 73.5 | 5.57 | 2.612 | 3.84 | 2.451 |
| 27 | 2 | 20.18 | 74.0 | 5.44 | 2.605 | 4.72 | 2.543 |
| 28 | 2 | 19.00 | 76.5 | 5.60 | 2.627 | 4.78 | 2.563 |
| 29 | 2 | 20.19 | 79.0 | 5.28 | 2.620 | 4.23 | 2.524 |
| 30 | 2 | 21.20 | 73.5 | 5.54 | 2.610 | 5.15 | 2.578 |
| 31 | 2 | 19.80 | 72.5 | 5.52 | 2.602 | 4.95 | 2.555 |
| 33 | 2 | 24.76 | 77.0 | 5.50 | 2.627 | 5.22 | 2.604 |
| 34 | 2 | 18.22 | 79.0 | 5.40 | 2.630 | 4.82 | 2.581 |
| 35 | 1 | 24.70 | 82.0 | 5.29 | 2.637 | 4.52 | 2.569 |
| 36 | 2 | 23.58 | 80.0 | 5.27 | 2.625 | 4.23 | 2.529 |
| 6N | 10 | 25.22 | 76.3 | 6.13 | 2.670 | 5.33 | 2.609 |
| 7N | 10 | 26.90 | 77.3 | 5.98 | 2.665 | 5.19 | 2.603 |
| 8N | 21 | 25.03 | 72.0 | 5.92 | 2.630 | 5.43 | 2.592 |

elongation, the correlation coefficient is 0.57; with the effective elongation, it is 0.77. The probability of obtaining a value as large or larger than 0.57 by chance alone is about 2 percent; the corresponding probability for 0.77 is considerably less than 0.1 percent. The correlation coefficients were weighted to take account of the number of flights made for each lot. Only five patches from one balloon were tested for most lots. Considering the small number of flights made and the small number of patches tested for most samples, the correlation was as good as would be expected. As the data were not obtained from a systematically designed series of experiments, few conclusions regarding the factors affecting the performance of sounding balloons can be drawn from them.

In order to make a more conclusive study of these factors, a special experiment was designed. This experiment involved 120 balloons divided into four groups of 30 balloons each. These groups consisted of regular and post-plasticized (plasticized after vulcanization), balloons from each of two manu-

facturers. The weights and flaccid lengths of the balloons were held fairly constant within each of the four groups. The 30 balloons within each group were used as follows: 12 for day flights, 12 for night flights, and 6 for laboratory tests. The allocation of balloons for flight and laboratory test was done at random. The order in which the balloons were tested in the laboratory was also random. For the laboratory tests, six patches were cut from each balloon. Three of the patches were tested at a constant temperature of −40° C, and the other three, by the procedure given in section 2, with a temperature of −60° C at burst.

Table 2 shows the design of the flight tests for the four groups of balloons at four Weather Bureau stations. On any one day at any one station two balloons from the same group were flown; one in the daytime and one at night. Table 3 lists the average bursting elevations for balloons of each group flown at each station. The results for day and night flights are given separately. In several cases the averages reported are for two flights for a given group at a given station instead of for the three indicated by the schedule of table 2, either because of instrument failure or premature failure of the balloon. Such results were eliminated because they do not reflect the inherent characteristics of the rubber film. An analysis of variance for the data from the individual flights reveals that:

1. The day-flight results do not distinguish conclusively between the four groups of balloons. The ranking changes markedly from station to station.

2. The night-flight results are more consistent for balloons of a given group, whether the balloons are flown at the same station or at different stations.

Tables 4 and 5 give the average differential bursting pressures and ultimate elongations for the six balloons from each group in the −40° and −60° C patch tests. The average effective elongations for the balloons in each group are given in table 6. Figures 4 and 5 show plots of the average flight elevations against the logarithms of the products of elongation and flaccid length. The day flights are compared with the results from the −40° C patch test, and the night flights are compared with the results from the −60° C patch test. In figure 4 the effective elongations are used and in figure 5 the ultimate elongations. When the ultimate elongations are used the correlation is rather poor. However, if the effective elongations are used, the correlation is excellent for night flights. It is seen that the points for the day flights, using effective elongations, are not very far from the line determined by the night flights. The greater scatter of the points for day flights is not surprising because of the uncertainty of the temperature of the balloon film (discussed in section 7) and the erratic behavior of the day flights. The small range in average day-flight elevations and effective elongations of the four groups and the large uncertainties in day-flight values result in low sensitivities for the day flights and −40° C patch tests, which are not sufficient to obtain significant differences between the four groups of balloons in this experiment.

TABLE 2. *Allocation of balloons to flight stations*

W, St. Cloud, Minn.; X, Bismarck, N. Dak.; Y, Rapid City, S. Dak.; Z, International Falls, Minn.

| Day of flight | Group | | | |
|---|---|---|---|---|
| | A | B | C | D |
| 1 | W | X | Y | Z |
| 2 | X | W | Z | Y |
| 3 | Y | Z | W | X |
| 4 | Z | Y | X | W |
| 5 | X | W | Z | Y |
| 6 | W | X | Y | Z |
| 7 | Z | Y | X | W |
| 8 | Y | Z | W | X |
| 9 | Y | Z | W | X |
| 10 | Z | Y | X | W |
| 11 | W | X | Y | Z |
| 12 | X | W | Z | Y |

TABLE 3. *Flight results*

Average bursting elevations, in kilometers

| Flight station | Group | | | | | | | |
|---|---|---|---|---|---|---|---|---|
| | A | | B | | C | | D | |
| | Day | Night | Day | Night | Day | Night | Day | Night |
| W | 22.64 | 23.54 | 25.21 | 18.36 | 21.79 | 24.15 | 27.82 | 20.16 |
| X | 21.00 | 23.35 | 25.26 | 17.64 | 24.95 | 23.68 | 22.43 | 18.02 |
| Y | 24.08 | 22.55 | 17.09 | 17.75 | 22.35 | 20.71 | 22.64 | 18.97 |
| Z | 19.38 | 25.66 | 23.95 | 19.55 | 24.50 | 22.97 | 22.84 | 19.80 |
| Average | 21.78 | 23.78 | 22.88 | 18.33 | 23.40 | 22.88 | 23.94 | 19.24 |

TABLE 4. *Laboratory results for patch tests at −40° C*

| Balloon number | Group | | | | | | | |
|---|---|---|---|---|---|---|---|---|
| | A | | B | | C | | D | |
| | Bursting pressure | Ultimate elongation | Bursting pressure | Ultimate elongation | Bursting pressure | Ultimate elongation | Bursting pressure | Ultimate elongation |
| | cm Hg | | cm Hg | | cm Hg | | cm Hg | |
| 1 | 6.4 | 6.20 | 12.7 | 5.60 | 8.9 | 5.40 | 11.1 | 5.23 |
| 2 | 7.1 | 5.95 | 13.7 | 5.53 | 8.3 | 5.40 | 10.5 | 5.23 |
| 3 | 8.4 | 6.07 | 9.5 | 5.60 | 8.4 | 5.53 | 10.4 | 5.28 |
| 4 | 10.3 | 5.77 | 14.1 | 5.77 | 8.5 | 5.27 | 10.4 | 5.22 |
| 5 | 12.1 | 5.93 | 14.4 | 5.67 | 8.9 | 5.40 | 10.7 | 5.22 |
| 6 | 10.8 | 5.73 | 14.8 | 5.83 | 8.9 | 5.27 | 11.3 | 5.30 |
| Average | 9.2 | 5.94 | 13.2 | 5.67 | 8.7 | 5.38 | 10.7 | 5.25 |

TABLE 5. *Laboratory results for patch tests at −60° C*

| Balloon number | Group | | | | | | | |
|---|---|---|---|---|---|---|---|---|
| | A | | B | | C | | D | |
| | Bursting pressure | Ultimate elongation | Bursting pressure | Ultimate elongation | Bursting pressure | Ultimate elongation | Bursting pressure | Ultimate elongation |
| | cm Hg | | cm Hg | | cm Hg | | cm Hg | |
| 1 | 12.0 | 6.05 | 19.0 | 5.90 | 13.5 | 5.00 | 15.9 | 4.75 |
| 2 | 8.9 | 6.05 | 15.9 | 5.47 | 13.9 | 4.97 | 14.7 | 4.67 |
| 3 | 14.0 | 5.55 | 16.9 | 5.68 | 11.8 | 4.93 | 14.3 | 4.77 |
| 4 | 12.7 | 5.92 | 15.5 | 5.27 | 12.7 | 4.82 | 15.5 | 4.83 |
| 5 | 13.2 | 5.48 | 16.8 | 5.60 | 13.9 | 4.73 | 15.9 | 4.83 |
| 6 | 10.8 | 6.07 | 18.2 | 5.23 | 13.5 | 4.62 | 14.8 | 4.68 |
| Average | 11.9 | 5.85 | 17.0 | 5.52 | 13.2 | 4.90 | 15.2 | 4.76 |

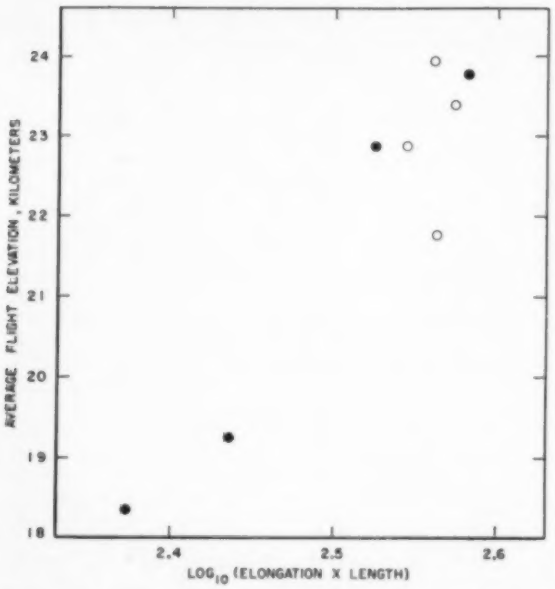


FIGURE 4. *Correlation between flight elevation and effective elongation.*

○, day flights and patch tests at −40° C; ●, night flights and patch tests at −60° C.

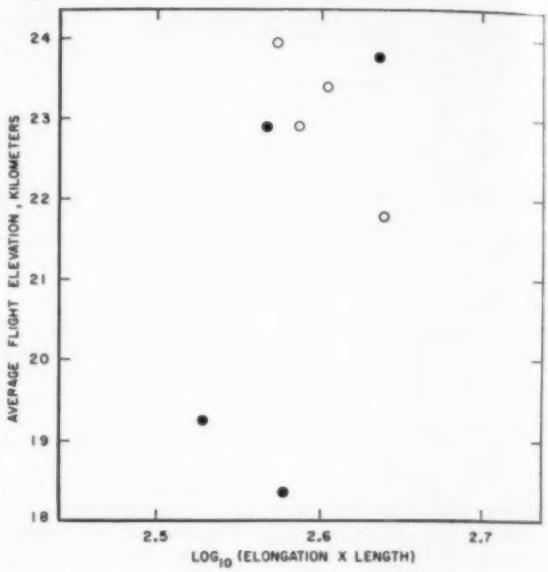


FIGURE 5. *Correlation between flight elevation and ultimate elongation.*

○, day flights and patch tests at −40° C; ●, night flights and patch tests at −60° C.

TABLE 6. *Estimation of temperature difference between day and night flights*

| Group | Ultimate elongation from patch test at— | | Effective elongation from patch test at— | | Flaccid length | | $T_D - T_N$ | |
|---|---|---|---|---|---|---|---|---|
| | −40° C | −60° C | −40° C | −60° C | Day flights | Night flights | From ultimate elongation | From effective elongation |
| | | | | | *in.* | *in.* | *° C* | *° C* |
| A | 5.94 | 5.85 | 4.99 | 5.16 | 73.3 | 74.0 | −38 | 17.6 |
| B | 5.67 | 5.52 | 5.15 | 5.44 | 68.1 | 68.6 | 232 | 12.8 |
| C | 5.38 | 4.90 | 5.01 | 4.45 | 74.8 | 75.3 | 9 | 6.8 |
| D | 5.25 | 4.76 | 5.11 | 3.85 | 71.3 | 70.9 | 46 | 14.4 |

## 7. Temperature of Balloon During Flight

Sounding balloons usually attain higher elevations during the day than at night. For the post-plasticized balloons that have been developed in the last few years, the difference between day and night flights is not large, but some regular balloons have been tested that flew satisfactorily in the daytime but flew very poorly at night. This variation between day and night flights appears to be due to a difference in the temperature of the balloon film. The temperature of the air in the stratosphere is about the same day or night. However, during the day the balloon film is heated by the sun's radiation and should be at a higher temperature than its surroundings. (Although the thin neoprene film is fairly transparent to visible light, it absorbs strongly in the ultraviolet and infrared regions of the spectrum.) At night the gas inside the balloon is cooled by expansion, and the temperature of the balloon film should be slightly below that of the air.

Groups of balloons have been flown both day and night, and patch tests have been made at two different temperatures. From the differences in day- and night-flight elevations, and the rates of change of the effective elongation with the temperature of the patch test, the balloon films have been estimated to be anywhere from 5° to 25° C warmer during the day than at night.

The method of estimating this temperature difference will be illustrated for the four groups of balloons in the planned flight experiment discussed in section 6. The necessary equations are

$$h_D - h_N = 49 \log_{10}\left(\frac{E_D L_D}{E_N L_N}\right), \tag{25}$$

$$\frac{T_D - T_N}{20} = \frac{E_D - E_N}{E_{-40} - E_{-60}}. \tag{26}$$

Equation (25) is derived from an expression similar to eq (24) but with different values of the constants. The subscript $D$ refers to conditions during day flights, and the subscript $N$ refers to conditions during night flights. Equation (26) is obtained by assuming that the elongation varies linearly with the temperature. The subscripts −40 and −60

refer to the temperatures at which the elongations were measured in the patch test.

The average flaccid lengths of the balloons flown during the day and flown at night and the differences in average day and night flight elevations may be substituted in eq (25). Then the elongation found from the patch test at −60° C is substituted for $E_N$, and eq (25) may be solved for the corresponding value of $E_D$. Using these values of $E_D$ and $E_N$ in eq (26), we may solve for the difference in temperature of the balloon film during day and during night flights. Table 6 gives the data used and the estimated temperature differences made in this manner for the four groups of balloons in the planned flight experiment, using both ultimate and effective elongations. Groups B and D show the most rapid change in effective elongation with the temperature, and should give the best estimates of the temperature difference. The values calculated from the effective elongations are more consistent than those calculated from the ultimate elongations. Furthermore, the balloons of group A burst at a lower average elevation in the daytime than they did at night; this result is predicted from the effective elongations, but not from the ultimate elongations at the two temperatures.

No inexpensive and reliable method of measuring the temperature of the balloon film itself during flight is known, but the Weather Bureau has made five flights in which the temperatures inside and outside of the balloon were measured. Radiosondes were modified to give three temperature readings. The air temperature was measured in the normal manner in a duct in the radiosonde box. Two additional temperature readings were obtained in place of the relative-humidity circuit. These readings were taken inside the balloon, which was carrying the radiosonde at positions near the top and near the bottom of the balloon. For night flights ordinary thermistors were used on all positions. For day flights white-coated thermistors (approximate diameter of 0.075 in.) were used inside the balloon to minimize the heating effect of solar radiation. The flights were made during December and January. No corrections were made to the thermistor readings for night flights. For day flights the air temperatures were corrected for errors due to solar radiation according to standard Weather Bureau practice. No corrections were made for the errors due to solar radiation on the thermistors inside the balloon, because the exact corrections are not known for this type of exposure (shielding from solar radiation by the rubber film and very little ventilation).

At night the temperature of the gas inside the balloon near the top averaged about the same as that of the outside air and the temperature inside the balloon near the bottom averaged about 4 deg C colder than the outside air. For day flights at an elevation of 16 km the indicated temperatures inside the balloon were 17 deg C warmer than the surrounding air near the top and 15 deg C warmer near the bottom. At an elevation of 22 km, the indicated temperatures inside the balloon were 23 deg C warmer near the top and 22 deg C warmer near the bottom than the outside air. Figure 6 gives a record of one of the day flights.

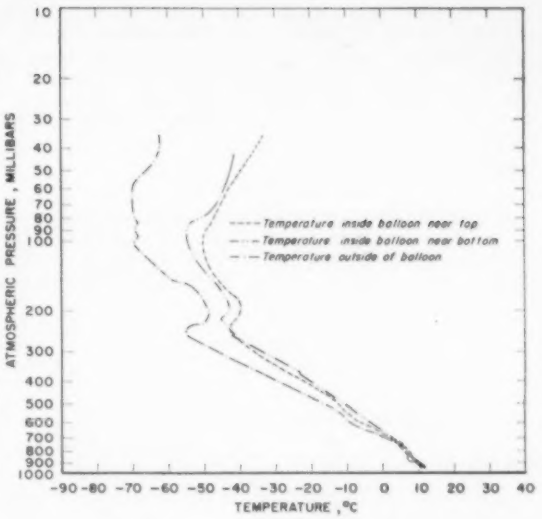


FIGURE 6. *Temperatures inside and outside of a post-plasticized balloon during a day flight.*

The temperatures indicated by the thermistors inside the balloon are estimated to be no more than 3 deg C warmer than the surrounding gas during the day flights. It seems probable that the daytime temperature of the rubber film itself is not very different from that indicated by the thermistors inside the balloon. Therefore, it may be assumed that the rubber film is warmer than the air during day flights and that the temperature difference increases with the elevation. At normal bursting elevations of 20 to 30 km, the film is probably 20 to 30 deg C warmer than the surrounding air during the day, whereas at night the rubber film may average 0 to 4 deg C colder than the surrounding air. Although the number of flights is too small to estimate the reliability of these results, there appear to be no inconsistencies between duplicate flights.

## 8. Summary

Because the Navy prefers to use a single type of balloon for both day and night flights and because the night flight is usually the more severe test, most of the patch tests were made at −60° C, following the procedure given in section 2. This temperature is approximately that of the rubber film at the time of burst in a night flight. The comparison of night-flight elevations with the results from the −60° C patch test indicates that the estimated effective elongation is a better measure of the quality of a balloon than the average ultimate elongation. A simple and economical ground test that can replace flight tests completely is not yet available. How-

ever, ground tests should be useful in controlling manufacturing processes, in determining whether experimental compounds might make satisfactory balloons, and in rejecting balloons of inferior quality. Planned flight experiments, combined with more extensive ground tests, may add to our knowledge of the factors that affect the performance of sounding balloons.

---

The flight tests for this work were made by the U. S. Weather Bureau through the cooperation of Herbert W. Rahmlow and F. P. Williams, of the Radiosonde Section, and of Jeff D. Ardoin, Silver Hill, Md., Weather Station. The temperature-measuring flights were planned with the aid of the Engineering, Upper Air Section of the Weather Bureau. The modification of the radiosondes and the flights were made by Christos Harmantas, Mary W. Hodge, Joseph S. Szokolszky, and Walter D. Smith of that section. At the National Bureau of Standards, Russell J. Capott, Richard S. Cleveland, Joseph J. Hamm, Ellis O. Knox, Elmer A. Koerner, John E. Pugh, Louis Schuman, Elmer W. Zimmerman, and others have contributed to the project.

WASHINGTON, April 23, 1954.

Journal of Research of the National Bureau of Standards Vol. 53, No. 6, December 1954 Research Paper 2558

# Plate-Separation Requirements for Standard Free-Air Ionization Chambers[1]

Frank H. Attix and LeRoy DeLaVergne

A method is described for measuring ionization losses resulting from inadequate separation of the parallel plates in free-air chambers. The ionization produced by X-rays scattered out of the collimated beam was measured separately and subtracted from the total to obtain the ionization contribution of only the electrons from the beam. Losses of this electron ionization are tabulated for plate separations from 6 to 36 centimeters, with moderately and heavily filtered X-rays from 50- to 250-kilovolt constant tube potential. Results are also converted into cylindrical coordinate form for application to chambers other than the parallel-plate type. A method is suggested for measurement, in other free-air chambers, of the contribution of ionization by scattered X-rays. Ionization-loss results are compared with previous experiments.

## 1. Introduction

For many years the free-air ionization chamber has been the standard instrument for the measurement in roentgens of X-radiation dose below 200 kilovolts. Agreement between the standard chambers of several national laboratories within about ±1 percent was established in 1931 by Taylor [1, 2],[2] and the design of the standard chamber [3, 4] at the National Bureau of Standards has remained unchanged from that time until recently.

In 1952, Kemp and Hall [5] made a precise study of the lateral dimension requirements for complete utilization of electron ionization in a parallel-plate, variable-pressure air chamber. The results indicated that the standard chambers at the National Bureau of Standards and at the National Physical Laboratory in England were inadequate in this respect, and that electric field distortion was responsible for the consistant underestimation of plate-separation requirements by other workers.

Preliminary measurements at the Bureau early in 1953, using a large free-air chamber with improved distortion characteristics, indicated that even larger chamber dimensions might be required than those predicted by Kemp and Hall. On the basis of this preliminary work, a temporary standard was constructed having plates 20 cm in separation and 26.8 cm in height. A comparison between this chamber and the old NBS standard chamber with X-rays of 200 kv (constant potential) and medium filtration (0.52-mm Cu plus 1.0-mm Al) revealed that the old chamber was measuring about 2 percent less ionization than the new one, in fair agreement with the predictions of Kemp and Hall.

A direct intercomparison between the National Physical Laboratory chamber and the new National Bureau of Standards chamber was carried out at NPL in June of 1953 [6]. The NPL chamber was found to be subject to ionization losses of about 3 percent at 195 kv (constant potential), which was close to the results Kemp and Hall obtained with a replica of the NPL chamber.

However, because of the disagreement between their work and the preliminary measurements made at the Bureau, and because their evidence placed in doubt the previously accepted free-air chamber design criteria, a broad study of the problem was undertaken. Both the field-distortion and plate-separation characteristics of free-air chambers are being investigated at the Bureau for X-rays generated by potentials up to 500 kv. This present paper deals primarily with the plate-separation requirements for X-rays generated by potentials up to 250 kv.

The definition of the roentgen requires the measurement of all the ionization produced by electrons that originate within a known volume of irradiated air. It is not practicable to measure this ionization however, because one cannot separate it from the ionization produced by other electrons originating in neighboring volumes of air, which must, of necessity, also be irradiated. The free-air chamber overcomes this difficulty by utilizing the "electronic-equilibrium" condition existing along the direction of the X-ray beam, as shown in figure 1. The cross-hatched region represents the known volume in the sense of the roentgen definition. Its dimensions are established by the area of the limiting diaphragm, D, and the length of ion-collecting plate C (assuming a uniform electric field). Ionization is collected throughout the region enclosed by the dashed lines. Some electrons, such as $e_1$, having paths predominantly perpendicular to the X-ray beam will expend their entire energies within the ion-collecting region, assuming the plate separation to be sufficiently large. (Actually, of course, the electron paths are not straight as indicated.) Others, like $e_2$, will pass out of that region and produce ionization where it will be collected on one of the guard plates and, hence will not be measured. Under the electronic-equilibrium condition, this ionization loss is just compensated by the contribution of other electrons, such as $e_3$, assuming air attenuation of the primary beam to be small. Such a condition can only exist if the two ends of the box are at a distance (from the ion-collecting region)

[1] This work was supported in part by the Atomic Energy Commission. This paper was presented at the December 16, 1953, meeting of the Radiological Society of North America, and appears in the December 1954 issue of Radiology.

[2] Figures in brackets indicate the literature references at the end of this paper.

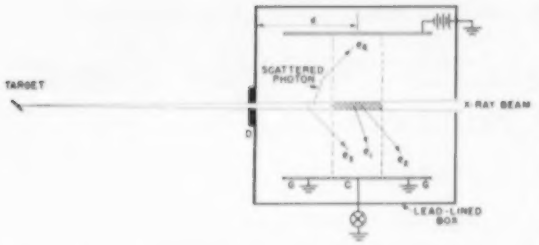


FIGURE 1. *Schematic plan view of a parallel-plate free-air ionization chamber.*

greater than the range of the electrons present, or about half the distance required for plate separation.

Electrons like $\epsilon_4$, resulting from scattered photons, produce ionization that is not included in the definition of the roentgen as these electrons do not originate within the cross-hatched volume of air nor do they compensate for ionization losses of other electrons that do. Their ionization contribution is usually assumed to be negligible. However, in large chambers that assumption may not be justified. On the other hand, the presence of such unwanted ionization would tend to compensate for loss of electron ionization (i. e., ionization produced by electrons that originate within the X-ray beam) due to insufficient plate separation. A method will be described for measurement of this ionization by scattered X-rays in free-air chambers.

Some mention should be made of the correction for air attenuation of X-rays in the distance $d$ (see fig. 1). Because limiting diaphragm D determines the total X-ray flux passing into the chamber, a free-air chamber measurement actually establishes the dose at the position of that diaphragm, except for the small attenuation of the beam in traversing the air between the diaphragm and the ion-collecting region.[3]

## 2. Apparatus and Experiment

### 2.1. General Method

The experiment consisted of three types of measurements for each kilovoltage and filtration:

1. Determination of the ionization produced in parallel layers of air, each 1 cm in thickness, at various perpendicular distances from a narrowly collimated X-ray beam, using a special experimental "grid" chamber.

2. A repeat of 1, except that a sheet of material (hereafter called the "electron filter") was interposed between the X-ray beam and the ion-collecting region to absorb all the electrons originating in the beam, but allow scattered X-rays to pass through with little attenuation, making it possible to differentiate between the two. By subtracting the ionization measured with the electron filter in place from that measured without the filter, the ionization was obtained for only the electrons originating in the beam, as required by the roentgen definition.

3. Measurement of the ionization produced in a conventional free-air chamber by the same X-ray beam used in the first two types of measurements. This was done to provide a figure for the ionization integrated over the entire ionized volume, so that the previous measurements of ionization in various parts of the volume could be expressed as fractions to the whole.

From these measurements it was possible of calculate the percentage by which the ionization produced by electrons from the X-ray beam in a free-air chamber would be decreased by inadequate separation of the parallel plates.

### 2.2. Grid Chamber

Figure 2 is a plan view of the experimental ionization chamber. It was housed within a lead-lined box, A, 70 cm long by 33 cm wide by 39 cm high. The electrode system was positioned along one side wall of the box, and consisted of a graphite plate, K, for collecting the ionization, surrounded by coplanar guard plates, J. In front of the collector were two parallel grids of graphite-coated nylon thread, L, which defined the volume in which ionization was collected (shaded area in fig. 2). The first row of threads was 1 cm from the collector plate, and was operated at $\pm 135$ v, which was found to be ample to avoid ion recombination in the collecting volume. The second row was at ground potential to give a more clearly defined collecting volume by reducing the "bulging" of field lines between the threads of the first row.

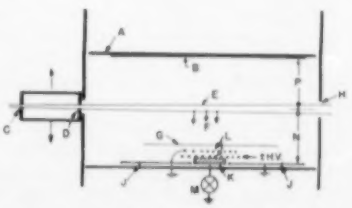


FIGURE 2. *Plan view of grid chamber.*

A, Lead box 70 cm long, 33 cm wide, 39 cm high; B, ¼a in. Lucite lining, graphite-coated; C, defining diaphragm, 1-cm diam, 76 cm from tube target; D, scatter diaphragm, 1.8-cm diam, 17 cm from defining diaphragm; E, collimated X-ray beam, approx 1.8-cm diam at position opposite collecting electrode; F, electrons and scattered photons; G, electron filter, 1.7-mm polystyrene, graphite-coated and connected to ground, positioned 2 cm from outer grid; H, X-ray beam exit hole, 7.4-cm diam; J, aluminum guard plates, 18 cm long and 33 cm high, graphite-coated; K, graphite collecting electrode, 10 cm by 24 cm by 5 mm; L, graphite-coated nylon threads; M, vibrating-reed electrometer; N, beam to plate distance, variable from 4 to 22 cm; P, distance of beam from opposite wall, variable from 24 to 6 cm; P+N is constant at 28 cm.

[3] The effective length $d$, of the absorbing air column is subject to some uncertainty because it depends on the average center of origin of the electrons contributing to the ionization in the collecting region. Taking this position at the center of the collecting region assumes that electron ranges are short, or that their paths are homogeneous in direction forward and rearward. At higher X-ray energies where forward-directed electrons predominate, the center of origin shifts toward the diaphragm and the effective air-absorption column decreases in length. If the scattered-photon ionization in a chamber is measured and corrected for in the dose calculation, then to be consistent the total absorption coefficient should be used in the air-absorption correction; that is, the coefficient should be experimentally determined by a method involving "narrow-beam" geometry, where the variable air column lies outside the narrowly diaphragmed chamber box, rather than by moving the plate system within the box.

The front and back walls of the lead box were fixed in position, as was the X-ray beam, E. The remainder of the box, including the electrode system, was mounted on a track at right angles to the X-ray beam, allowing the variation of the distance, $N$, from the X-ray beam to the collector plate over the range 4 to 22 cm. The distance $P+N$ to the wall opposite the electrode system was 28 cm. That wall and the top and bottom of the box were lined with $\frac{1}{16}$-in. graphite-coated Lucite, B, to minimize electron backscattering.

The electron filter, G, consisted of a sheet of graphite-coated polystyrene 1.7 mm in thickness, electrically connected to ground. When in place, this filter stopped all electrons approaching the collecting volume from outside the filter, but allowed scattered photons to pass through with negligible attenuation. When the filter was removed, both electrons and scattered photons were allowed to pass.

Most of the electrons stopped by the filter originated within the X-ray beam. Hence the difference between the two measurements (filter in, filter out) approximately represents ionization produced by electrons of the roentgen definition. However, the filter also intercepted some electrons produced outside the beam (and outside the filter position) by scattered photons. These electrons were partially replaced by those ejected from the inner surface of the filter itself. As will be seen from the data in figure 4, such compensation was not complete at 100 kv (or at lower kilovoltages) where photoelectric effect in the air made the filter material slightly non-air-equivalent. It was possible to correct for this, as will be discussed further in relation to figure 4.

Figure 3 is a detail drawing of the grid chamber electrode system, indicating its dimensions and the mounting of the threads. Actually, the grids were made of only one long nylon thread, which was wound around spiral grooves in the two aluminum rods, F. This thread was then painted with alcohol "dag" in such a way as to leave parts E bare, to serve as insulators, but to connect the inner row of threads to the upper rod and the outer row to the lower rod. External electrical connections were then made to the rods themselves.

The collector plate was made of graphite so that it would be nearly air-equivalent from the standpoint of electron backscattering. To determine the magnitude of this effect, the graphite was replaced with aluminum in one instance for 200-kv X-rays with medium filtration. The ionization measured with the electron filter in place was about 60 percent greater than for the graphite plate because of photoelectric effect in the aluminum. However, the calculated results for electron ionization losses in free-air chambers, based on the aluminum-plate data, did not differ appreciably from those calculated from the graphite-plate data except at small distances from the X-ray beam, as is shown in table 2. Hence since electron scattering varies roughly as $Z^2$, one may assume that the experimental results are not significantly influenced by backscatter of electrons from the graphite collector plate.

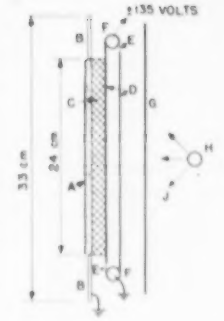


FIGURE 3. *Grid-chamber electrode system, viewed from rear.*

A, Graphite collecting electrode; B, graphite-coated aluminum guard plates; C, ion collecting volume, 1 cm by 10 cm by 24 cm; D, graphite - coated nylon threads in two rows 1 cm apart. Separation of threads in each row 5 mm, with 30 threads per row. Thread diameter, 0.2 mm; E, part of each thread not covered by graphite, to provide insulation; F, 0.5-in. diam graphite-coated aluminum rods supporting the nylon threads. Rods are cut with a spiral groove of five turns to the inch, to properly position the threads. Distance between axes of the two rods, 29.4 cm; G, electron filter, graphite-coated polystyrene; H, X-ray beam; J, electrons and scattered photons.

## 2.3. Standard Free-Air Chamber

Measurement of the ionization integrated over the entire ionized volume was made by means of the present NBS standard chamber mentioned in the introduction. Plate separation was 20 cm, plate height, 26.8 cm. The limiting diaphragm diameter (1 cm) and the collector plate length (10 cm) were the same as those in the grid chamber. The standard chamber was located on one side of the grid chamber, with the limiting diaphragms of the two chambers in the same plane. The X-ray tube housing was mounted on a track running at right angles to the beam direction, and could thus be positioned in alinement with either chamber. Standard-chamber readings were made in conjunction with each grid-chamber run, the X-ray tube output being constant.

One might ask why the standard-chamber reading was necessary, since it would seem possible to get the total ionization by merely summing up the grid-chamber measurements over the whole volume. This was prohibited by the fact that the grid-chamber plate system could not be moved closer to the X-ray beam than about 6 cm with the electron filter in place, or 4 cm without it. Closer positioning would have caused the beam penumbra to strike the grids or filter. Thus, it was not possible with the grid chamber to make measurements in the most densely ionized central region.

Small errors in the standard chamber itself, such as might be caused by slight insufficiency in plate separation, would have a negligible effect on the subsequent calculations of ionization losses.

A detailed description of this standard chamber will be the subject of a later paper.

## 2.4. Measurement of Ionization Current

A vibrating-reed electrometer was used as a null-detecting device for the current measurements. Currents larger than about $10^{-12}$ amp were passed through calibrated multimegohm resistors, and the resulting IR drops compensated by a potentiometer

connected in series. For smaller currents a compensating rate-of-charge method was employed, the charge being collected on a calibrated capacitor which was an integral part of the electrometer.

All measurements were carried out at atmospheric pressure and room temperature, approximately 755 mm Hg and 26° C, respectively.

The ionization currents measured in the grid chamber with different polarities of voltage on the inner grid were generally not identical in magnitude, since there was some ionization generated by scattered X-rays in the region behind the collecting electrode. There the grid potential had no influence, but contact-potentials served to collect ionization. This extra-cameral ionization was corrected for by measuring the current with both polarities and averaging the two values. The unwanted current is added in one case and subtracted in the other, and is thus cancelled out.

### 2.5. X-Ray Apparatus and Beam Filtration

A 250 kv X-ray tube enclosed in a thick lead housing was employed for this work. The high-voltage generator supplied an essentially constant potential, having a ripple not exceeding 0.6 percent. Kilovoltage and tube current were continuously monitored during operation and were, by manual adjustment, maintained at a constant value within $\pm 0.1$ percent.

The inherent filtration of the X-ray tube was equivalent to approximately 3 mm of Al. Additional filtration [4] was placed at the 1.27-cm-diam portal in the tube housing, located 16 cm from the target. In table 1 are given the added filtrations used at various kilovoltages, together with the copper half-value layers of the filtered beams.

TABLE 1. *X-ray beam characteristics*

| Constant potential | Added [a] filtration | Copper half-value-layers |
|---|---|---|
| | Medium | |
| *kv* | *mm* | *mm* |
| 90 | None | 0.077 |
| 75 | ...do | .099 |
| 100 | 1.02 Al | .176 |
| 150 | 0.228 Cu+1.02 Al | .60 |
| 200 | 0.52 Cu+1.02 Al | 1.23 |
| 250 | 1.02 Cu+1.02 Al | 2.14 |
| | Heavy | |
| 100 | 0.53 Pb | 0.77 |
| 150 | 1.53 Sn+4.00 Cu | 2.42 |
| 200 | 0.70 Pb+4.00 Sn+0.59 Cu | 4.03 |
| 250 | 2.70 Pb+1.00 Sn+0.59 Cu | 5.28 |

[a] Inherent filtration: 3 mm Al.

The "heavy" filtrations were essentially those of Ehrlich and Fitch [7]; note error in table 4, p. 16, filtration for 150 kv should be 1.53 mm Sn and 4 mm Cu.

## 3. Experimental Results

Figures 4 to 7 are given as examples of the ionization versus distance curves obtained with the grid chamber. Included are curves for 100 kv, medium filtration; 200 kv, heavy filtration; and 250 kv, with both medium and heavy filtration. The filters used were those listed in table 1. The electron curves have been determined by a point-by-point subtraction of the filter-in curve from the filter-out curve.

The extrapolated range of 100-kev electrons in air at atmospheric pressure is given in the literature [8] as 12 cm. Compton recoil electrons produced by 100-kv X-rays will have energies not exceeding 28 kev, and thus ranges less than 2 cm. This identifies the electrons producing the curve in figure 4 as photoelectrons. Therefore, the bend in the upper curve clearly shows the transition from electron ionization to that resulting from scattered X-rays. Beyond 15 cm the "filter-in" and "filter-out" curves are seen to be parallel and at a constant separation, even though the lower curve has been corrected for attenuation of scattered photons. They should coincide beyond the 12-cm range of the electrons from the X-ray beam. The observed discrepancy is probably caused by the lack of air equivalence of the electron filter material, as was mentioned previously. It is corrected for by raising the lower curve parallel to itself until it coincides with the upper one at large distances.

Figure 5 presenting ionization curves for 200-kv X-rays with heavy filtration also has a sharp bend in the "filter out" curve. However, in this case the "filter-in" curve lies well below it, and thus photon scattering cannot account for the abrupt change in slope. The cause becomes evident if one again considers the types of electrons present. For the X-ray wavelengths present in the primary beam, the absorption coefficient for air will consist of about 2-percent photoelectric effect and 98-percent Compton effect. The range of the maximum-energy photoelectrons will be about 37 cm, whereas the range of the most energetic Compton electrons (88 kev) will be 9 cm. Thus the change in the slope of the curves of figure 5 at 9 cm represents the transition from Compton electrons to the longer-range photoelectrons.

It should be mentioned in regard to figure 5 (and all other cases of heavy X-ray filtration) that the lower curve, for electron filter in place, had to be estimated in an indirect way. The background current in the grid chamber was of the order of $10^{-15}$ amp and was sometimes unsteady, making it very difficult to obtain reliable measurements of ionization currents of that order of magnitude or smaller. Hence, it was thought preferable to estimate the curve in the following way: The slope was taken in each case to be the same as for the corresponding medium X-ray filtration as these were found to be about the same for all energies. Then the curve was adjusted to a position such that twice the area under the curve out to 10 cm was in agreement with

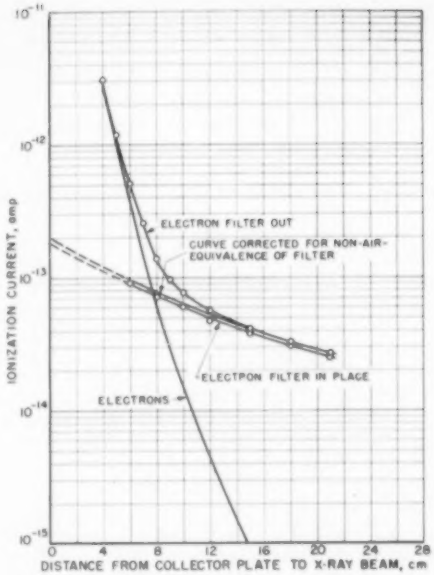
IONIZATION CURRENT, amp
ELECTRON FILTER OUT
CURVE CORRECTED FOR NON-AIR-EQUIVALENCE OF FILTER
ELECTPON FILTER IN PLACE
ELECTRONS
DISTANCE FROM COLLECTOR PLATE TO X-RAY BEAM, cm

FIGURE 4. *Grid-chamber current versus distance from X-ray beam.*

100 kv, medium filtration (1.02-mm Al). Standard free-air chamber current: $4.73\times10^{-13}$ amp.

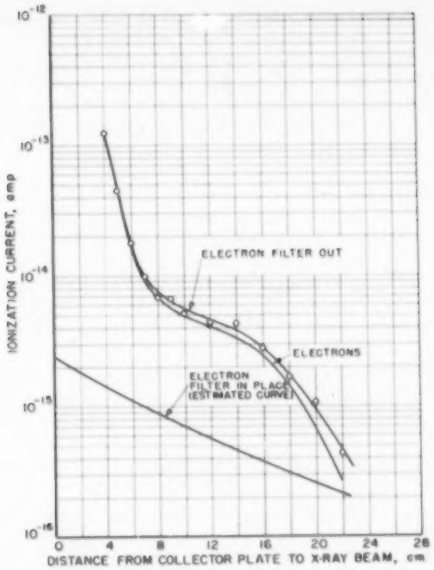
IONIZATION CURRENT, amp
ELECTRON FILTER OUT
ELECTRONS
ELECTRON FILTER IN PLACE (ESTIMATED CURVE)
DISTANCE FROM COLLECTOR PLATE TO X-RAY BEAM, cm

FIGURE 5. *Grid-chamber current versus distance from X-ray beam.*

200 kv, heavy filtration (0.70-mm Pb+4.00-mm Sn+0.59-mm Cu). Standard free-air chamber current: $1.076\times10^{-11}$ amp.

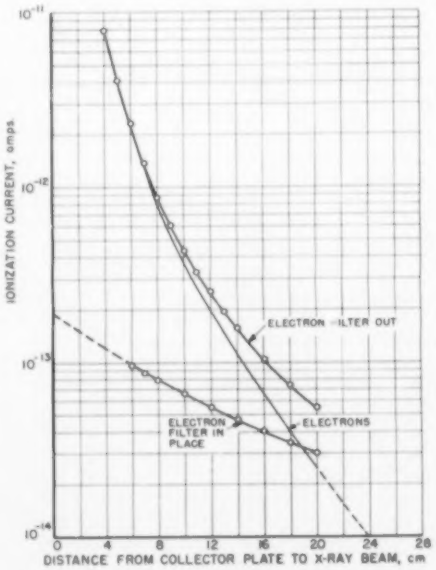


FIGURE 6. *Grid-chamber current versus distance from X-ray beam.*

250 kv, medium filtration (1.02-mm Cu+1.02-mm Al). Standard free-air chamber current: $7.82\times10^{-13}$ amp.

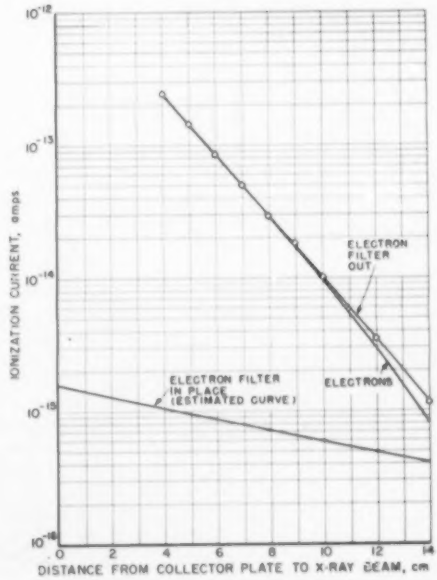
IONIZATION CURRENT, amps
ELECTRON FILTER OUT
ELECTRON FILTER IN PLACE (ESTIMATED CURVE)
ELECTRONS
DISTANCE FROM COLLECTOR PLATE TO X-RAY BEAM, cm

FIGURE 7. *Grid-chamber current versus distance from X-ray beam.*

250 kv, heavy filtration (2.7-mm Pb+1.00-mm Sn+0.59-mm Cu). Standard free-air chamber current: $8.89\times10^{-12}$ amp.

the total scattered photon contribution measured in the 20-cm standard free-air chamber, by a method to be described. This was assumed to be proper because a similar comparison between scatter measurements in the free-air chamber and the grid chamber showed generally good agreement for the medium X-ray filtrations.

In figure 7, representing the ionization curves obtained with heavy filtration at 250 kv, the bend observed in figure 5 has disappeared. The photoelectric effect in air is negligible here, and the ionization is almost entirely produced by Compton electrons. Their energies will not exceed 123 kev, and hence their ranges extend to only about 15 cm, which appears to be consistent with the curves in figure 7.

It is thus apparent that the plate-separation requirements for 200 kv with heavy filtration are greater than for 250 kv, because of the disappearance of the photoelectric effect in air at the latter energy.

## 4. Calculation of Electron Ionization Losses

For each kilovoltage and filtration the percentage electron-ionization losses caused by insufficient plate separation in free-air chambers were calculated by means of the formula

$$\frac{(100)(1.087)(2)\sum_{d}^{\infty}(I_{efo}-I_{efi})}{I_{sc}},$$

where

$I_{efo}$ = the grid-chamber ionization current with the electron filter out;

$I_{efi}$ = the grid-chamber ionization current with the electron filter in place;

$I_{sc}$ = the corresponding ionization current in the standard free-air chamber;

$d$ = the variable distance (cm) from collector plate to X-ray beam in the grid chamber, $d-1=s/2$, where $s$ is the free-air chamber plate separation for which the ionization loss is being computed. 1 is subtracted from $d$ to account for the 1-cm depth of the grid-chamber collecting volume.

The factor (2) is included because the grid chamber measures the ionization on only one side of the X-ray beam. The (1.087) is a correction factor that accounts for the area covered by the nylon threads, which stop the electrons that strike them.

The summation sign indicates that the electron current is summed up, for layers each 1 cm in thickness, from distance $d$ out to infinity. The electron ionization curves were simply assumed to continue with unchanging slope at plate-to-beam distances exceeding those at which data were obtained.

In figure 8 are plotted the resulting ionization losses for the curves in figures 4 to 7. Table 2 contains data for all kilovoltages studied.

It should be noted that in the calculations the diameter of the X-ray beam is not considered, and the distances are reckoned from the central axis of the beam. Thus the results are most accurate when applied to chambers having X-ray beams of about the same diameter (1.8 cm) as was used here.

Thus far, only the losses resulting from inadequate plate separation have been discussed, and no mention has been made of plate height, which is of course of equal importance. A chamber should be designed with both of those dimensions sufficiently large to allow nearly all the electrons projected radially outward from the X-ray beam to run their full ranges without leaving the ion-collecting volume, either by striking the plates at the sides or by escaping out the top and bottom. The data in table 2 represent

TABLE 2. *Percentage electron-ionization losses for various plate separations in a free-air chamber*

| Plate separation | Kilovoltage and filtration | | | | | | | | | | |
|---|---|---|---|---|---|---|---|---|---|---|---|
| | 60 kv Medium | 75 kv Medium | 100 kv | | 150 kv | | 200 kv | | | 250 kv | |
| | | | Medium | Heavy | Medium | Heavy | Medium | Medium * | Heavy | Medium | Heavy |
| *cm* | % | % | % | % | % | % | % | % | % | % | % |
| 6 | 0.2 | 0.80 | 2.2 | 6.4 | 4.3 | 3.9 | 4.9 | 5.5 | 4.8 | 5.0 | 14.5 |
| 8 | <.05 | .20 | 0.8 | 3.2 | 2.1 | 3.1 | 2.6 | 2.9 | 2.3 | 2.9 | 8.5 |
| 10 | | <.05 | .3 | 1.5 | 1.2 | 2.5 | 1.6 | 1.8 | 1.4 | 1.8 | 4.9 |
| 12 | | | .1 | 0.6 | 0.6 | 1.9 | 1.0 | 1.2 | 1.1 | 1.1 | 2.8 |
| 14 | | | .0 | .2 | .4 | 1.5 | 0.7 | 0.8 | 0.8 | 0.7 | 1.7 |
| 16 | | | <.05 | .1 | .2 | 1.1 | .5 | .5 | .7 | .5 | 0.9 |
| 18 | | | | .0 | .1 | 0.8 | .3 | .4 | .5 | .4 | .5 |
| 20 | | | | <.05 | .1 | .5 | .2 | .3 | .5 | .3 | .2 |
| 22 | | | | | .0 | .4 | .1 | .2 | .4 | .2 | .1 |
| 24 | | | | | .0 | .2 | .1 | .1 | .3 | .1 | .0 |
| 26 | | | | | <.05 | .1 | .1 | .1 | .3 | .1 | <.05 |
| 28 | | | | | | .1 | .0 | .1 | .2 | .1 | |
| 30 | | | | | | .0 | .0 | .0 | .1 | .0 | |
| 32 | | | | | | <.05 | <.05 | .0 | .1 | .0 | |
| 34 | | | | | | | | .0 | .0 | .0 | |
| 36 | | | | | | | | <.05 | .0 | <.05 | |

* The data in this column were obtained with a bare aluminum collecting plate in place of the graphite plate normally used in the grid chamber. They illustrate the magnitude of the effect of electron backscattering on the results.

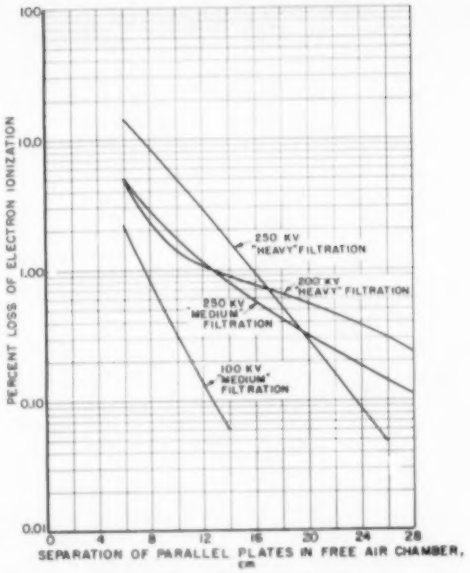


FIGURE 8. *Electron ionization losses in parallel-plate free-air chambers with adequate plate height.*

losses caused by plate-separation inadequacy alone, assuming the plate height to be adequate. What constitutes adequate plate height is complicated by field distortion, as pointed out by Kemp and Hall [5]. The collecting volume may be defined as the region occupied by the electric-field lines that terminate on the collector plate. This region will be considerably smaller in effective height than the plates themselves, if the field is not properly guarded from the effects of the grounded chamber enclosure. The actual cross-sectional shape of the collecting volume of a particular chamber, in a plane at right angles to the X-ray beam, is obtainable from a study of field lines in an electrolytic tank.

It was thought to be desirable to convert the data in table 2 into a more general form that could be applied to any free-air chamber in which the cross-sectional shape of the collecting volume were known. A graphical method was found for doing this.

The graph used in this calculation was similar to that shown in figure 9, but drawn to a large scale. The ionization field was assumed to be made up of concentric cylindrical shells, each 1 cm in thickness and containing a uniform ionization density. The superimposed rectangles, 24 cm in height and 1 cm in thickness, represent various positions of the grid-chamber collecting volume. By first taking planimeter measurements, the unknown ionization densities in the cylindrical shells were deduced from the known electron ionizations in the grid-chamber volume. It was then possible to calculate how much of the ionization lay outside of any given radius, i. e., the ionization that would be lost by a cylindrical chamber of that radius, positioned coaxially with the beam. Table 3 gives the results of such calculations.

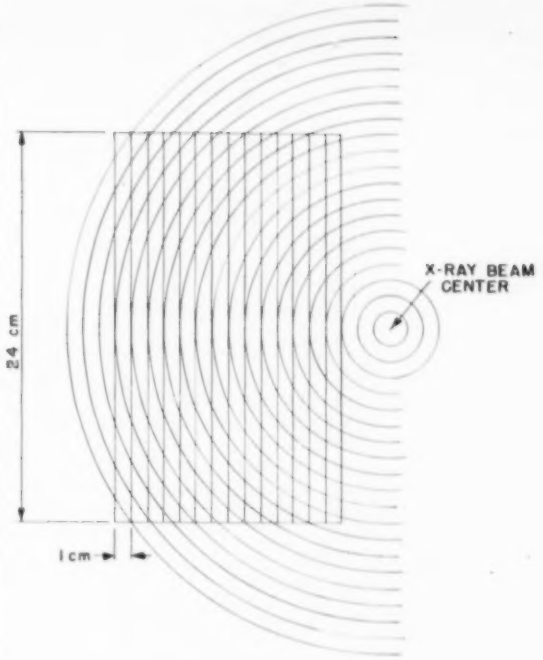


FIGURE 9. *Drawing similar to that used for planimeter measurements to determine the ionization densities existing in cylindrical shells coaxial with the X-ray beam.*

To apply these results to any chamber for which the cross-sectional shape of the collecting volume is known, it is necessary to plot the cross section on polar-coordinate graph paper, with the X-ray beam located at the origin. The ionization losses are then obtained from table 3 for a number of representative radii on the plot, weighted according to the angular sector they represent, and summed to give the total ionization loss.

A calculation of this sort was carried out to determine the adequacy of the 24-cm height of the collector plate in the grid chamber, and the effect on the data in table 2. In the worst cases (250 kv, medium filtration; 200 kv, heavy filtration) the tabulated percentage losses in table 2 were found to be too small by about 0.2 percent for figures of 1 percent or larger, and by 0.1 percent or less for figures below 1 percent. The data in table 3 are not subject to this error as the actual collector-plate height of the grid chamber was taken into account in the calculation of that data.

The ionization contributed by scattered X-rays in a particular free-air chamber will depend not only upon the plate separation and height, but also upon the length of the irradiated air column within the chamber enclosure; thus, this ionization cannot be conveniently tabulated. It was therefore considered preferable to describe a method by which the ioniza-

TABLE 3. *Percentage losses of electron ionization outside of various radii from the X-ray beam*

| Radius | Kilovoltage and filtration | | | | | | | | | |
|---|---|---|---|---|---|---|---|---|---|---|
| | 60 kv Medium | 75 kv Medium | 100 kv | | 150 kv | | 200 kv | | 250 kv | |
| | | | Medium | Heavy | Medium | Heavy | Medium | Heavy | Medium | Heavy |
| *cm* | % | % | % | % | % | % | % | % | % | % |
| 3 | 0.7 | 2.1 | 4.9 | 12.9 | 8.9 | 6.0 | 9.7 | 10.4 | 9.9 | 27.7 |
| 4 | .1 | .5 | 2.0 | 7.6 | 4.7 | 5.3 | 5.5 | 5.0 | 6.1 | 18.1 |
| 5 | <.05 | .1 | .8 | 4.1 | 2.7 | 4.6 | 3.5 | 2.9 | 4.0 | 11.5 |
| 6 | | <.05 | .3 | 2.0 | 1.6 | 3.9 | 2.3 | 2.2 | 2.7 | 7.2 |
| 7 | | | .1 | .8 | 1.1 | 3.3 | 1.7 | 1.8 | 1.9 | 4.4 |
| 8 | | | .0 | .3 | .7 | 2.6 | 1.3 | 1.6 | 1.4 | 2.7 |
| 9 | | | <.05 | .2 | .5 | 2.1 | .9 | 1.4 | 1.1 | 1.6 |
| 10 | | | | .1 | .3 | 1.6 | .7 | 1.3 | .8 | .9 |
| 11 | | | | .0 | .2 | 1.2 | .5 | 1.1 | .6 | .5 |
| 12 | | | | .0 | .1 | .8 | .4 | 1.0 | .5 | .3 |
| 13 | | | | <.05 | .1 | .6 | .3 | .8 | .4 | .1 |
| 14 | | | | | .0 | .4 | .2 | .7 | .3 | .0 |
| 15 | | | | | .0 | .2 | .1 | .5 | .3 | <.05 |
| 16 | | | | | <.05 | .1 | .1 | .4 | .2 | |
| 17 | | | | | | .1 | .1 | .3 | .2 | |
| 18 | | | | | | .0 | .0 | .2 | .1 | |
| 19 | | | | | | <.05 | .0 | .1 | .1 | |
| 20 | | | | | | | <.05 | .1 | .1 | |
| 21 | | | | | | | | .0 | .1 | |
| 22 | | | | | | | | <.05 | .0 | |

tion by scattered X-rays can be directly determined with sufficient accuracy in any given chamber.

A tube of nearly air-equivalent material such as Lucite, extending the full length of the chamber enclosure, is positioned inside the chamber, so that the X-ray beam passes through it from end to end. The tube must have walls thick enough to stop the electrons, but thin with respect to attenuation of scattered X-rays. The plastic should be made conducting with a graphite coating, and operated at half the potential of the high voltage plate, to minimize field distortion. The X-ray beam is narrowly collimated to prohibit the penumbra from producing excess scatter by striking the walls of the tube, which should be as small in diameter as practicable. The ratio of ionization measured with the tube in place to that with it removed will give the fraction of the total ionization that is contributed by scattered X-rays. As most of the electrons have short ranges (see table 3), the normal distribution of electrons generated by scattered X-rays in the chamber will not be significantly disturbed by the presence of the tube. A small error will be produced by the "shadowing" effect of the tube because it collects the ionization produced between it and the high-voltage plate, prohibiting that ionization from arriving at the collector plate. This can be corrected with sufficient accuracy by simply taking into account the collecting volume lost by the effect. Details of the application of this method to the NBS standard chamber will be included in a later paper; however, the ionization from scattered X-rays in that chamber was found to constitute 0.3 to 0.4 percent of the total ionization, increasing slowly with decreasing energy.

The net ionization loss of a free-air chamber is found by subtracting the measured contribution due to scattered X-rays from the appropriate figures for loss of electron ionization as given in tables 2 and 3.

## 5. Comparison of Grid-Chamber Results With Other Measurements

Two chambers were constructed whose predicted ionization losses (from grid-chamber results) were large because of inadequate dimensions. Care was taken to avoid field distortion in these chambers. The actual deficiency was then determined experimentally for 200-kv X-rays with medium filtration by comparison with the 20-cm standard chamber. In the latter chamber electron losses and scattered photon contributions compensate one another within about 0.05 percent at that energy.

Table 4 gives the results for a chamber of 24-cm height and separations from 6 to 9 cm. Table 5 gives similar data for a chamber 10 cm in height and the same range of separations. Agreement with grid-chamber predictions is good in both cases.

In the light of these results and other considerations, the limits of error of the electron-loss data in tables 2 and 3 are estimated to be $\pm 0.3$ percent, except for the grid-chamber plate-height inadequacy, which affects only table 2. The loss figures are

TABLE 4. *Comparison of predicted and measured deficiencies for parallel plate chambers*

24 cm plate height

| Free-air chamber plate separation | Measured ionization deficiency | Ionization [a] deficiency from grid-chamber data |
|---|---|---|
| *cm* | % | % |
| 6 | 4.9 | 5.0 |
| 7 | 3.5 | 3.6 |
| 8 | 2.7 | 2.7 |
| 9 | 2.1 | 2.1 |

[a] These figures have been raised by 0.1 percent to account for the estimated difference in scattered photon ionization in the 20-cm standard chamber and the test chamber.

TABLE 5. *Comparison of predicted and measured deficiencies for parallel-plate chambers*

10-cm plate height

| Free-air chamber plate separation | Measured ionization deficiency | Ionization * deficiency from grid-chamber data |
|---|---|---|
| *cm* | % | % |
| 6 | 6.0 | 5.8 |
| 7 | 4.7 | 4.7 |
| 8 | 3.9 | 3.9 |
| 9 | 3.3 | 3.3 |

* These figures have been raised by 0.15 percent for the reason noted in table 4.

probably within closer limits of error at larger plate separations, where the losses themselves are decreased.

## 5.1. Comparison With Results of Kemp and Hall

The results of the measurements of Kemp and Hall [5] are expressed as ionization losses in chambers having *square* cross sections of various sizes. These ionization loss figures are compared with corresponding figures from the present work in table 6, for 100-kv X-rays.

TABLE 6. *Comparison with work of Kemp and Hall*

| Square-chamber dimensions | Ionization losses of Kemp and Hall, 100 kvp | Electron - ionization losses from grid-chamber measurements, 100-kv constant potential |
|---|---|---|
| *cm* | % | % |
| 9.6×9.6 | <0.1 | 0.7 |
| 7.4×7.4 | .5 | 1.9 |
| 6.5×6.5 | 1.0 | 3.0 |

It is evident that large differences exist between the two sets of data, the ionization losses of Kemp and Hall being smaller than reported here. Similar discrepancies were found to exist at the other kilovoltages as well. The most important factors contributing to these differences are:

1. Difference in quality of the X-rays used. The copper half-value-layer obtained by Kemp and Hall at 100 kvp was 0.078 mm,[5] as compared with a value of 0.176 mm obtained in the present experiment. Kemp and Hall used a Villard circuit and 2-mm Al inherent filtration, compared with a constant potential generator and 3-mm Al inherent filtration.

2. Difference in X-ray beam diameter. Kemp and Hall employed a beam about 1 cm in diameter, as compared with the present 1.8 cm.

## 5.2. Comparisons With Work of Others

To facilitate comparisons with other experiments at kilovoltages differing from those used for the present experiment, a graph of plate separation versus kilovoltage is given in figure 10 for medium X-ray filtration. Also plotted on this graph are the points at which complete [6] collection of ionization was observed by other investigators. Constant-potential kilovoltages were used in every case. Filtrations were not given except by Duane and Lorenz, who used 2-mm Al at 95 kv, but did not state the filtrations for other kilovoltages, and by Failla, who used 0.1-mm Cu and 2.15-mm Al at 110 kv. One may assume a medium or light filtration was employed in all the other instances.

The results of Taylor, Singer, and Charlton [9] are essentially in agreement with the present grid-chamber data, since it is unlikely that they could have detected by their method the very small increments of ionization existing at greater separations. Their ionization chamber was relatively free from electric-field distortion at separations up to 18 cm, because of the long guard plates (25 cm), the large collecting-plate height (35 cm), and a system of guard wires, all enclosed in a tank of ample dimensions (65-cm diam by 213-cm length). The other data of Taylor [10] were given as part of a general survey paper, and were not all obtained with an individual chamber. The point at 240 kv was taken from reference [9]. The other data were taken in two other chambers, each of which is now known, in the light of recent developments, to have been subject to considerable field distortion, accounting for the low values obtained for the separations.

The same explanation also applies to the results of Kaye and Binks [11], Duane and Lorenz [12], and Failla [13].

Failla's work was particularly interesting, inasmuch as he made a careful study of the field distor-

[5] Figure supplied by Kemp in a private communication.

[6] The other investigators used the method of varying the plate separation while observing the ionization current. Complete ionization collection was assumed to exist at the point where no detectable increase in ionization was observed with further increase in separation. Their methods did not differentiate between electron ionization and that produced by scattered X-rays, but simply measured the total of the two.

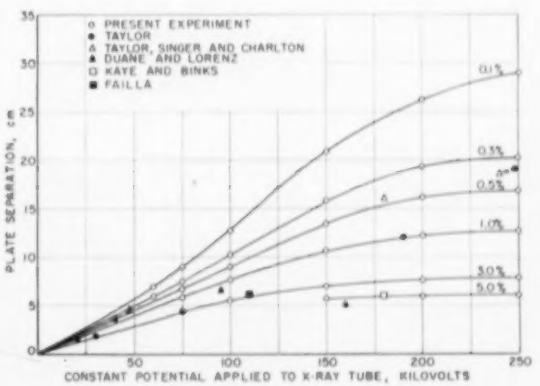


FIGURE 10. *Comparison with results of other workers for medium X-ray filtrations and constant potentials.*

The curves are drawn through points obtained in the present experiment, each curve indicating the plate separations at which equal losses of electron ionization occur for various kilovoltages. The other points represent separations at which other workers observed complete collection of ionization (see footnote 6).

tion existing within his chamber. His collecting-plate was divided into 11 adjacent vertical strips, each 3.8 cm wide, so that he could measure the ionization in various volumes along the X-ray beam. He found that the ionization currents collected by several of the centrally located strips were the same, and that the closer the plate separation, the larger the number of adjacent strips collecting the same current. This was interpreted as an indication of the region over which no field distortion was present. One could equally well interpret the same facts as showing the region over which the distortion produced the *same error* in each strip. The latter would seem to be the case, since, in another measurement, Failla varied the plate separation from 6 to 20 cm and measured a constant current output from the central strip out to 15-cm separation. The present work shows that the current should have increased by about 3 percent over this range of separations, for 110-kv X-rays with medium filtration. Hence, the effective collecting volume of the central strip probably decreased by about 3 percent because of worsening field distortion. This has been substantiated by preliminary measurements of field distortion by Miller and Kennedy at the Bureau.

The field-distortion problem is thus seen to be much more serious than has been heretofore supposed, and new criteria must be established for designing distortion-free chambers. This problem is now under investigation.

The authors express their appreciation to H. O. Wyckoff for many helpful discussions relating to this work.

## 6. References

[1] L. S. Taylor, BS J. Research **8,** 9 (1932) RP397; Radiology **18,** 99 (1932).
[2] L. S. Taylor, BS J. Research **8,** 325 (1932) RP417; Radiology **18,** 627 (1932).
[3] L. S. Taylor and G. Singer, BS J. Research **5,** 507 (1930) RP211; Radiology **15,** 637 (1930).
[4] L. S. Taylor and G. Singer, J. Research NBS **16,** 165 (1936) RP865; Radiology **26,** 322 (1936).
[5] L. A. W. Kemp and S. M. Hall, Brit. J. Radiol. **27,** 219 (1954).
[6] H. O. Wyckoff, G. H. Aston, and E. E. Smith, Brit. J. Radiol. **27,** 325 (1954).
[7] M. Ehrlich and S. H. Fitch, Nucleonics **9,** 5 (1951).
[8] N. N. Das Gupta and S. H. Ghosh, Revs. Mod. Phys. **18,** 280 (1946).
[9] L. S. Taylor, G. Singer, and A. L. Charlton, J. Research NBS **21,** 19 (1938) RP1111.
[10] L. S. Taylor, Brit. J. Radiol. **24,** 67 (1951).
[11] G. W. C. Kaye and W. Binks, Brit. J. Radiol. **6,** 530 (1933).
[12] W. Duane and E. Lorenz, Am. J. Roentgenol. **19,** 461 (1928).
[13] G. Failla, Am. J. Roentgenol. **21,** 47 (1929).

Washington, July 8, 1954.

# INDEX TO VOLUME 53

## July to December 1954—Research Papers 2510 to 2558


### A

Page

Absolute standards of mutual inductance, a study of, RP2548 ..... 297
Adiabatic demagnetization installation at NBS, RP2530 ..... 173
Aerological sounding balloons, RP2557 ..... 383
*Allen, H. C., Jr., E. E. Naylor, E. K. Plyler,* Deuterium-sulfide band at 4,590 $cm^{-1}$, RP2549 ..... 321
Alloys, high-temperature, determination of nickel, manganese, cobalt, and iron in, RP2552 ..... 353
Anhydrous sodium hydroxide: heat content, transition temperature, and melting point, RP2519 ..... 81
*Armstrong, G. T.,* Vapor pressure of nitrogen, RP2543 ..... 263
*Attir, F. H., L. DeLaVergne,* Plate-separation requirements for standard free-air ionization chambers, RP2558 ..... 393
Austenite-ferrite, delta, reactions and the formation of carbide, sigma, and chi phases in chromium-nickel-molybdenum steels, RP2517 ..... 67

### B

Bacher and Goudsmit theory of complex spectra, RP2515 ..... 35
*Bagg, T. C., F. Stair, R. G. Johnston,* Spectral distribution of energy from the sun, RP2523 ..... 113
*Ball, A. F., T. B. Douglas, G. T. Furukawa, R. E. McCoskey,* Calorimetric properties of normal heptane from 0° to 520° K, RP2526 ..... 139
Balloons, aerological sounding, RP2557 ..... 383
*Bates, R. G., V. E. Bower,* Standard potential of the silver–silver-chloride electrode from 0° to 95° C and the thermodynamic properties of dilute hydrochloric acid solutions, RP2546 ..... 283
*Beckstoldt, C. J., H. C. Vacher,* Delta ferrite-austenite reactions and the formation of carbide, sigma, and chi phases in 18 chromium-8 nickel-3.5 molybdenum steels, RP2517 ..... 67
*Benedict, W. S., E. K. Plyler,* Infrared emission spectra of cyanide and dicarbon radicals, RP2528 ..... 161
Bounds on a distribution function that are functions of moments to order four, RP2556 ..... 377
*Bower, V. E., R. G. Bates,* Standard potential of the silver–silver-chloride electrode from 0° to 95° C and the thermodynamic properties of dilute hydrochloric acid solutions, RP2546 ..... 283
*Brabant, J. M., R. S. Caswell, A. Schwebel,* Disintegration rate of carbon-14, RP2513 ..... 27
*Bright, H. A., J. L. Hague, E. D. Brown,* Separation of titanium, tungsten, molybdenum, and niobium by anion exchange, RP2542 ..... 261
—, —, *E. E. Maczkowske,* Determination of nickel, manganese, cobalt, and iron in high-temperature alloys, using anion-exchange separations, RP2552 ..... 353
Bromide, separation of, from chloride and iodide, RP2511 ..... 13
*Brown, D. W., R. E. Florin, L. A. Wall, L. A. Hyma, J. D. Michaelsen,* Factors affecting the thermal stability of polytetrafluoroethylene, RP2524 ..... 121
*Brown, E. D., J. L. Hague, H. A. Bright,* Separation of titanium, tungsten, molybdenum, and niobium by anion exchange, RP2542 ..... 261
*Buckley, F., A. A. Maryott,* Influence of molecular shape on the dielectric constant of polar liquids, RP2539 ..... 229
*Buzzard, R. W., J. J. Park,* The gold-uranium system, RP2547 ..... 291

### C

Calorimetric properties of normal heptane, RP2526 ..... 139
Canada balsam, refractivity measurements on, by interferometry, RP2555 ..... 373
Carbon-14, determination of, by counting in formamide and other solvents, RP2537 ..... 221
Carbon-14, disintegration rate, RP2513 ..... 27
Carbon-14, position-labeled sugars with:
RP2536 ..... 217
RP2550 ..... 325
Carbohydrates, position-labeled with carbon-14:
RP2536 ..... 217
RP2550 ..... 325
*Carlson, E. T.,* Some properties of strontium hydroxide and its monohydrate, RP2554 ..... 371
*Caswell, R. S., J. M. Brabant, A. Schwebel,* Disintegration rate of carbon-14, RP2513 ..... 27
Chloride, separation of, from bromide and iodide, RP2511 ..... 13
Chromium-nickel-molybdenum steels, delta ferrite-austenite reactions and the formation of carbide, sigma, and chi phases in, RP2517 ..... 67
*Clabaugh, W. S., T. J. Murphy, R. Gilchrist,* Separation of iodide, bromide, and chloride from one another and their subsequent determination, RP2511 ..... 13
Cobalt, nickel, manganese, and iron in high-temperature alloys, determination of, RP2552 ..... 353
Combustible liquids, self-ignition temperatures, RP2516 ..... 49
Compression of linear high polymers at high pressures, temperature dependence of, RP2540 ..... 245
*Connar, W. S., T. I. Davenport, W. B. Mann, C. C. McCraven, C. C. Smith, W. J. Youden,* Comparison of four national radium standards, RP2544 ..... 267
—, *W. J. Youden,* New experimental designs for paired observations, RP2532 ..... 191
Correlation of polarized light phenomena with the orientation of some metal crystals, RP2510 ..... 1
Creep of high-purity nickel, RP2551 ..... 329
Cyanide and dicarbon radicals, infrared emission spectra, RP2528 ..... 161
Cyanohydrin reaction, use of, in the synthesis of radioactive sugars:
RP2536 ..... 217
RP2550 ..... 325

### D

Page

*Davenport, T. I., W. B. Mann, C. C. McCraven, C. C. Smith, W. S. Connar, W. J. Youden,* Comparison of four national radium standards, RP2544 ..... 267
*de Hemptinne, M., V. H. Dibeler, F. L. Mohler,* Mass spectra of the deuteroethylenes, RP2522 ..... 107
*de Klerk, D., R. P. Hudson,* Installation for adiabatic demagnetization experiments at the National Bureau of Standards, RP2530 ..... 173
*DeLaVergne, L., F. H. Attir,* Plate-separation requirements for standard free-air ionization chambers, RP2558 ..... 393
Demagnetization experiments, adiabatic, at NBS, RP2530 ..... 173
Density, optical rotation, and refractive indices of dextran solutions, RP2525 ..... 131
Deuterium-sulfide band at 4,590 $cm^{-1}$, RP2549 ..... 321
Deuteroethylenes, mass spectra, RP2522 ..... 107
*Dever, J. L., T. B. Douglas,* Anhydrous sodium hydroxide: the heat content from 0° to 700° C, the transition temperature, and the melting point, RP2519 ..... 81
Dewpoint method, determination of relative humidity-temperature relationships of saturated salt solutions by, RP2512 ..... 19
Dextran, optical rotation, density, refractive index, RP2525 ..... 131
*Dibeler, V. H., F. L. Mohler, M. de Hemptinne,* Mass spectra of the deuteroethylenes, RP2522 ..... 107
Dielectric constant of polar liquids, influence of molecular shape on, RP2539 ..... 229
*Digges, T. G., W. B. Jenkins, C. R. Johnson,* Creep of high-purity nickel, RP2551 ..... 329
Disintegration rate of carbon-14, RP2513 ..... 27
Distribution function, bounds on, RP2556 ..... 377
*Douglas, T. B., J. L. Dever,* Anhydrous sodium hydroxide: the heat content from 0° to 700° C, the transition temperature, and the melting point, RP2519 ..... 81
—, *G. T. Furukawa, R. E. McCoskey, A. F. Ball,* Calorimetric properties of normal heptane from 0° to 520° K, RP2526 ..... 139
—, *W. M. Logan,* Heat content of molybdenum disilicide from 0° to 900° C, RP2520 ..... 91
*Dressler, R. F.,* Turbulent flow in shock tubes of varying cross section, RP2541 ..... 253
*Dryden, M. P., C. F. Snyder, H. S. Isbell, N. B. Holt,* Optical rotations, refractive indices, and densities of dextran solutions, RP2525 ..... 131

### E

Electrode, silver–silver-chloride, standard potential of, RP2546 ..... 283
Ethylene-*d*, mass spectra, RP2522 ..... 107
Experimental designs for paired observations, RP2532 ..... 191

### F

Ferrite-austenite reactions, delta, and formation of carbide, sigma, and chi phases in chromium-nickel-molybdenum steels, RP2517 ..... 67
*Fillmore, C. L., S. M. Lang, R. S. Roth,* Some properties of porcelains and phase relations in the ternary systems of beryllia and zirconia with titania, ceria, and chromia, RP2534 ..... 201
*Florin, R. E., L. A. Wall, D. W. Brown, L. A. Hyma, J. D. Michaelsen,* Factors affecting the thermal stability of polytetrafluoroethylene, RP2524 ..... 121
Formamide, assay of radioactive materials dissolved in, RP2537 ..... 221
*Frush, H. L., H. S. Isbell, N. B. Holt,* Synthesis of D-galactose-1-$C^{14}$ and D-talose-1-$C^{14}$, RP2536 ..... 217
—, —, —, Synthesis of $\alpha$-D-xylose-1-$C^{14}$ and $\beta$-D-lyxose-1-$C^{14}$, RP2550 ..... 325
*Furukawa, G. T., T. B. Douglas, R. E. McCoskey, A. F. Ball,* Calorimetric properties of normal heptane from 0° to 520° K, RP2526 ..... 139
Fused-quartz glass, index of refraction, RP2531 ..... 185

### G

D-Galactose-1-$C^{14}$, synthesis, RP2536 ..... 217
Gas analysis, determination of hydrogen by volumetric combustion and chemical absorption, RP2518 ..... 77
*Gilchrist, R., R. B. Johannesen, C. L. Gordon, J. E. Stewart,* Application of infrared spectroscopy to the determination of impurities in titanium tetrachloride, RP2533 ..... 197
—, *T. J. Murphy, W. S. Clabaugh,* Separation of iodide, bromide, and chloride from one another and their subsequent determination, RP2511 ..... 13
Glass, fused-quartz, index of refraction, RP2531 ..... 185
Glass, refractivity, RP2529 ..... 165
Gold-uranium system, RP2547 ..... 291
*Gordon, C. L., R. B. Johannesen, J. E. Stewart, R. Gilchrist,* Application of infrared spectroscopy to the determination of impurities in titanium tetrachloride, RP2533 ..... 197
*Graver, F. W.,* A study of absolute standards of mutual inductance and in particular the three-section National Bureau of Standards type, RP2548 ..... 297

### H

*Hague, J. L., E. D. Brown, H. A. Bright,* Separation of titanium, tungsten, molybdenum, and niobium by anion exchange, RP2542 ..... 261
—, *E. E. Maczkowske, H. A. Bright,* Determination of nickel, manganese, cobalt, and iron in high-temperature alloys, using anion-exchange separations, RP2552 ..... 353
*Hasegawa, S., A. Wexler,* Relative humidity-temperature relationships of some saturated salt solutions in the temperature range 0° to 50° C, RP2512 ..... 19

Page

Heat capacity and heat of fusion of *n*-heptane, RP2526 ... 139
Heat content of molybdenum disilicide, RP2520 ... 91
Heptane, normal, calorimetric properties, RP2526 ... 139
*Holt, N. B., H. S. Isbell, H. L. Frush,* Synthesis of D-galactose-1-$C^{14}$ and D-talose-1-$C^{14}$, RP2536 ... 217
—, —, —, Synthesis of α-D-xylose-1-$C^{14}$ and β-D-lyxose-1-$C^{14}$, RP2550 ... 325
—, *C. F. Snyder, H. S. Isbell, M. R. Dryden,* Optical rotations, refractive indices, and densities of dextran solutions, RP2525 ... 131
*Hudson, R. P., D. de Klerk,* Installation for adiabatic demagnetization experiments at the National Bureau of Standards, RP2540 ... 173
Humidity, effect on calibration of National Bureau of Standards thermal-radiation standards, RP2535 ... 211
Humidity-temperature relationships of some saturated salt solutions in the temperature range 0° to 50° C, RP2512 ... 19
Hydrochloric-acid solutions, thermodynamic properties of, RP2546 ... 283
Hydrogen, determination by slow combustion over platinum in excess oxygen, RP2518 ... 77
Hydroxide, anhydrous sodium, thermodynamic properties, RP2519 ... 81
Hydroxide, strontium, properties, RP2554 ... 371
*Hyma, L. A., R. E. Florin, L. A. Wall, D. W. Brown, J. D. Michaelsen,* Factors affecting the thermal stability of polytetrafluoroethylene, RP2524 ... 121

## I

Ignition, self-, of combustible liquids, RP2516 ... 49
Index of refraction of fused-quartz glass, RP2531 ... 185
Infrared emission spectra of cyanide and dicarbon radicals, RP2528 ... 161
Infrared spectroscopy, application of, to the determination of impurities in titanium tetrachloride, RP2533 ... 197
Interferometer for measuring homogeneity of glass, RP2529 ... 165
Iodide, separation of, from bromide and chloride, RP2511 ... 13
Ionization chambers, standard free-air, plate-separation requirements for, RP2558 ... 393
Iron, nickel, manganese, and cobalt in high-temperature alloys, determination of, RP2552 ... 353
*Isbell, H. S., H. L. Frush, N. B. Holt,* Synthesis of D-galactose-1-$C^{14}$ and D-talose-1-$C^{14}$, RP2536 ... 217
—, —, —, Synthesis of α-D-xylose-1-$C^{14}$ and β-D-lyxose-1-$C^{14}$, RP2550 ... 325
—, *A. Schwebel, J. D. Mayer,* Determination of carbon-14 in solutions of $C^{14}$-labeled materials by means of a proportional counter, RP2537 ... 221
—, *C. F. Snyder, M. R. Dryden, N. B. Holt,* Optical rotations, refractive indices, and densities of dextran solutions, RP2525 ... 131
Isotopic ethylenes, mass spectra, RP2522 ... 107

## J

*Jenkins, W. D., T. G. Digges, C. R. Johnson,* Creep of high-purity nickel, RP2551 ... 329
*Johannesen, R. B., C. L. Gordon, J. E. Stewart, P. Gilchrist,* Application of infrared spectroscopy to the determination of impurities in titanium tetrachloride, RP2533 ... 197
*Johnson, C. R., W. D. Jenkins, T. G. Digges,* Creep of high-purity nickel, RP2551 ... 329
*Johnston, H. G., R. Stair,* Effects of recent knowledge of atomic constants and of humidity on the calibrations of the National Bureau of Standards thermal-radiation standards, RP2535 ... 211
—, —, *T. C. Bugg,* Spectral distribution of energy from the sun, RP2523 ... 113

## K

*Kessler, K. G., W. F. Meggers, C. E. Moore,* Extension of the arc spectra of palladium and platinum (6500 to 12000 A), RP2538 ... 225

## L

*Lang, S. M., R. S. Roth, C. L. Fillmore,* Some properties of porcelains and phase relations in the ternary systems of beryllia and zirconia with titania, ceria, and chromia, RP2534 ... 201
Light phenomena, polarized, correlation with orientation of some metal crystals, RP2510 ... 1
Liquids, combustible, self-ignition temperatures, RP2516 ... 49
*Logan, W. M., T. B. Douglas,* Heat content of molybdenum disilicide from 0° to 900° C, RP2520 ... 91
β-D-Lyxose-1-$C^{14}$, synthesis of, RP2550 ... 325

## M

Macrocalorimetric comparison of four national radium standards:
RP2544 ... 267
RP2545 ... 277
*Mackowski, E. E., J. L. Hague, H. A. Bright,* Determination of nickel, manganese, cobalt, and iron in high-temperature alloys, using anion-exchange separations, RP2552 ... 353
*Madorsky, S. L., S. Straus,* Thermal degradation of polymers as function of a molecular structure, RP2553 ... 361
*Mandel, J., G. M. Martin, R. D. Stiehler,* Aerological sounding balloons, RP2557 ... 383
—, *R. D. Stiehler,* Sensitivity—a criterion for the comparison of methods of test, RP2527 ... 155
Manganese, nickel, cobalt, and iron in high-temperature alloys, determination of, RP2552 ... 353
*Mann, W. B.,* A radiation balance for the macrocalorimetric comparison of four national radium standards, RP2545 ... 277
—, *T. I. Davenport, C. C. McCraven, C. C. Smith, W. S. Connor, W. J. Youden,* Comparison of four national radium standards, RP2544 ... 267
*Marpolt, A. A., F. Huckley,* Influence of molecular shape on the dielectric constant of polar liquids, RP2539 ... 229
Mass spectra of the deuteroethylenes, RP2522 ... 107
*McCoskey, R. E., T. B. Douglas, G. T. Furukawa, A. F. Ball,* Calorimetric properties of normal heptane from 0° to 520° K, RP2526 ... 139
*McCraven, C. C., T. I. Davenport, W. B. Mann, C. C. Smith, W. S. Connor, W. J. Youden,* Comparison of four national radium standards, RP2544 ... 267

Page

*Martin, G. M., J. Mandel, R. D. Stiehler,* Aerological sounding balloons, RP2557 ... 383
*Meggers, W. F., K. G. Kessler, C. E. Moore,* Extension of the arc spectra of palladium and platinum (6500 to 12000 A), RP2538 ... 225
Metal crystals oriented by polarized light, RP2510 ... 1
Meters, watthour, testing, RP2521 ... 95
*Michaelsen, J. D., R. E. Florin, L. A. Wall, D. W. Brown, L. A. Hyma,* Factors affecting the thermal stability of polytetrafluoroethylene, RP2524 ... 121
*Mohler, F. L., V. H. Dibeler, M. de Hemptinne,* Mass spectra of the deuteroethylenes, RP2522 ... 107
Molecular shape, influence on dielectric constant of polar liquids, RP2539 ... 229
Molecular spectrum of deuterium sulfide, RP2549 ... 321
Molecular structure, thermal degradation of polymers as function of, RP2553 ... 361
Molybdenum disilicide, thermodynamic properties, RP2520 ... 91
Molybdenum, titanium, tungsten, and niobium, separation of, by anion exchange, RP2542 ... 261
*Moore, C. E., K. G. Kessler, W. F. Meggers,* Extension of the arc spectra of palladium and platinum (6500 to 12000 A), RP2538 ... 225
*Mayer, J. D., A. Schwebel, H. S. Isbell,* Determination of carbon-14 in solutions of $C^{14}$-labeled materials by means of a proportional counter, RP2537 ... 221
*Murphy, T. J., W. S. Clabaugh, P. Gilchrist,* Separation of iodide, bromide, and chloride from one another and their subsequent determination, RP2511 ... 13
Mutual inductance, a study of absolute standards of, RP2548 ... 297

## N

*Naylor, B. F., H. C., Allen, Jr., E. K. Plyler,* Deuterium-sulfide band at 4,590 $cm^{-1}$, RP2549 ... 321
*Newton, C. J., H. C. Vacher,* Correlation of polarized light phenomena with the orientation of some metal crystals, RP2510 ... 1
Nickel, high-purity, creep of, RP2551 ... 329
Nickel, manganese, cobalt, and iron in high-temperature alloys, determination of, RP2552 ... 353
Niobium, titanium, tungsten, and molybdenum, separation of, by anion exchange, RP2542 ... 261
Nitrogen, vapor pressure, RP2543 ... 283

## O

Observations, paired, experimental designs for, RP2532 ... 191
Optical cement, refractive index of, RP2555 ... 373
Optical rotations, refractive indices, and densities of dextran solutions, RP2525 ... 131
Optical surfaces, testing of, RP2514 ... 29
Orientation of metal crystals by polarized light, RP2510 ... 1
Oxide porcelains, physical and phase equilibrium properties, RP2534 ... 201

## P

Palladium and platinum, extension of arc spectrum, RP2538 ... 225
*Park, J. J., R. W. Buzzard,* The gold-uranium system, RP2547 ... 291
Phase diagram of gold-uranium system, RP2547 ... 291
Plate-separation requirements for standard free-air ionization chambers, RP2558 ... 393
Platinum and palladium, extension of arc spectrum, RP2538 ... 225
*Plyler, E. K., H. C. Allen, Jr., B. F. Naylor,* Deuterium-sulfide band at 4,590 $cm^{-1}$, RP2549 ... 321
—, *W. S. Benedict,* Infrared emission spectra of cyanide and dicarbon radicals, RP2528 ... 161
Polar liquids, influence of molecular shape on the dielectric constant of, RP2539 ... 229
Polarized light phenomena, correlation with orientation of metal crystals, RP2510 ... 1
Polymers, linear high, temperature dependence of compression of, RP2540 ... 245
Polymers, thermal degradation of, as a function of molecular structure, RP2553 ... 361
Polytetrafluoroethylene, thermal stability, RP2524 ... 121
Porcelains, oxide, properties, RP2534 ... 201
Proportional counter, use of, for assay of radioactive materials in solution, RP2537 ... 221
Pyrolysis of polymers as a function of molecular structure, RP2553 ... 361

## R

Radiation balance for the macrocalorimetric comparison of four national radium standards, RP2545 ... 277
Radiation, solar, ultraviolet spectral-energy distribution, RP2523 ... 113
Radiation standards, NBS, effect of humidity on, RP2535 ... 211
Radioactive sugars, synthesis:
RP2536 ... 217
RP2550 ... 325
Radioactivity, measurement of, in formamide and other solvents, RP2537 ... 221
Radium standards, national, comparison:
RP2544 ... 267
RP2545 ... 277
Refractive index, density, and optical rotation of dextran solutions, RP2525 ... 131
Refractivity measurements on Canada balsam by interferometry, RP2555 ... 373
Refractivity measurements on thick plates, RP2529 ... 165
*Rodney, W. S., R. J. Spindler,* Index of refraction of fused-quartz glass for ultraviolet, visible, and infrared wavelengths, RP2531 ... 185
*Roth, R. S., S. M. Lang, C. L. Fillmore,* Some properties of porcelains and phase relations in the ternary systems of beryllia and zirconia with titania, ceria, and chromia, RP2534 ... 201

## S

Salt solutions, saturated, relative humidity-temperature relationships of, RP2512 ... 19
*Saunders, J. B.,* Refractivity measurements on Canada balsam by interferometry, RP2555 ... 373
—, Refractivity measurements on thick plates, RP2529 ... 165
—, Testing of large optical surfaces with small test plates, RP2514 ... 29

Page

*Schuhmann, S., M. Shepherd*, Determination of hydrogen by slow combustion over platinum in excess oxygen, RP2518 ... 77
*Schwebel, A., R. S. Caswell, J. M. Ibrabant*, Disintegration rate of carbon-14, RP2513 ... 27
—, *H. S. Isbell, J. D. Moyer*, Determination of carbon-14 in solutions of $C^{14}$-labeled materials by means of a proportional counter, RP2537 ... 221
Self-ignition temperatures of combustible liquids, RP2516 ... 49
Sensitivity—a criterion for the comparison of methods of test, RP2527 ... 155
Separation of titanium, tungsten, molybdenum, and niobium by anion exchange, RP2542 ... 261
*Setchkin, N. P.*, Self-ignition temperatures of combustible liquids, RP2516 ... 49
*Shepherd, M., S. Schuhmann*, Determination of hydrogen by slow combustion over platinum in excess oxygen, RP2518 ... 77
Shock tubes of varying cross section, turbulent flow in, RP2541 ... 253
Silver–silver-chloride electrode, standard potential of, RP2546 ... 283
*Smith, C. C., T. I. Davenport, W. B. Mann, C. C. McCraven, W. S. Connor, W. J. Youden*, Comparison of four national radium standards, RP2544 ... 267
*Snyder, C. F., H. S. Isbell, M. R. Dryden, N. B. Holt*, Optical rotations, refractive indices, and densities of dextran solutions, RP2525 ... 131
Sodium hydroxide, anhydrous, thermodynamic properties, RP2519 ... 81
Solar radiation, ultraviolet spectral-energy distribution, RP2523 ... 113
Spectra, complex, Bacher and Goudsmit, theory of, RP2515 ... 35
Spectra, infrared emission, of cyanide and dicarbon radicals, RP2528 ... 161
Spectra, mass, of the deuteroethylenes, RP2522 ... 107
Spectra, palladium and platinum, RP2538 ... 225
Spectral absorption of deuterium sulfide, RP2549 ... 321
Spectral distribution of energy from the sun, RP2523 ... 113
Spectroscopy, infrared, application in determination of impurities in titanium tetrachloride, RP 2533 ... 197
*Spindler, R. J., W. S. Rodney*, Index of refraction of fused-quartz glass for ultraviolet, visible, and infrared wavelengths, RP2531 ... 185
*Spinks, A. W., T. I. Zapf*, Precise comparison method of testing alternating-current watthour meters, RP2521 ... 95
*Stair, R., R. G. Johnston, T. C. Bagg*, Spectral distribution of energy from the sun, RP2523 ... 113
—, —, Effects of recent knowledge of atomic constants and of humidity on the calibrations of the National Bureau of Standards thermal-radiation standards, RP2535 ... 211
Standard potential of the silver–silver-chloride electrode from 0° to 95° C and the thermodynamic properties of dilute hydrochloric acid solutions, RP2546 ... 283
Standards, national radium, comparison:
RP2544 ... 267
RP2545 ... 277
Standards, NBS thermal-radiation, effect of humidity on, RP2535 ... 211
Standards of mutual inductance, absolute, study of, RP2548 ... 297
Statistical procedures and survey of comparison of four national radium standards, RP2544 ... 267
Statistics, mathematical, RP2556 ... 377
Steels, chromium, nickel, molybdenum, delta ferrite-austenite reactions and the formation of carbide, sigma, and chi phases in, RP2517 ... 67
*Stewart, J. E., R. B. Johannesen, C. L. Gordon, B. Gilchrist*, Application of infrared spectroscopy to the determination of impurities in titanium tetrachloride, RP2533 ... 197
*Stichler, E. D., J. Mandel*, Sensitivity—a criterion for the comparison of methods of test, RP2527 ... 155
—, *G. M. Martin, J. Mandel*, Aerological sounding balloons, RP2557 ... 383
*Straus, S., S. L. Madorsky*, Thermal degradation of polymers as a function of molecular structure, RP2553 ... 361
Strontium hydroxide monohydrate, preparation and properties of, RP2554 ... 371
Synthesis of D-galactose-1-$C^{14}$ and D-talose-1-$C^{14}$, RP2536 ... 217
Synthesis of α-D-xylose-1-$C^{14}$ and β-D-lyxose-1-$C^{14}$, RP2550 ... 325

## T

D-Talose-1-$C^{14}$, synthesis, RP2536 ... 217
Temperature dependence of compression of linear high polymers at high pressures, RP2540 ... 245

Page

Temperature-relative-humidity relationships of some saturated salt solutions, RP2512 ... 19
Temperatures, self-ignition, of combustible liquids, RP2516 ... 49
Test methods, sensitivity—a criterion for the comparison of, RP2527 ... 155
Tetrachloride, titanium, determination of impurities in, RP2533 ... 197
Thermal degradation of polymers as a function of molecular structure, RP2553 ... 361
Thermal-radiation standards, effects of recent knowledge of atomic constants and of humidity on the calibrations of, RP2535 ... 211
Thermal stability of polytetrafluoroethylene, RP2524 ... 121
Thermodynamic properties of anhydrous sodium hydroxide, RP2519 ... 81
Thermodynamic properties of hydrochloric-acid solutions, RP2546 ... 283
Thermodynamic properties of molybdenum disilicide, RP2520 ... 91
Titanium tetrachloride, determination of impurities in, RP2533 ... 197
Titanium, tungsten, molybdenum, and niobium, separation of, by anion exchange, RP2542 ... 261
*Trees, R. E.*, Bacher and Goudsmit theory of complex spectra, RP2515 ... 35
Tungsten, titanium, molybdenum, and niobium, separation of, by anion exchange, RP2542 ... 261
Turbulent flow in shock tubes of varying cross section, RP2541 ... 253

## U

Ultraviolet spectral-energy distribution of direct solar radiation, RP2523 ... 113
Uranium-gold system, phase diagram, RP2547 ... 291

## V

*Vacher, H. C., C. J. Bechtoldt*, Delta ferrite-austenite reactions and the formation of carbide, sigma, and chi phases in 18 chromium-8 nickel-3.5 molybdenum steels, RP2517 ... 67
—, *C. J. Newton*, Correlation of polarized light phenomena with the orientation of some metal crystals, RP2510 ... 1
Vapor pressure of nitrogen, RP2543 ... 263

## W

*Wall, L. A., R. E. Florin, D. W. Brown, L. A. Hyma, J. D. Michaelsen*, Factors affecting the thermal stability of ploytetrafluoroethylene, RP2524 ... 121
Watthour meters, testing, RP2521 ... 95
*Weir, C. E.*, Temperature dependence of compression of linear high polymers at high pressures, RP2540 ... 245
*Wexler, A., S. Hasegawa*, Relative humidity-temperature relationships of some saturated salt solutions in the temperature range 0° to 50° C, RP2512 ... 19

## X

α-D-Xylose-1-$C^{14}$, synthesis of, RP2550 ... 325

## Y

*Youden, W. J., W. S. Connor*, New experimental designs for paired observations, RP2532 ... 191
—, *T. I. Davenport, W. B. Mann, C. C. McCraven, C. C. Smith, W. S. Connor*, Comparison of four national radium standards, RP2544 ... 267

## Z

*Zapf, T. I., A. W. Spinks*, Precise comparison method of testing alternating-current watthour meters, RP2521 ... 95
*Zelen, M.*, Bounds on a distribution function that are functions of moments to order four, RP2556 ... 377

UNITED STATES
GOVERNMENT PRINTING OFFICE
DIVISION OF PUBLIC DOCUMENTS
WASHINGTON 25, D. C.
OFFICIAL BUSINESS

PENALTY FOR PRIVATE USE TO AVOID PAYMENT OF POSTAGE, $300 (GPO)

Journal of Research of the National Bureau of Standards Vol. 53, No. 6 December 1954

# Contents

| | | Page |
|---|---|---|
| Creep of high-purity nickel. William D. Jenkins, Thomas G. Digges, Carl R. Johnson. | RP2551 | 329 |
| Determination of nickel, manganese, cobalt, and iron in high-temperature alloys, using anion-exchange separations. John L. Hague, Edwin E. Maczkowske, and Harry A. Bright. | RP2552 | 353 |
| Thermal degradation of polymers as a function of molecular structure. S. L. Madorsky and S. Straus. | RP2553 | 361 |
| Some properties of strontium hydroxide and its monohydrate. Elmer T. Carlson. | RP2554 | 371 |
| Refractivity measurements on Canada balsam by interferometry. James B. Saunders. | RP2555 | 373 |
| Bounds on a distribution function that are functions of moments to order four. Marvin Zelen. | RP2556 | 377 |
| Aerological sounding balloons. Gordon M. Martin, John Mandel, and Robert D. Stiehler. | RP2557 | 383 |
| Plate-separation requirements for standard free-air ionization chambers. Frank H. Attix and LeRoy DeLaVergne. | RP2558 | 393 |
| Index to volume 53 (July to December 1954, Research Papers RP2510 to RP2558). | | 403 |

Single copies of the above Research Papers are not available for sale, but the Superintendent of Documents, U. S. Government Printing Office, Washington 25, D. C., will reprint 100 or more copies, and request for the purchase price should be mailed promptly to that Office.

For sale by the Superintendent of Documents, U. S. Government Printing Office, Washington 25, D. C. Price 60 cents (single copy). Subscription Price: $4 a year; $1.25 additional for foreign mailing. Single copies vary in price.

UNITED STATES GOVERNMENT PRINTING OFFICE, WASHINGTON : 1954